LASER CLADDING OF FeCrMoCB METALLIC GLASS ON NICKEL-FREE STAINLESS-STEEL TO DEVELOP DURABLE AND COST-EFFECTIVE BIOMEDICAL IMPLANTS

MAHMOUD ZAKARIA ALSAYED ABDALFATTAH IBRAHIM

FACULTY OF ENGINEERING
UNIVERSITY OF MALAYA
KUALA LUMPUR

2019

LASER CLADDING OF FeCrMoCB METALLIC GLASS ON NICKEL-FREE STAINLESS-STEEL TO DEVELOP DURABLE AND COST-EFFECTIVE BIOMEDICAL IMPLANTS

MAHMOUD ZAKARIA ALSAYED ABDALFATTAH IBRAHIM

THESIS SUBMITTED IN FULFILMENT OF THE REQUIREMENTS FOR THE DEGREE OF DOCTOR OF PHILOSOPHY

FACULTY OF ENGINEERING

UNIVERSITY OF MALAYA

KUALA LUMPUR

2019

UNIVERSITI MALAYA

ORIGINAL LITERARY WORK DECLARATION

Name of Candidate: **Mahmoud Zakaria Alsayed Abdalfattah Ibrahim** (A)

Registration/Matric No: **KHA150112**

Name of Degree: **Doctor of Philosophy (Ph.D)**

Title of Project Paper/Research Report/Dissertation/Thesis ("this Work"):

LASER CLADDING OF FeCrMoCB METALLIC GLASS ON NICKEL-FREE STAINLESS-STEEL TO DEVELOP DURABLE AND COST-EFFECTIVE BIOMEDICAL IMPLANTS

Field of Study: **Mechanical Engineering**

I do solemnly and sincerely declare that:
(1) I am the sole author/writer of this Work;
(2) This Work is original;
(3) Any use of any work in which copyright exists was done by way of fair dealing and for permitted purposes and any excerpt or extract from, or reference to or reproduction of any copyright work has been disclosed expressly and sufficiently and the title of the Work and its authorship have been acknowledged in this Work;
(4) I do not have any actual knowledge nor do I ought reasonably to know that the making of this work constitutes an infringement of any copyright work;
(5) I hereby assign all and every rights in the copyright to this Work to the University of Malaya ("UM"), who henceforth shall be owner of the copyright in this Work and that any reproduction or use in any form or by any means whatsoever is prohibited without the written consent of UM having been first had and obtained;
(6) I am fully aware that if in the course of making this Work I have infringed any copyright whether intentionally or otherwise, I may be subject to legal action or any other action as may be determined by UM.

Candidate's Signature Date

Subscribed and solemnly declared before,

Witness's Signature Date

Name:

Designation:

LASER CLADDING OF FeCrMoCB METALLIC GLASS ON NICKEL-FREE STAINLESS-STEEL TO DEVELOP DURABLE AND COST-EFFECTIVE BIOMEDICAL IMPLANTS

Abstract

Medical implants are man-made devices used to treat, heal or recover living tissues problems or deficiencies. The market surveys predicted that the global market value of medical implants will hit 116 billion USD by 2022. The orthopedic or bone implants segment is leading with 31% share of the total medical market and the joint replacement represent most of this segment. These figures reveal the high potential of the orthopedic implants industry, especially, the joint replacement implants. Thus, numerous of researchers focused on developing biomaterials for joint replacement applications. To ensure durability and long-term implant, the applied biomaterial should prove high wear and corrosion resistance, suitable mechanical properties and acceptable biocompatibility. Currently, three major metallic alloys are used; Titanium alloy (Ti6Al4V), Cobalt alloy (CoCrMo), and 316L stainless-steel. However, Ti6Al4V alloy lacks the tribology properties, while the CoCrMo alloy and 316L stainless-steel fail to prove high biocompatibility in the long-term. Although the progressive advancement in biomaterials, there is no record for successful permanent or long-term implant. 316L stainless-steel is still used because it is cheaper than other alloys (about tenth the cost of Ti and Co-alloys) and approved by the US Food and Drug Administration (FDA) for temporary implants. Nickel ion release is considered one of the hazardous effect rising from the 316L stainless-steel. In a way to improve the biocompatibility of 316L stainless-steel, a nickel-free stainless-steel is proposed known as ASTM F2229 or Cronidur30. This proposed alloy not only improved the 316L stainless-steel biocompatibility excluding the

Nickel ion hazardous effects but also proved better mechanical properties, enhanced wear and corrosion resistance. However, the alloy still needs further investigations to enhance its tribological, mechanical and biomedical characteristics to ensure the long-term durability for orthopedic implants. For this purpose, a cost-effective and durable Fe-based (FeCrMoCB) metallic glass is proposed to be laser cladded on ASTM F2229. Metallic glasses are featured with superior wear and corrosion resistance, mechanical properties and excellent biocompatibility. Fe-based metallic glass is abundant, available and has high glass forming ability. Laser cladding is a promising coating technique due to its ability to deposit vast materials on metals, establish a real metallurgical bond, thus high strength adhesion between the coating layer and the substrate, rapid heating and cooling rate required for amorphous structure formation, and offer clean and controllable technique. The cladded samples were prepared by preplacing FeCrMoCB amorphous powder on 30x30x3 mm ASTM F2229 samples, then cladded using high power diode laser. To optimize the coating layer; laser power, scanning speed, substrate surface roughness, overlap percentage, and laser beam spot size were varied. The macro and microstructure were examined using Optical microscope and scanning electron microscope, respectively. While, the phase transformation was recognized and analyzed using X-ray diffraction. The hardness, wear behavior (dry and in simulated body fluid), and corrosion resistance, were evaluated by microhardness and nano-indentation, ball-on disk wear test, electrochemical polarization, respectively. The cytocompatibility and bioactivity were investigated using direct cell-culture test and soaking in simulated body fluid, respectively. The investigations showed that the studied variables affected significantly the amorphous structure of the cladded FeCrMoCB layer which in turn affected the mechanical, tribology and corrosion properties. The results showed that

an amorphous-crystalline composite structure (76% amorphous content) showed better tribological properties than high amorphous structure (87% amorphous content). The cladded FeCrMoCB metallic glass layer proved higher hardness up to five times the substrate hardness, lower wear rate – both dry and wet – up to tenth that of the substrate, significantly enhanced corrosion resistance, beside good cytocompatibility. In addition, FeCrMoCB metallic glass showed excellent bioactivity which promotes it as intermediate bioactive material for excellent osseointegration in orthopaedic implants. It is concluded that the proposed FeCrMoCB metallic glass coating has high potential for bone implants, especially for joint replacement with higher durability and bioactivity and thus less revision surgeries is needed.

Keywords;

Laser cladding, Metallic glass materials, Nickel-free stainless-steel, orthopedic implants

PELAPISAN KACA LOGAM FeCrMoCB PADA NIKEL KELULI TAHAN KARAT NIKEL UNTUK MEMBANGUNKAN IMPLAN BIOMEDIKAL YANG TAHAN LAMA DAN KOS EFEKTIF

Abstrak

Implan perubatan merupakan peranti buatan manusia yang digunakan untuk merawat, menyembuh, dan memulih tisu hidup yang telah rosak atau cedera. Berdasarkan tinjauan pasaran, dijangkakan nilai pasaran global implan perubatan akan mencecah 116 billion USD menjelang tahun 2022. Bahagian implan ortopedik (tulang) mendahului pasaran perubatan dengan saham pasaran sebanyak 31% dan penggantian sendi mewakili sebahagian besar daripada bahagian tersebut. Ini menunjukkan bahawa industri implan ortopedik, khususnya, implan penggantian sendi, berpotensi tinggi untuk dibangunkan. Oleh itu, ramai penyelidik memberi tumpuan kepada pembangunan biobahan untuk tujuan penggantian sendi. Bagi memastikan daya ketahanan implan dalam jangka panjang, biobahan perlu memiliki ketahanan yang tinggi terhadap kakisan dan kehausan serta sifat mekanikal yang bersesuaian dan biokeserasian yang baik. Terdapat tiga jenis pancalogam yang biasa digunakan, iaitu: Titanium aloi (Ti6Al4V), Cobalt aloi (CoCrMo), dan keluli tahan karat 316L. Namun begitu, aloi Ti6Al4V tidak mempunyai sifat tribologi yang baik, manakala aloi CoCrMo dan keluli tahan karat 316L tidak mempunyai biokeserasian yang baik untuk penggunaan jangka panjang. Walaupun terdapat perkemanga progresif dalam bidang biobahan, sehingga kini belum ada biobahan yang berjaya dihasilkan untuk penggunaan implan kekal atau jangka masa panjang. Keluli tahan karat 316L masih digunakan secara meluas kerana kosnya hanya sepersepuluh kos aloi titanium dan kobalt.Ia juga diluluskan untuk kegunaan implan sementara oleh Pentadbiran Makanan dan Ubat-Ubatan Amerika Syarikat. Namun, pembebasan ion

Nikel adalah salah satu kesan berbahaya berikutan penggunaan bahan ini. Maka, keluli tahan karat bebas nikel (ASTM F2229 atau Cronidur30) dicipta untuk mengatasi masalah ini. Aloi ASTM F2229 bukan sahaja memperbaiki biokeserasian keluli tahan karat 316L tanpa kesan sampingan ion Nikel, malah meningkatkan ketahanan terhadap kakisan dan kehausan. Aloi ini juga mempunyai sifat mekanikal yang lebih baik dalam bendalir tubuh simulasi. Namun, kajian terperinci diperlukan untuk meningkatkan ciri-ciri tribologi, mekanikal, dan bioperubatan aloi ASTM F2229 demi memastikan daya ketahanan implan ortopedik dalam jangka panjang. Oleh itu, kajian ini bertujuan menghasilkan lapisan kaca logam berasaskan ferum (FeCrMoCB) yang menjimatkan kos dan tahan lama untuk menyaluti permukaan ASTM F2229 dengan menggunakan teknologi pelekapan laser. Kaca logam mempunyai ketahanan yang tinggi terhadap kakisan dan kehausan serta sifat mekanikal dan biokeserasian yang sangat baik. Kaca logam berasaskan Ferum boleh didapati dengan mudah dan mempunyai keupayaan pembentukan kaca yang baik. Pelekapan laser merupakan teknologi penyalutan yang berpotensi tinggi kerana teknik ini mampu menyaluti permukaan logam dengan pelbagai jenis bahan, dan memberikan kadar pemanasan dan penyejukan yang diperlukan untuk pembentukan struktur amorfus. Pelakapan laser juga bersih, boleh dikawal, dan teknik ini mengukuhkan pelekatan antara lapisan salut dan substrat melalui ikatan metalurgi yang terbentuk. Kesemua sampel disediakan dengan meratakan serbuk amorf FeCrMoCB ke atas substrat ASTM F2229 bersaiz 30 mm × 30 mm × 3 mm, diikuti oleh penyalutan dengan menggunakan laser diod berkuasa tinggi. Kuasa laser, kelajuan pengimbasan, kekasaran permukaan substrat, peratusan tindihan, dan saiz titik pancaran laser telah dipelbagaikan untuk mengoptimumkan sifat-sifat lapisan salutan. Makrostruktur diperiksa mengunakan mikroskop optik, mikrostruktur

dengan mikroskop pengimbas elektron, transformasi fasa dengan spektroskop sinar-X serakan tenaga. Manakala kekerasan, kelakuan kehausan dalam keadaan kering dan basah (bendalir tubuh simulasi), ketahanan kakisan diperika menggunakan ujian mikrokekerasan dan lekukan nano, ujian kehausan bola-atas-cakera, ujian pengutuban elektrokimia. Sitokeserasian, dan bioaktiviti ujian sel kultur secara langsung, dan rendaman dalam bendalir tubuh simulasi. Hasil kajian menunjukkan bahawa kesemua pemboleh ubah memberi kesan yang ketara terhadap struktur amorfus lapisan salut FeCrMoCB danmempengaruhi sifat mekanikal, tribologi, dan kakisan lapisan salutan tersebut. Struktur komposit amorf-berhablur (kandungan amorfus 76%) memberikan sifat tribologi yang lebih baik berbanding dengan struktur amorfus yang tinggi (kandungan amorf 87%). Lapisan salutan FeCrMoCB mempunyai kekerasan yang lebih tinggi (sehingga 5 kali ganda berbanding dengan kekerasan substrat), kadar kehausan yang lebih rendah dalam keadaan kering dan basah (sehingga sepersepuluh kekasaran substrat), serta peningkatan ketahanan kakisan, dan sitokeserasian yang baik. Bioaktiviti meningkat kerana salutan tersebut berguna sebagai bahan bioaktif perantaraan, mencapai osseointegrasi cemerlang. Kesimpulannya, lapisan FeCrMoCB yang terhasil berpotensi tinggi sebagai implan ortopedik,terutamanya untuk penggantian sendi, dan berpotensi untuk mengurangkan pembedahan ulangan.

Kata kunci;

Penyalutan laser, Bahan kaca logam, Keluli tahan karat bebas nikel, Implan ortopedik

ACKNOWLEDGEMENTS

Firstly, I would like to give my overwhelming gratitude to Allah (the most glorified and most high)

I would like to express my appreciations to my supervisors; Prof. Ahmed Sarhan, Prof. Hamdi and Prof. Farazila for their great support, help and guidance throughout my research work. Also, I would like to express my appreciations to Prof. Kuo who hosted my experimental work in Taiwan and granted me his support and help.

I am highly grateful to my Mother Nahira, my brothers Mostafa and Yahya and a special thanks to my wife Banan for their support and encouragement all the time.

Also, I would like to acknowledge my Uncle Mr. Ashraf Ibrahim for his kind support and care and to all that have a fingerprint in my life and career.

Finally, to my father – May Allah Mercy him – who inspired me and supported me in my academic career.

MAHMOUD

TABLE OF CONTENTS

LIST OF FIGURES

LIST OF TABLES

LIST OF ABBREVIATIONS

a.u.	:	arbitrary unit
P	:	Laser power
v	:	Scanning speed
d	:	Laser beam spot size
OL%	:	Overlap percentage
E_s	:	Specific energy
AC	:	Amorphous content
i_{corr}	:	Corrosion current
E_{corr}	:	Corrosion potential
CR	:	Corrosion rate
K	:	Unit conversion constant for corrosion rate
EW	:	Equivalent weight
P	:	Density
W_r	:	Wear rate
V_{loss}	:	Volume loss
m	:	mass
D	:	sliding distance
F	:	applied normal load

CHAPTER 1: INTRODUCTION

1.1. Introduction

The development of medical implants - used to treat bone fractures and deficiencies - has attracted more attention in the last few decades. The need for implants increased dramatically over the past five years and expected to increase in the coming five years (Orthopedic Implants Market Size | Industry Report, 2024, 2016), Figure 1.1 (the number of revision hip surgery increased by 26% and is predicted to reach 137% in 2030) (Sanli, Arts, & Geurts, 2016). According to the market researches, the expected market value of medical implants will hit the 116 billion USD by 2022 (Tatkare, 2016). In addition, orthopaedic implants occupy 31% of the medical implant global market, Figure 1.2 (Medical Implants Market Global Forecast To 2023 | MRFR, 2018). These reports clarify the increasing and the potential of the medical implant market globally. Also, they reveal the importance of the orthopaedic implants among the other medical implants. From Figure 1.1 and Figure 1.2, it is obvious that joint replacement implants (hip and knee joint replacements) take the majority (more than 70%) of the orthopaedic implants market.

This increasing need lead to more focus on developing more durable implants. A durable medical implant is simply an implant that can be implanted in the human body and kept for a long time without revision surgery and without any harmful side effects. Many materials have been developed for medical implants applications which are termed “biomaterials”.

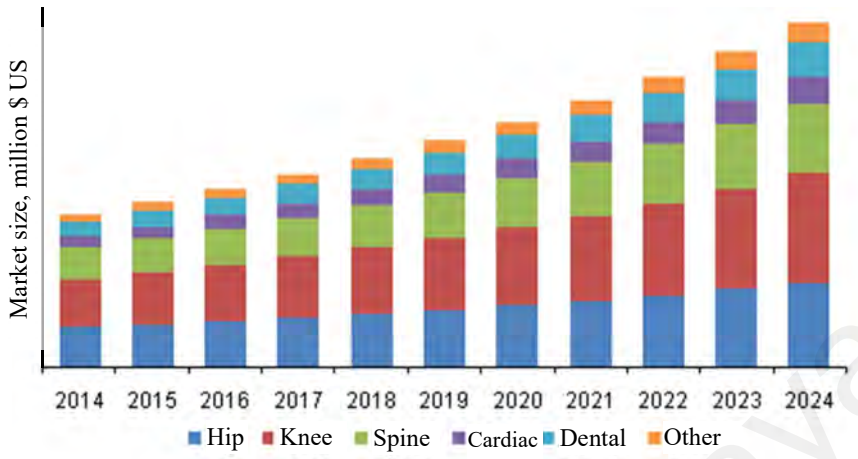

Figure 1.1: medical implants market growth from 2014 to 2024 (Orthopedic Implants Market Size | Industry Report, 2024, 2016)

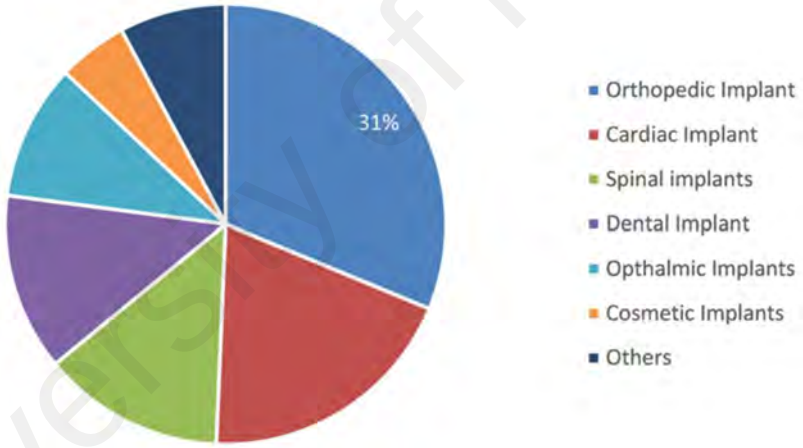

Figure 1.2: distribution of medical implants type in the global market (Medical Implants Market Global Forecast To 2023 | MRFR, 2018)

A biomaterial should be non-toxic, allergy-free, exhibit high corrosion resistance in bio-fluids, good osteoconduction and have acceptable mechanical properties (Goharian & Abdullah, 2017). The term "Biocompatibility" is used to describe the acceptance of a biomaterial in a medical implant. The biocompatibility is defined as "*the ability of a material to perform with an appropriate host response in a specific situation*" (Williams, 2003). According to this statement, the biomaterial properties of concern vary regarding

the application. However, the cytocompatibility or non-toxicity is indispensable. For example, a knee-joint replacement material should prove high wear and corrosion resistance in simulated body fluids, besides acceptable mechanical properties while skull shell implant should prove high osseointegration and osteoconductive properties. A wide range of materials has been considered as biomaterials such as metals, ceramics and polymers to meet the vast applications of implanted devices (Ibrahim, Sarhan, Yusuf, & Hamdi, 2017; Kokubo, 1998; Sharma et al., 2017). According to the market research report issued by Allied Market Research Inc., the metallic biomaterials hold a dominant share in 2014 and is predicted to maintain this lead in the coming four years, Figure 1.3 (Tatkare, 2016).

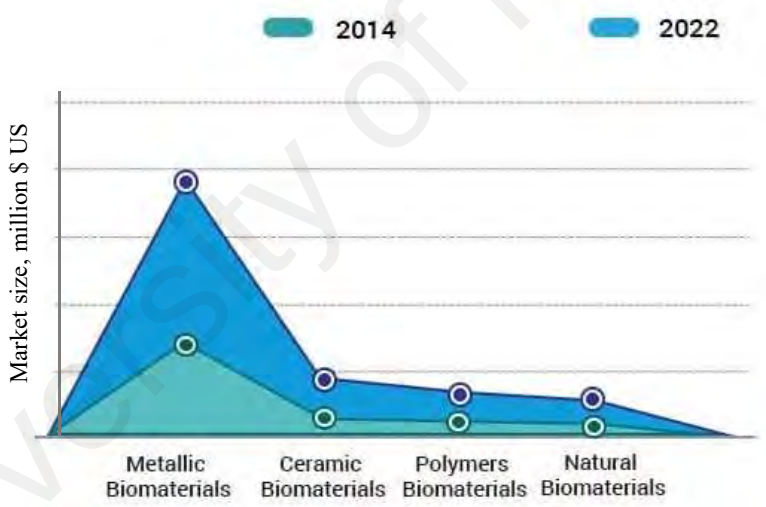

Figure 1.3: biomaterials diversity and their market size (Tatkare, 2016)

After Lister introduced his aseptic surgical technique in 1860's (Asri et al., 2017), the metallic alloys have been developed to be used in medical implants (Asri et al., 2017). The metallic alloys find wider applications in medical implants than pure metals due to their enhanced mechanical properties and tribological properties besides good

biocompatibility which qualify metallic alloys for orthopaedic implants especially the joint replacement applications (Chen & Thouas, 2015).

In 1920's, the stainless steel alloy (18-8 SS) was introduced which, at this time, considered a superior corrosion resistant alloy compared to available alloys (Hermawan, Ramdan, & Djuansjah, 2011). After that time, researchers focused on developing high corrosion resistant materials to be used in the medical application. Currently, the most popular metallic alloys for joint replacement applications are 316L stainless steel, CoCrMo alloy and Ti6Al4V which proved high mechanical properties as well as good biocompatibility, Table 1.1. However, until now, there is no record of successful long-term – or permanent - implantation of the metallic device in the human body (Ibrahim, Sarhan, Yusuf, & Hamdi, 2017b).

Table 1.1: comparison between the common metallic biomaterials

Property	Ti6Al4V	CoCrMo	316L stainless steel
Toxicity of the alloy and elements	Ti is non-toxic V and Al are toxic	Co, Ni, Cr are highly toxic	Iron induces lower toxicity Cr, Ni are toxic
Corrosion resistance	Highest	High	Moderate
Biocompatibility	Highest	Moderate	Reasonable
Wear resistance	Poor	High	Moderate
Mechanical Properties	Excellent	Excellent	Good
Fatigue strength	Poor	Excellent	Good
Cost	Expensive	Most expensive	Inexpensive

Titanium and its alloys attracted more concern recently for their superior specific strength and low toxicity, but in the other side, they have poor wear resistance and low fatigue strength which limits the application of Ti6Al4V in joint replacement implants (Niinomi, 2002). Researchers proposed cobalt-based alloys to be used in the medical application.

Cobalt alloys – especially CoCrMo alloy – proved high strength, high corrosion and wear resistance. Although the toxicity of the Co element, the alloy showed high biocompatibility due to its high corrosion resistance. More studies about the toxicity of released debris should be held (Evans & Thomas, 1986). 316L stainless steel showed a less expensive alternative (up to tenth the cost of Ti6al4V and CoCrMo alloy) with acceptable biocompatibility. In addition, it is approved by the US Food and Drug Administration (FDA) as a short-term implant due to the negative and hazardous effects of Ni ion release (Goharian & Abdullah, 2017). To overcome the Ni-ions release toxicity problem of 316L SS, a nickel-free high nitrogen stainless steel was proposed known as ASTM F2229 or Cronidur30. The proposed alloy proved improved wear and corrosion resistance as well as better mechanical properties, especially in simulated body fluids (Kartik, Veerababu, Sundararamanc, & Satyanarayana, 2015; Ma et al., 2012; Menghua et al., 2014). However, ASTM F2229 does not prove long-term implants, but it is a promising alloy as it is much cheaper than commonly used Co and Ti alloys (SS cost is about tenth the cost of the Ti and Co alloys) (Chen & Thouas, 2015; Ibrahim et al., 2019).

Metallic glasses are newcomers emerging into the metallic biomaterials. Metallic glasses are metallic alloys with randomly-ordered atoms or, in other words, have an amorphous structure. Metallic glasses showed superior mechanical, tribology and corrosion resistance properties due to the absence of crystalline-structure defects such as dislocations and grain boundaries (Löffler, 2003). Recently, many research works considered metallic glasses for biomedical applications as they proved acceptable biocompatibility (Buzzi et al., 2006; Li et al., 2015; Schroers, Kumar, Hodges, Chan, & Kyriakides, 2009; Sun et al., 2014; Wang, Li, Zheng, & Li, 2012). These properties make metallic glasses a promising candidate for biomedical applications. However, the lack of ductility and limited sizes inhibit spreading their applications (Gu, Poon, & Shiflet, 2007).

1.2. Problem statement

Although the great advancement in the biomaterials, no successful long-term metallic implant has been recorded. The metallic biomaterial for joint replacement should offer excellent wear and corrosion resistance, high hardness, suitable mechanical properties and acceptable cytocompatibility behaviour.

ASTM F2229 have acceptable properties – approved by US FDA – with low cost compared to the conventionally used metallic biomaterials. However, ASTM F2229 showed insufficient corrosion, pitting and wear resistance in the long-term and still considered as a temporary implant. In addition, it showed reduced fatigue properties in simulated body fluids (Chen & Thouas, 2015). This may lead to fatigue failure after implantation beside the corrosion failure.

Generally, the drawbacks of stainless-steel alloys are poor wear and corrosion resistance. An upcoming approach to improve the ASTM F2229 surface properties is to develop a coating layer that has superior properties with sufficient adhesion strength to meet the US FDA requirement. Bioceramics coating layer such as Zirconia (ZrO_2), Tantalum oxide (Ta_2O_5), Titania (TiO_2), etc. are proposed as it offers excellent tribology, bio-corrosion, and biocompatibility properties, but the coating process is challenging due to the differences in thermal and physical properties of the metallic alloys and ceramics (Ibrahim et al., 2017). To overcome this challenge, metallic glasses are a promising alternative to the bioceramics. They offer superior wear and corrosion resistance and proved excellent biocompatibility. In addition, they have physical and thermal properties close to that of metallic biomaterials, as well as, matching the chemical composition. Thus, obtaining a defect-free metallic glass coating layer is less challenging and would enhance the biocompatibility of ASTM F2229.

To develop the coating layers, many research works proposed coating techniques such as physical vapour deposition, electrophoretic deposition and thermal spraying to overcome

the prementioned challenges, but these techniques failed to meet the bonding strength (50 MPa) requirement recommended by the US FDA (Mohseni, Zalnezhad, & Bushroa, 2014). As an alternative, laser cladding offers improved wear capabilities over these proposed coating, largely due to its true metallurgical bond that offers greater adhesion than the mechanical bonding of these proposed coating. While these proposed coating can incur delamination from porosity or surface preparation, laser cladding will not delaminate, and its metallurgical bond creates greater separation resistance. The result is often 2-3 times greater product life.

1.3. Objectives

This research aims to:

- Develop a defect-free FeCrMoCB metallic glass coating layer on ASTM F2229 for joint replacement implant.
- Investigate the effects of the substrate surface roughness on the geometry, phase transformation of the laser cladded FeCrMoCB metallic glass coating.
- Enhance the tribology, corrosion and cytocompatibility behaviour of a cost-effective laser cladded FeCrMoCB metallic glass coating in simulated body fluid.
- Verify of FeCrMoCB amorphous metallic glass as promising intermediate bioactive materials for excellent osseointegration in orthopaedic implants.

1.4. Scope of the study

This research work is focusing on developing a novel metallic glass coating layer on ASTM F2229. The proposed coating layer will enhance the tribology and corrosion properties, increase the hardness and have better cytocompatibility to introduce a cost-effective and durable joint replacement implant.

1.5. Outline of thesis

The present thesis includes 5 chapters. Chapter 1 contains an introduction to the issue concerned in the research, the problem statement and the objectives of the research. Chapter 2 includes the literature review of the published work related to the research. Chapter 3 describes the materials and methods utilized in the research as well as the design of the experiment, sample preparations and the investigations made to evaluate the fabricated samples. Chapter 4 lists the results of the investigations made and their analysis, discusses and interprets the results and findings. Chapter 5 includes the conclusions of the research and the recommendations for future work.

1.6. Conclusion

Generally, biomedical bone-implants are attracting more concern due to the increasing market size. The market researches reveal the potential of orthopedics; thus, more concern was directed to develop metallic biomaterials. However, the currently available metallic alloys failed to prove durable and permanent biomedical implants. Many researches focused on developing enhanced biomaterial via application of coating layers with different bioceramics on the metallic biomaterials.

This research is dealing with developing coated biomaterial with enhanced corrosion, wear and biocompatibility properties.

CHAPTER 2: LITERATURE REVIEW

2.1. Introduction

Biomedical bone-implant material should meet the biocompatibility requirements as well as the mechanical properties requirement. The biocompatibility requirements include sufficient corrosion resistance, cytocompatibility, no dangerous or harmful ion-release, and non-allergy or side-effect when implanted. On the other side, the material should withstand the mechanical loads – both static and dynamic – and exhibit good wear resistance, especially for joint replacements. It is well-known that no perfect material for bone-implants until now. Generally, the most common metallic alloys used in bone-implants are stainless-steels (SS), Titanium (Ti) alloys and Cobalt (Co) alloys.

This chapter covers the properties and characteristics of the common metallic biomaterials as well as the metallic glasses as a potential candidate for biomedical applications. Also, this chapter discusses the development of techniques to enhance and promote the biomedical properties of the currently used metallic biomaterials.

2.2. Historical background

The first recorded implant alloy developed for human was “Sherman Vanadium Steel” (Metallic Implant Materials, 2007). This alloy failed to last for long time due to rapid corrosion in human body. In 1920’s, the stainless steel alloy (18-8 SS) was introduced which, at this time, was considered superior anti-corrosion to available alloys (Hermawan, Ramdan, & Djuansjah, 2011). After that time, researchers focused on developing high corrosion materials to be used in biomedical applications. Later, 316L SS, Co-alloys and Ti-alloys were introduced and proved excellent mechanical properties as well as good biocompatibility. Biocompatibility is a term used to describe the behavior

of a material dealing with living tissue, which is non-toxic, not releasing harmful elements and not causing allergic effects (Goharian & Abdullah, 2017).

Studies showed that metallic substrates release metal ions which may be considered toxic and hazardous. Also, the metals induce poor bioactivity which means metals do not form chemical bond with living tissues. By the 1930's, polymers were used in biomedical applications, but were limited in load bearing applications for their poor mechanical properties compared to metals. In 1970, Larry Hench introduced bioactive glass (Moritz et al., 2004) which showed excellent bioactivity. However, the fracture toughness of bioactive ceramics (0.5 to 2 MPa.$m^{1/2}$) lacks that of bones (10-30 MPa.$m^{1/2}$) (Ibrahim, Sarhan, Yusuf, & Hamdi, 2017). Then, a progressive advancement was directed to bioactive ceramics as hydroxyapatite. Figure 2.1 shows the development of implants materials in the last century (Niinomi, 2002).

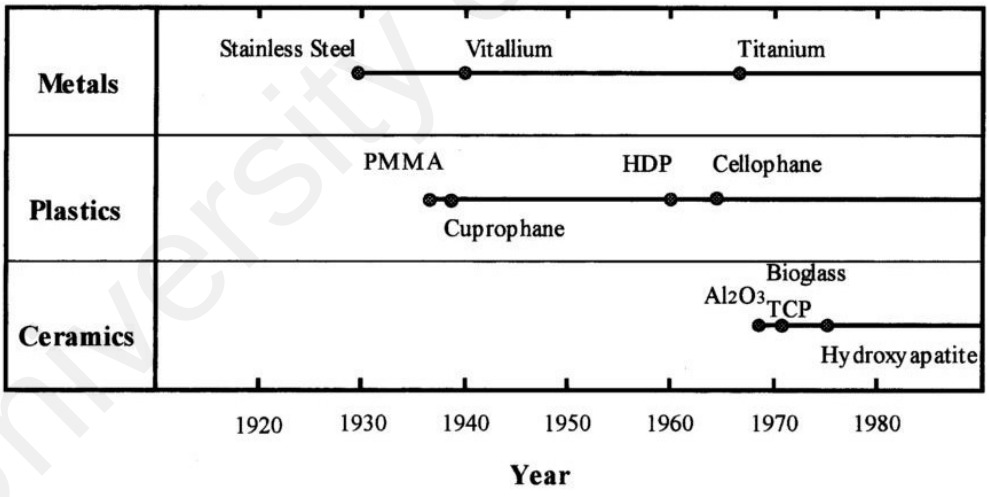

Figure 2.1: History of implants materials development (Niinomi, 2002)

In the next sections, the most common metallic alloys used in biomedical implants and the techniques developed to improve the performance of the implants will be reviewed.

2.3. Metallic alloys in biomedical implants

After the discovery of iron, humans used iron in food containers and other usages. Silver and gold were used in bone implants and dental replacement. In fact, the materials dealing with living tissues should meet the following requirement; non-toxic, high corrosion resistance, accepted by living tissues and have suitable mechanical properties as hardness, ultimate tensile strength (UTS), fatigue limit, and Young's modulus.

Generally, there is no perfect inert metal or in other words doesn't corrode in the human body. So, the metals and their alloying elements are evaluated according to their toxicity level and durability in the human body. As a fact, metals exist in human body for certain functions. Normal concentrations of different elements are listed in Table 2.1 (Q. Chen & Thouas, 2015). These elements when exceed certain levels, they become harmful. The human body is highly corrosive media, so as the metals corrode, hazardous metal ions released (Yamamoto, Honma, & Sumita, 1998).

Usually, the metallic implants failed to prove durability and long-term due to severe bio-corrosion. Developments and improvements were made to the alloys to increase their corrosion resistance. The corrosion of implant can be minimized as follows:

- Usage of appropriate metals.
- Avoiding implantation of different types of metal in the same region. This reduces the electro-chemical corrosion.
- Design the implant to minimize notches, pits and crevices.
- Recognizing that metal corrosion resistance is not the same all over the body.

Table 2.1: Metallic elements in human body, their functions, and normal concentrations

Metallic element	Function	Normal concentrations
Iron (Fe)	Contained in heme groups of hemoglobin and myoglobin which are required for oxygen transport in the body. Anemia is the primary consequence of iron deficiency. Excess iron levels can enlarge the liver, may provoke diabetes and cardiac failure.	4-5 g in body (Nantel & Tontisirin, 2001)
Copper (Cu)	Contained in enzymes of the ferroxidase system which regulates iron transport in the blood and facilitates release from storage. A copper deficiency can result in anemia from reduced ferroxidase function. However, Cu is considered a highly toxic element.	0.9-2.8 µg/L (Kubala-Kukuś et al., 2014)
Zinc (Zn)	Important for reproductive function due to its role in FSH (follicle stimulating hormone) and LH (leutinizing hormone). Required for DNA binding of zinc finger proteins which regulate a variety of activities. An excess of zinc may cause anemia or reduced bone formation.	2 g in body (Nantel & Tontisirin, 2001)
Manganese (Mn)	Major component of the mitochondrial antioxidant enzyme manganese superoxide dismutase. A manganese deficiency can lead to improper bone formation and reproductive disorders. An excess of manganese can lead to poor iron absorption	2-4 mg/day in body (Crossgrove & Zheng, 2004)
Cobalt (Co)	Contained in vitamin B12. Co has high toxicity.	0.3 to 0.9 µg/L (Okazaki & Gotoh, 2005)
Molybdenum (Mo)	Required for the excretion of nitrogen in uric acid in birds. An excess can cause diarrhea and growth reduction.	0.6-13.1 µg/L (Burguera & Burguera, 2007)
Chromium (Cr)	A cofactor in the regulation of sugar levels. Chromium deficiency may cause hyperglycemia (elevated blood sugar) and glucosuria (glucose in the urine). Elevated levels of some forms of chromium, such as Cr(VI), can be carcinogenic	0.4-0.6 µg/L (Okazaki & Gotoh, 2005)

2.3.1. Stainless steel alloys (SS)

Stainless steel is iron-based alloy. The alloy contains Cr, Ni, Mo, Mn, Si, Cu, and carbon. Stainless steel is featured for its high corrosion resistance when first revealed in the early of 20th century. This feature is referred to the formation of chromium oxide film which is stable and prevents further oxidation. In 1930's, clinicians used 18-8 SS as biomedical implants, but it failed to prove durability due to rapid corrosion. Further developments were carried out to enhance the corrosion resistance and new SS alloys were presented.

2.3.1.1. 316L Stainless Steel

A further development of 18-8 SS has been done by adding Ni. It is found that the corrosion resistance is enhanced when Ni is added, and this called 316 SS. After that, it was found that the carbon causes the formation of chromium carbides which is located at the grain boundaries leading to localized corrosion. So, decreasing the carbon content improved the corrosion resistance of the SS, and 316L SS is introduced (Q. Chen & Thouas, 2015; "Metallic Implant Materials," 2007). Chemical composition of 316L SS are shown in Table 2.2.

.

Table 2.2: Chemical composition of 316L SS, compositions presented are in % wt. (Luo et al., 2016)

Material	Fe	Cr	Ni	C	S	P	Si
316L SS	Balance	16.0-18.0	10.0-14.0	0.03	0.03	0.045	1.0

For long years, 316L SS was considered for biomedical devices and implants used in trauma surgeries (Plecko et al., 2012), Figure 2.2 shows examples for biomedical implants made from 316L SS in (a) knee replacement and (b) ankle replacement (Q. Chen & Thouas, 2015). 316L is featured for its accepted mechanical and tribology properties as well as biocompatibility. The mechanical properties of 316L SS is shown in Table 2.3. Also, the 316L has high ductility, cheap and can be easily manufactured.

Until now, 316L SS is the most common used alloy in biomedical implants due to its low cost, accepted biocompatibility and good mechanical properties (Galván, Larrea, Braceras, Multigner, & González-Carrasco, 2016). Moreover, 316L are approved by the US FDA as a temporary implant.

Figure 2.2: Examples of 316L SS implant in (a) knee, (b) ankle (Q. Chen & Thouas, 2015)

Table 2.3: Mechanical properties of 316L SS (Yazdipour & Heidarzadeh, 2016)

Material	UTS, MPa	Yield strength, MPa	Modulus of Elasticity, GPa
316L SS	1170	480	190-200

The studies showed the high risk of releasing of Ni ions in human body which result from the bio-corrosion of 316L SS, but Ni is important in 316L SS as it stabilizes the austenitic phase (austenitic SS is preferred rather than martensitic SS in implants) (Mansur, Wang, & Berndt, 2013).

Although the proposed high corrosion resistance of 316L SS, they showed poor durability as an implant in human body. Normally, they corrode rapidly when implanted and corrosion failures take place as shown in Figure 2.3. So, their applications are limited in medical devices or short-term implants (Q. Chen & Thouas, 2015; Hermawan et al., 2011). Also, the release of Ni ions, which induced by 316L SS alloy, may cause severe adverse effect on the human health. Further development introduced a Ni-free SS alloy with enhanced properties.

Figure 2.3: Corrosion failure of SS Hip joint stem implant (Q. Chen & Thouas, 2015)

2.3.1.2. Ni-free, high nitrogen Stainless-Steel (ASTM F2229)

New developments were investigated to enhance the biocompatibility of 316L by replacing Ni with high concentration of nitrogen. Nitrogen was found to act as austenitic phase stabilizer replacing hazardous Ni. So, Ni-free, high concentration nitrogen SS (ASTM F2229) was developed (Table 2.4 shows compositions (in wt.%) of ASTM F2229) (Ibrahim et al., 2017). The ASTM F2229 SS proved better pitting corrosion, wear and corrosion resistance than conventional 316L SS (Muley, Vidvans, Chaudhari, & Udainiya, 2016). Besides, it showed enhanced fatigue strength and hardness (Kartik, Veerababu, Sundararamanc, & Satyanarayana, 2015; Niinomi, 2002). The developed alloy has great potential in biomedical applications, but still need further studies to evaluate its biomedical properties (T. Ma et al., 2012; Menghua et al., 2014).

From Figure 2.4, the developed Ni-free SS has enhanced bio-corrosion, as well as, enhanced fatigue resistance and excellent cytocompatibility near to commercial pure titanium, Figure 2.5 (Niinomi, 2002).

Table 2.4: Composition (in wt. %) of 316L SS and Ni-free, high nitrogen SS (ASTM F2229) (Ibrahim et al., 2017)

Stainless Steel type	Cr	Ni	Mo	Mn	Si	Cu	N	C	P	S
ASTM F2229	19.00-23.00	0.10	21.00-24.00	0.50-1.50	0.75	0.25	>0.90	0.08	0.03	0.01

2.3.1.3. Mechanical and biocompatibility properties of SS

The nature of loads is static and dynamic. The dynamic load is more critical as the most of implants fail due to lack of fatigue strength. Normally, the implants are directed to corrosion and pitting corrosion due to the aggressive behavior of the human body which affects the fatigue resistance.

Generally, SS-alloys are reliable in terms of fatigue resistance. However, the alloy showed reduced fatigue properties (by about 20% of dry fatigue strength) when subjected to corrosive media, Figure 2.6 (Q. Chen & Thouas, 2015). As a fact, SS is very sensitive to fatigue failure in corroding environment, which increase the possibility of failure due to fatigue.

SS has poor pitting and crevice corrosion resistance because of the chromium carbides formed on the grain boundaries (Muley et al., 2016; P. Zhang & Liu, 2016). So, SS implants failures which were reported because of fatigue failures, was due to initiation of cracks at very poor surface finish and crevice corrosion sites. However, the developed ASTM F2229 proved better crevice corrosion resistance because of the addition of nitrogen, but still need more investigations (Talha, Behera, & Sinha, 2013).

Table 2.5 compares the mechanical properties of 316L SS and ASTM F2229 (Ibrahim et al., 2017). Another point is the inferior wear resistant of SS alloy which caused by debris release and reduce life (Niinomi, 2002) although the 316L SS showed reduced wear rate under simulated body fluid (SBF) (Yu Wang, Shi, Duan, Li, & Xu, 2014).

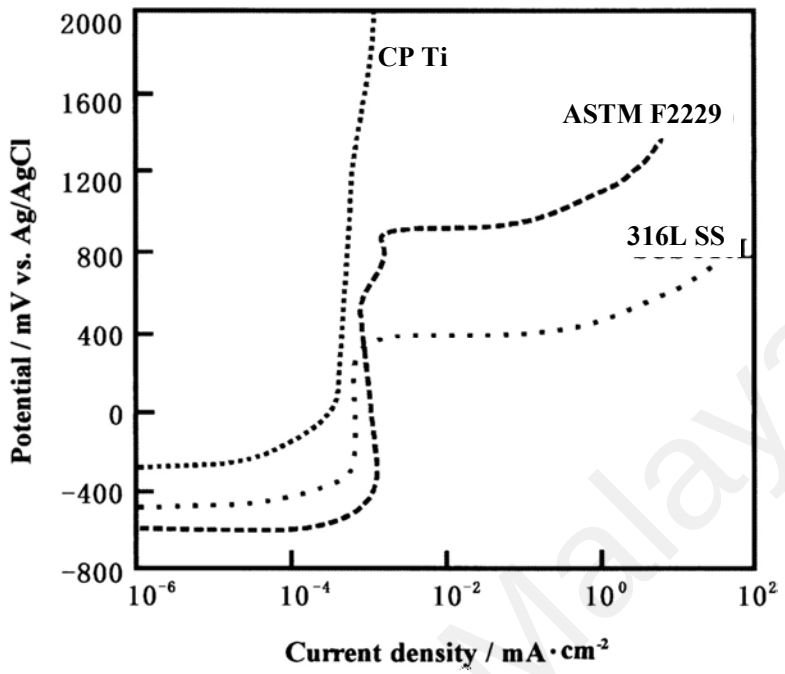

Figure 2.4: Potential/current density curve for 316L SS, ASTM F2229 SS and CP Ti (Niinomi, 2002)

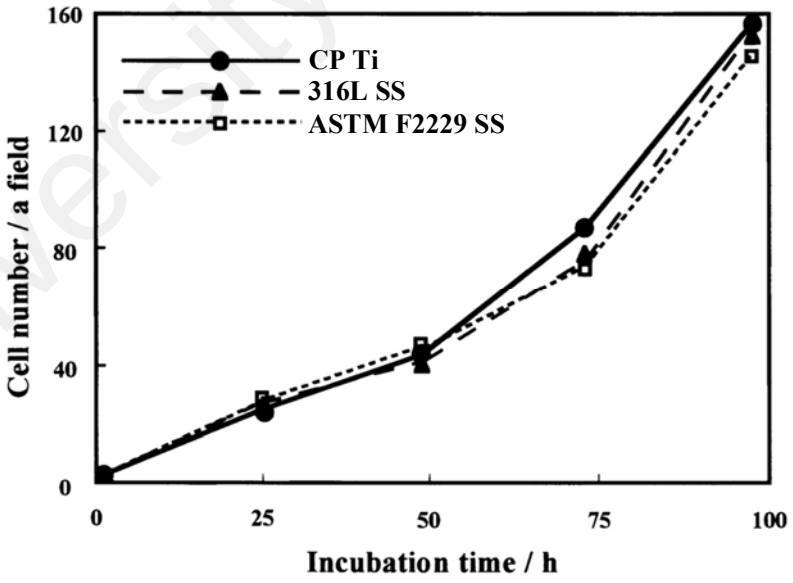

Figure 2.5: Cell growth obtained on ASTM F2229 SS, 316L SS and CP Ti (Niinomi, 2002)

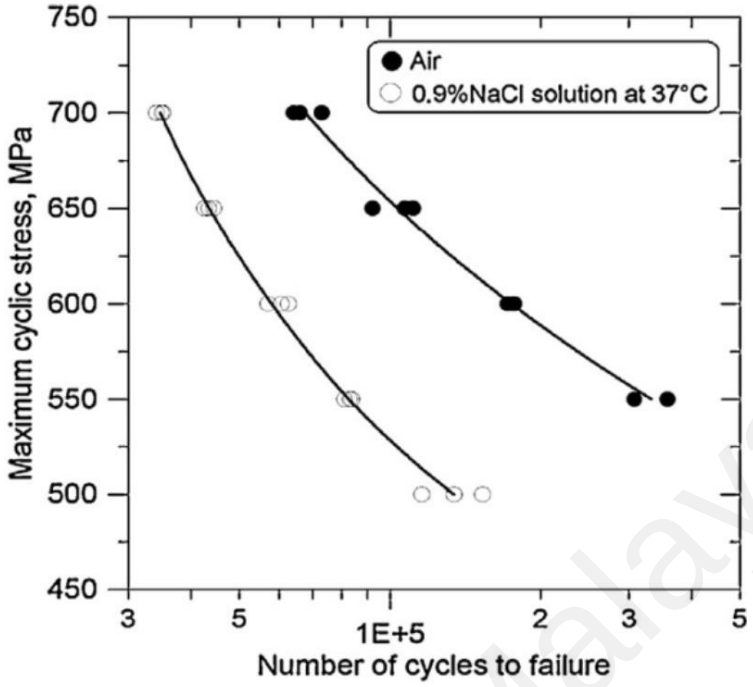

Figure 2.6: ASTM F2229 SS fatigue performance in air and in 0.9% NaCl solution (Q. Chen & Thouas, 2015)

As a conclusion, SS alloys are featured to be relatively cheap alloy, have suitable biocompatibility, and exhibit good mechanical properties. In addition, it is widely used and is approved from the US FDA as temporary biomedical implant material (Dewidar, Khalil, & Lim, 2007; L. Huang et al., 2015).

Table 2.5: Mechanical properties of 316L SS and ASTM F2229 (Ibrahim et al., 2017)

Stainless Steel type	UTS, MPa	Yield strength, MPa	Fatigue strength in air	Fatigue strength in PBS	Hardness, HRC	Max elongation, %
316L SS (ASTM F138)	490-1350	190-690	220-600	220-600	25-39	12-40
ASTM F2229	931-1731	586-1551	650	500	43-50	12-52

**The fatigue strength measured at 10^7 cycles*

On the other side, SS alloys have poor bio-corrosion resistance and pitting corrosion resistance, reduced fatigue performance in corroding media, no bioactivity, and poor wear resistance. Even the developed ASTM F2229 proved better properties (as fatigue, wear and corrosion resistance, no Ni ion release) to replace the 316L SS, but it still lacks to prove durable implant. Further studies are needed to ensure the biocompatibility of this alloy.

2.3.2. Cobalt alloys

In the early of 20th century, the CoCrMo alloy presented and was employed in aircraft applications. The alloy includes Co as base metal, Cr, Mo, W, C, and Ni as alloying elements, the role of alloying elements is listed in Table 2.6. The alloy showed great corrosion and wear resistance and excellent mechanical properties (UTS, fatigue strength, Young's Modulus) even at elevated temperatures. The alloying elements Cr, Mo, and Ni are responsible for the excellent wear and corrosion resistance (Q. Chen & Thouas, 2015). In 1940s, the alloy found the first application in biomedical implants in dental application. After that, the alloy was developed and utilized in orthopedics and joint replacements (Figure 2.7 shows knee replacement made of CoCr alloy) because of their excellent wear resistance and galvanic properties (Plecko et al., 2012; Pramanik, Agarwal, & Rai, 2005).

Table 2.6: Roles of various alloying elements in Co-alloys (Ibrahim et al., 2017)

Alloying element	Rule in Co-alloy
Cr	Enhance wear and corrosion resistance
Ni	Enhance corrosion resistance, increase strength, and castability
Mo	Enhance corrosion resistance and increase strength
C	Enhance wear resistance and increase cast ability
W	Enhance strength, but decrease corrosion fatigue strength and corrosion resistance

Figure 2.7: Knee replacement made from CoCrMo alloy (Ibrahim et al., 2017)

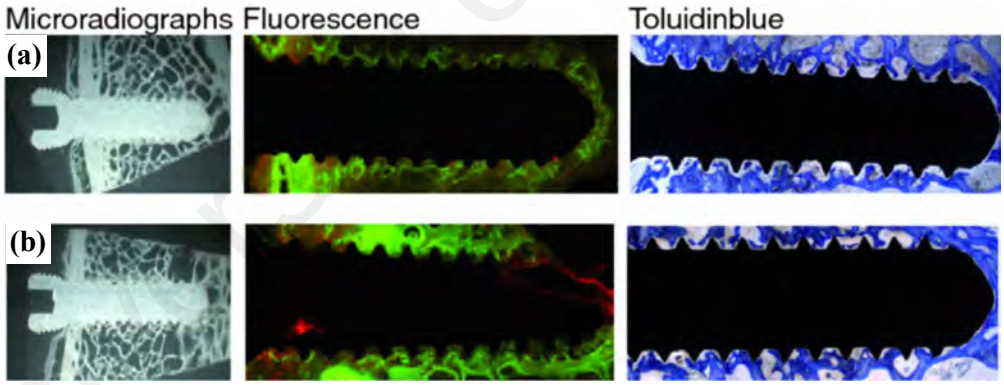

Figure 2.8: Bone sections after removing screw implants (a) CoCr alloy, (b) Stainless Steel (Plecko et al., 2012)

2.3.2.1. Biocompatibility of Co-based alloys

Although Co, Cr, and Ni are classified as high toxic elements (Yamamoto et al., 1998), the alloy CoCrMo showed high biocompatibility due to its high corrosion resistance which limits the ion release of toxic elements (Evans & Thomas, 1986). Co-based alloys

succeeded in biomedical implants and considered as permanent implant replacing SS alloys, besides the superior mechanical properties. Co-based alloys replaced 316L SS in joint replacement as they exhibit excellent wear resistance. However, in long term the metal-on-metal contact results in debris which release cobalt and chromium ions in the human body causing severe adverse effects (Evans & Thomas, 1986).

Moreover, CoCrMo alloy showed low osseointegration and exhibited no bioactivity beside the cost, which is great challenge for Co-based alloys (Plecko et al., 2012). M. Plecko et al. investigated the osseointegration of different metals. The results showed poor osseointegration, even lower than stainless steel, which brings a new limitation for CoCr-alloys. Figure 2.8 shows the fluorescence and toluidine-blue dye of bone-section after removal of screw implant. The figure shows lower new cells developed at the interface in the case of CoCr implant (the grey color represent the old bone cells and the blue color represent the new cells formed) (Plecko et al., 2012). For this reason, further studies should be held to evaluate the toxicity, biocompatibility and osseointegration of the Co-alloys.

2.3.2.2. Mechanical Properties of Co-based alloy

CoCrMo alloys are widely used in biomedical implants for their high wear resistance and high hardness. Also, they exhibit high mechanical strength (UTS 960 MPa), Table 2.7 compares the mechanical properties of Co-alloys and ASTM F2229, and high polishing surface quality which enhance the corrosion resistance and minimize the pitting and crevice corrosion. They have excellent fatigue resistance behavior (10^7 cycles at 610 MPa) even when notched, and can be improved by post treatments (the fatigue strength is increased by 100% to 120%), Figure 2.9 shows superior fatigue behavior of forged and HIP Co-alloys over 316L SS (Odahara, Matsumoto, & Chiba, 2008). They showed

excellent fatigue resistance when subjected to corroding media, Figure 2.10 (Q. Chen & Thouas, 2015).

Table 2.7: Mechanical properties comparison between Co-alloys and ASTM F2229 (Ibrahim et al., 2017)

Material	UTS, MPa	Yield strength, MPa	Fatigue strength in air, MPa	Fatigue strength in PBS	Hardness, HRC	Max elongation, %
Co-alloys	650-1900	450-1610	200-950	100-200	47	12-50
ASTM F2229	931-1731	586-1551	650	500	43-50	12-52

However, Co-alloys has poor fatigue strength in physiological solutions – 100-200 MPa which is marginally unsafe compared to the loadings for arms and legs which may reach 200 MPa – which result in lower success rate of Co-alloys implants after 20 years (Q. Chen & Thouas, 2015).

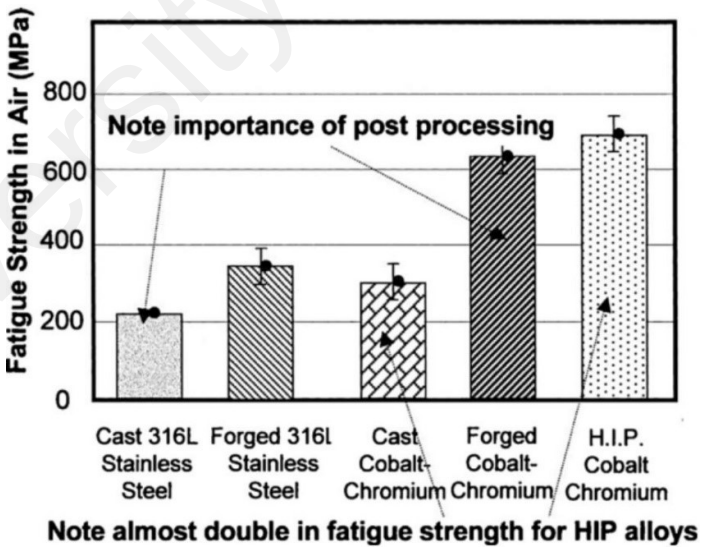

Figure 2.9: Fatigue strength of SS and Co-Cr alloys (Q. Chen & Thouas, 2015)

As a conclusion, the main features of CoCrMo alloy are excellent corrosion resistance, excellent wear resistance, superior mechanical properties, and high fatigue resistance in air. These features make Co-alloy excellent for biomedical applications (it occupies about 20% of the joints replacement - hip and knee joints - market). However, Co-alloys have low ductility, poor fatigue in physiological solutions, increased cost, need expensive fabrication processes are the main drawbacks, and may induce hazardous metals ion release. In addition, they have high density (9.8 gm/cm^3) alloys and may release toxic metal particles. These drawbacks limit the increasing use of Co-alloys in biomedical implants. One of the other issues facing Co-alloys is the implant failure due to fretting fatigue. However, CoCrMo alloy is still the most popular alloy used in joint replacements because of the excellent wear and corrosion resistance (Q. Chen & Thouas, 2015; Yu Wang et al., 2014).

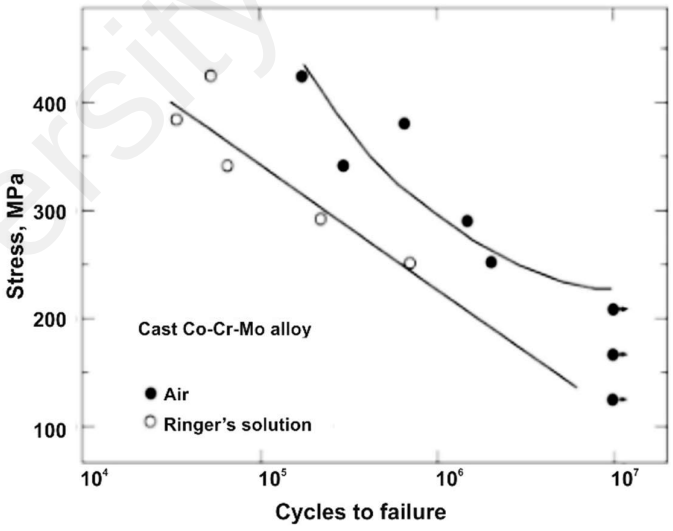

Figure 2.10: Fatigue performance of Co-alloy in air and physiological solution (Q. Chen & Thouas, 2015)

2.3.3. Titanium alloys

Titanium (Ti) alloys were first introduced as structure material in aerospace application. Later, in 1950 Ti-alloys were employed as dentistry implants. After that, it became of great interest to be used in bone implants (Niinomi, 2002). Ti is considered non-toxic, even at high doses, to the human body (Chien, Liu, Kuo, Wu, & Hong, 2016; Moritz et al., 2004; Zalnezhad, Baradaran, Bushroa, & Sarhan, 2014).

Titanium is low density metal (4.8 gm/cm^3) which offers superior specific strength over other common alloys. Pure titanium can be used, but for limited application because of their relatively insufficient mechanical and fatigue strength, however, studies showed that titanium fatigue performance is not affected in corroding media (Niinomi, 2008). This makes high potential for using titanium in biomedical applications. To enhance the mechanical properties, the titanium is strengthened by adding alloying elements as Al, V, Nb, Zr, Mo, etc. (Niinomi, 2008). Ti6Al4V is one of the most common alloys used in biomedical applications for its excellent mechanical properties.

2.3.3.1. Biocompatibility of Ti-alloys

Ti alloys – especially Ti6Al4V – proved excellent corrosion resistance and biocompatibility. The in vitro and in vivo tests showed that Ti element is safe for human body and possess good osseointegration (the formation of a direct interface with bones without intervening soft tissues), Figure 2.11 shows the infusion at the interface between host bone and Ti implant.

It is noted that Ti has excellent biocompatibility and exhibit the highest polarization resistance, which resulted on great concern on developing Ti-alloys, Figure 2.12 shows the biocompatibility of different metallic element (Niinomi, 2002). It is however should be noted that Al and V are reported to have allergic effect on the human body. So, development of second generation of Ti alloys was proposed by replacing Al and V with

Zr, Ta, and Mo which are considered relatively safe for human body (Niinomi, 2002, 2008). Alloys Ti6Al7Nb, Ti5Al2.5Fe, Ti15Zr4Nb2Ta, etc. were developed for biomedical applications as they are allergy-free alloys. However, these alloys contains elements with different specific weight and melting point causing non-homogeneity of the casting which requires advanced manufacturing processes (Niinomi, 2002).

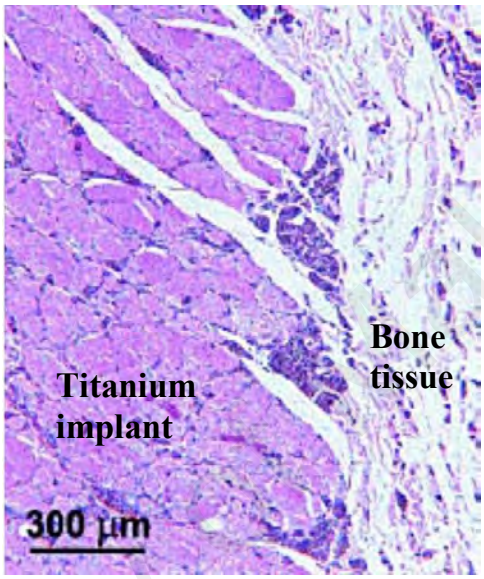

Figure 2.11: infusion at the interface between bone and Ti implant (Q. Chen & Thouas, 2015)

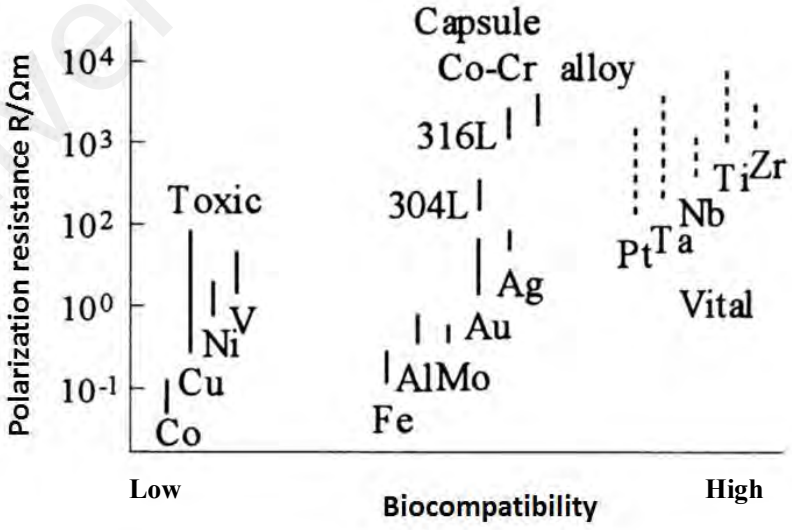

Figure 2.12: Biocompatibility and polarization resistance of metals (Niinomi, 2002)

2.3.3.2. Mechanical properties of Ti-alloys

Generally, with low density and strength (500 MPa) comparable to that of 316L SS, the most featuring property of Ti-alloy is their superior specific strength (288 N.m/kg while 63 N.m/kg for SS) and have relatively low Young's Modulus (80 GPa) which is near to the value of cortical bones (Q. Chen & Thouas, 2015; Niinomi, 2008). Table 2.8: Mechanical properties of pure Ti and Ti6Al4V alloy. This reduces the effect of stress shielding which may cause the release of implant form the bones. The Ti-alloy proved no change in fatigue behavior in physiological solutions (Figure 2.13 shows that the fatigue strength remains the same in air and in physiological solutions). However, Ti-alloy is sensitive to fretting fatigue which is about half the plain fatigue strength (Niinomi, 2008). This property causes the fracture of Ti implants, for example, at the neck of THR in Figure 2.14.

Table 2.8: Mechanical properties of pure Ti and Ti6Al4V alloy (Ibrahim et al., 2017)

Material	UTS, MPa	Yield strength, MPa	Fatigue strength in air*, MPa	Fatigue strength in PBS	Hardness,	Max elongation, %
Pure Ti	241-550	172-480	120-275	100-200	70-100 HRB	15-24
Ti6Al4V	896	827	250-300	250	30-39 HRC	10

* *Fatigue life measured at 10^7 cycles*

On the other side, titanium is very poor in wear resistance, poor hardness and exhibits low tensile ductility and low bending strength which made Ti-alloys fail to prove long-term implant especially in total hip replacement (Figure 2.14 shows fracture of Ti implant due to fretting fatigue) (Q. Chen & Thouas, 2015). The implants made of titanium should have high surface quality because its fatigue resistance is very sensitive to surface conditions and the fatigue strength may be reduced up to 40% when notched (Q. Chen & Thouas, 2015).

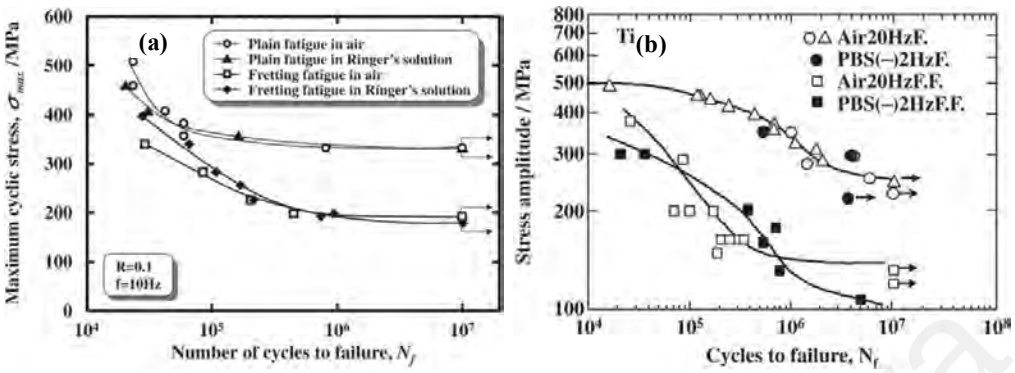

Figure 2.13: Fretting fatigue and plain fatigue of (a) TiNbTaZr alloy, (b) Ti6Al4V alloy (Niinomi, 2008)

Figure 2.14: Fracture of Ti hip joint implant

As a conclusion, Ti-alloy is featured for its high specific strength compared to SS and Co-alloys, low density, high corrosion resistance, and superior biocompatibility and osseointegration. However, Ti-alloy drawbacks are their relatively high cost, poor forgeability, highly sensitive fatigue strength to notches and insufficient bending strength, low hardness, and low wearing resistance. These drawbacks limit the application of Ti-alloy in long-term load bearing implants and in joints, however, it is highly promising alloy for other biomedical applications (Niinomi, 2008). Until now, there is a lack of long-term application of Ti-alloys in clinical applications due to low wear resistance and inferior both fatigue and fretting fatigue strength.

2.4. Metal based amorphous alloys (Metallic Glass)

Recently, amorphous metallic alloys or Metallic Glass (MG) came to concern because of their superior mechanical properties and excellent tribology and corrosion behavior. MGs do not have crystalline structure as conventional solidified metals, Figure 2.15. MG was first introduced in 1950's by very high cooling rate (10^4-10^7 °C/s) from the vapor or liquid state. At this time the applications were limited because of limited sizes obtained (Hofmann, 2013). Certain studies succeeded to obtain amorphous phase at lower cooling rate through using certain combinations of alloying elements – depending on the size of the atoms used – enabling producing much bigger sizes (up to few centimeters) (Hofmann, 2013). Recently, it is proved to obtain amorphous alloys by using different techniques as ion implantation, electrodeposition or mechanical alloying (Kwon, Kim, Kim, Lee, & Fleury, 2006). Figure 2.16 shows the development in MG systems and the improvements in obtained sizes (Ibrahim et al., 2017).

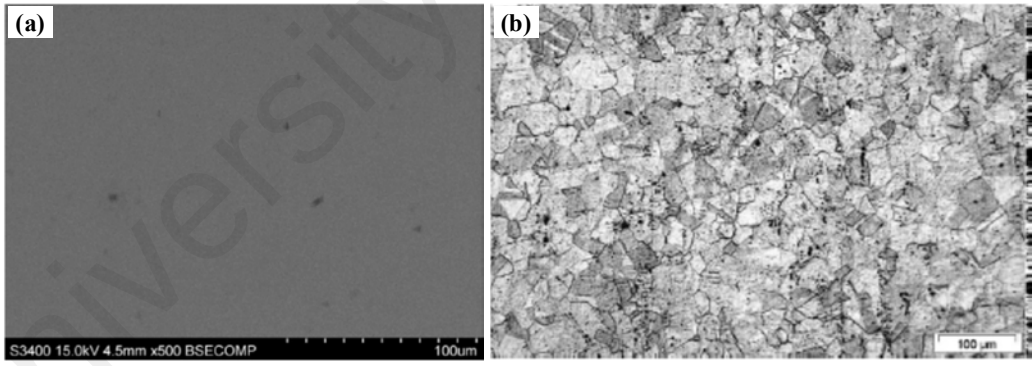

Figure 2.15: SEM of (a) Zr-based MG (Espallargas, Aune, Torres, Papageorgiou, & Muñoz, 2013), (b) 304 SS (Ezazi et al., 2015)

The amorphous systems can be categorized as ferrous and non-ferrous alloy systems. The ferrous alloy system (Fe-Si-B-Nb, Co-Fe-Si-B-Nb, Ni-Si-B-Ta, etc.) are featured for their high magnetic properties which can be employed in transformers and another

electromagnet equipment. The non-ferrous alloy systems are employed in different applications like sport, electronics, medical and foundry equipment.

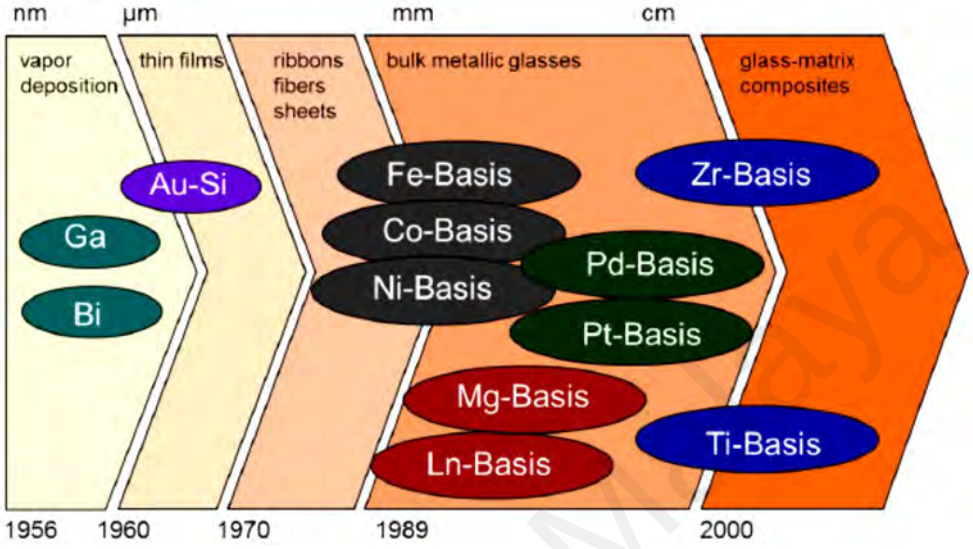

Figure 2.16: Historical development in MG systems and obtained sizes (Ibrahim et al., 2017)

Recently, the MGs have high potential to be applied in biomedical applications. They can be categorized as biodegradable, like Mg, Ca, and Zn based MGs, and non-biodegradable MGs, like Fe, Ti, and Zr, based MGs (H. F. Li & Zheng, 2016). It was found that MGs have excellent mechanical properties as high strength, high wear resistance as well as superior corrosion resistance and excellent biocompatibility (Buzzi et al., 2006; C. H. Huang et al., 2015; D. Li et al., 2017; S. Li et al., 2015; Schroers, Kumar, Hodges, Chan, & Kyriakides, 2009; Zhou, Zhang, Wang, Yasir, & Liu, 2015). Hence, Fe, Ti, Zr based MGs are potential candidatures for bone-implants applications.

2.4.1. Fe-based MG

The Fe-based MG are available and cheap (H. X. Li, Lu, Wang, Wu, & Lu, 2019), which make it attractive in different applications, besides their good glass-forming ability (GFA) allowing production of larger geometries. Fe-based MG became a promising candidate

for their superior mechanical properties, wear, and corrosion resistance besides, good cytocompatibility.

2.4.1.1. Mechanical properties of Fe-based MG

The Fe-based MGs exhibited excellent mechanical properties. They have high ultimate tensile strength, yield strength, and high hardness. X.J Gu et al. evaluated the mechanical properties of non-ferromagnetic Fe-based MG. The results revealed that the constitution of the alloy affects its strength as well as their elasticity and plasticity (Gu, Poon, & Shiflet, 2007). The authors studied 23 different Fe-based MG alloys and the results obtained are summarized in Table 2.9 compared with ASTM F2229 SS and CoCr alloy. The mechanical properties of Fe-based MG are outstanding, but it exhibited small elongation until fracture with limited bulky sizes (up to 16mm in diameter).

Table 2.9: the mechanical properties of Fe-based MG with ASTM F2229 and CoCr alloy (Ibrahim et al., 2017)

Material	Yield strength, MPa	UTS, MPa	Plastic strain, %	Vickers Hardness, GPa
Fe-based MG	3400-3800	3800-4400	0-0.8	8-11
ASTM F2229 SS	586-1551	931-1731	12-52	0.42-0.51
Co-based alloy	560	960	20	0.47

An important mechanical property required in biomedical implant is the fatigue strength. Normally, the crystalline alloys exhibit endurance limit (maximum stress for 10^7 cycles) about 0.4-0.6 of their fracture strengths. D.C. Qiao et al. studied the fatigue behavior of Fe-based MG ($Fe_{48}Cr_{15}Mo_{14}C_{15}B_6Er_2$) and found that its fatigue strength is considerably high (682 MPa), but with lower endurance limit/tensile strength (4.4 GPa) ratio (0.155). However, the material failed abruptly when the endurance limit is exceeded. Figure 2.17 shows the fatigue behavior of Fe-based MG (Qiao et al., 2007).

Another consideration is the wear resistance under dry and wet conditions. The Fe-based MG showed excellent wear resistance under dry conditions (An et al., 2014; Z. Li, Zhang, & Liu, 2015; Lu et al., 2018; Segu, Choi, Yi, & Kim, 2012). However, there is a lack in investigating the performance of Fe-based MG in SBF environment.

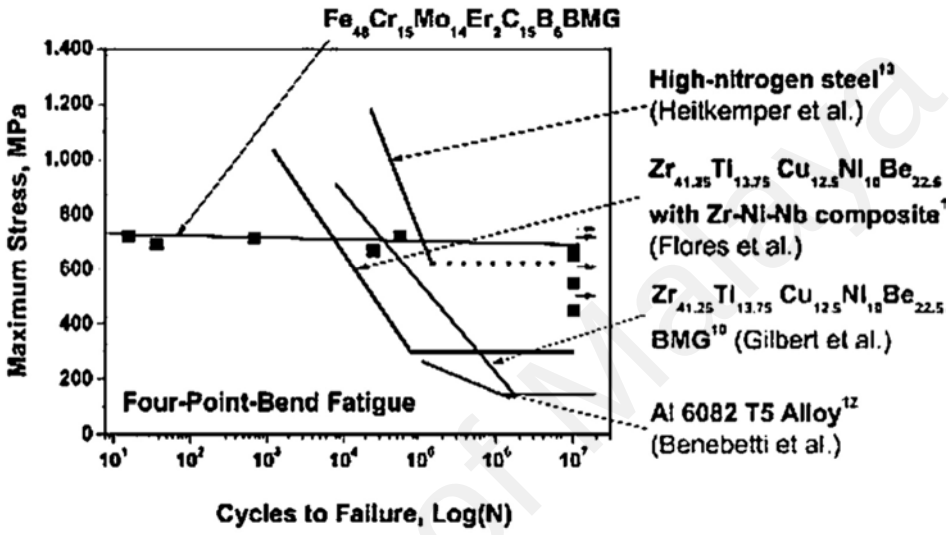

Figure 2.17: compares the fatigue behavior of Fe-based MG, Zr-based MG, High nitrogen steel, and Al-alloy (Qiao et al., 2007)

2.4.1.2. Biocompatibility of Fe-based MG

Fe-based MGs are reported to exhibit enhanced biocompatibility than SS due to its promising corrosion resistance and mechanical properties, especially in SBF. In addition, the developed non-ferromagnetic Fe-based MG is nickel free, which results in less hazardous effect as biomedical implant. Figure 2.18 shows the surface morphology of Fe-based MG and 316L SS before and after immersion in Hank's solution (Y. B. Wang, Li, Zheng, & Li, 2012).

Y.B. Wang et al. studied the performance of three different Fe-based MG in SBF and compared with 316L SS performance. They measured the amount of ion release and the

cell growth on the different substrates. The result showed negligible ion release from the different Fe-based MG compared to 316L SS, Figure 2.19 (Y. B. Wang et al., 2012).

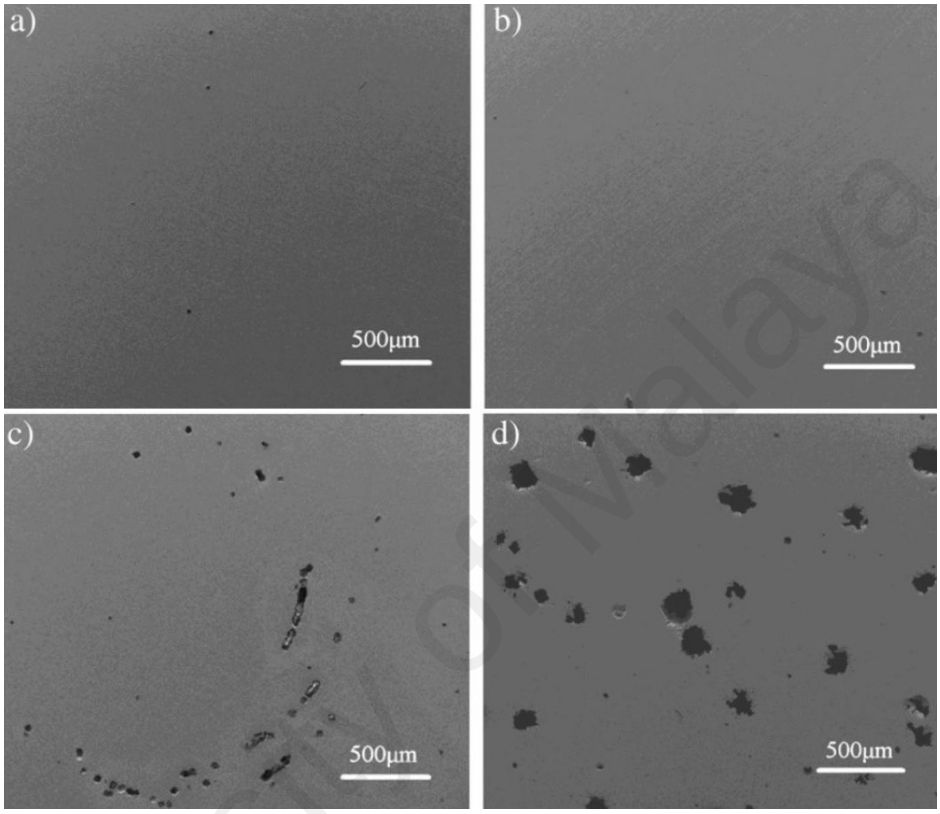

Figure 2.18: Surface morphology of (a) Fe-based MG, (b) 316L SS, (c) Fe-based MG after immersion in Hank's solution, and (d) 316L SS after 15 days immersion in Hank's solution (Y. B. Wang et al., 2012)

The results showed that better biocorrosion and pitting corrosion resistance of Fe-based MG than 316L SS, as well as high cell growth which reveals the biocompatibility potential of Fe-based MG. However, these MGs needs more in vivo and in vitro investigation before introducing to the market.

2.4.1.3. FeCrMoCB MG

FeCrMoCB metallic glass is a newly developed amorphous alloy. Few studies considered investigating the properties of this alloy. Q. Chen et al. studied the electrochemical

corrosion of FeCrMoCB MG in both hydrochloric acid and sodium hydroxide. They concluded that the corrosion resistance of FeCrMoCB MG in acidic environment is better than its resistance in alkaline solution (Q. J. Chen, Hu, Zhou, Hua, & Yang, 2011). Later, Z. Mahbooba et al. utilized direct metal laser sintering and succeeded to produce a fully amorphous structure with a thickness 15 times more than the critical casting (Q. J. Chen et al., 2011). However, no recorded study has investigated the biomedical properties of FeCrMoCB MG as corrosion and wear resistance in simulated body fluids as well as the in-vitro bioactivity and cytocompatibility.

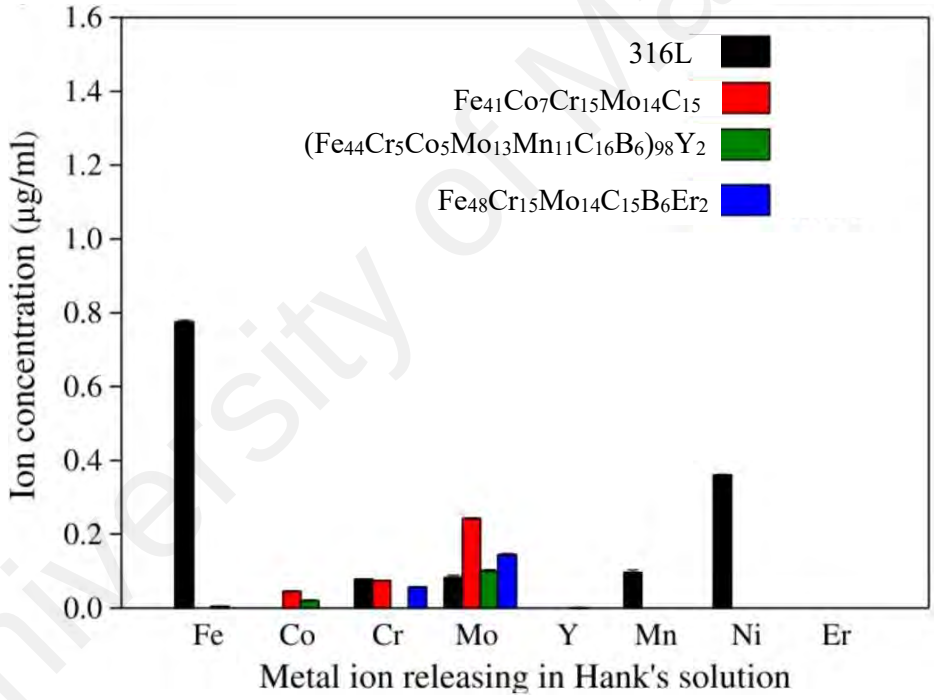

Figure 2.19: Metal ion releasing in Hank's solution for different Fe-based MG and 316L SS (Y. B. Wang et al., 2012)

2.4.2. Ti-based MGs

Titanium and its alloy are of great concern in the recent decades to be utilized in biomedical applications due to their excellent corrosion resistance, biocompatibility, and

mechanical properties. However, enhanced mechanical properties are required. MG systems present better mechanical properties and corrosion resistance behavior. Late in previous century, Ti-based MG was presented with enhanced mechanical and biomedical properties which can be considered a further development of Ti-alloys for permeant implants.

2.4.2.1. Mechanical properties of Ti-based MGs

Many researches were held to evaluate different Ti-based MG alloys. The presented Ti-based MG has relatively low Young's modulus (80-120 GPa), higher tensile strength (1700-2500 MPa), and enhanced corrosion resistance, Table 2.10 (H. F. Li & Zheng, 2016). As mentioned before, fatigue strength is very important factor for biomedical implants. It is reported that Ti-based MGs have promising fatigue strength reaching 1.5 GPa and the ratio of endurance limit to tensile strength is high up to 0.8. This indicates that Ti-based MG may not undergo fatigue phenomena, Figure 2.20 shows the S-N curve of different MG alloys and crystalline alloys (Fujita et al., 2012).

Table 2.10: Mechanical properties of Ti-based MG and Ti6Al4V (H. F. Li & Zheng, 2016)

Material	UTS, MPa	Fatigue Strength, MPa*	Young's Modulus, GPa	Elongation, %	Vickers Hardness, GPa
Ti-based MG	1700-2500	1500	68-102	2.3	4-5
Ti6Al4V	896	250	80	10	0.30-0-39

**The fatigue strength evaluated at 10^7 cycles*

2.4.2.2. Biocompatibility of Ti-based MGs

Many studies investigated the corrosion behavior of Ti-based MGs in different types of SBF, like phosphate-buffered solution (PBS), Hank's solution and Ringer's solution. The studies showed higher corrosion resistance than crystalline Ti-alloys. Ling Bai et al.

investigated in vitro behavior of $Ti_{70}Zr_6Fe_7Si_{17}$ and $Ti_{64}Zr_5Fe_6Si_{17}Mo_6Nb_2$ (at.%) MG alloys. The results showed excellent biocompatibility of both alloys, moreover, the morphology of the specimen revealed forming HA after 15 days of immersion in SBF, Figure 2.21 (Bai, Cui, Wang, Bu, & Qi, 2008).

These results reveal the promising potential of using Ti-based MG in biomedical implants replacing the crystalline Ti-alloys. However, Ti-based MG is limited in size (up to 15mm in diameter) and needs further investigation for both in vitro and in vivo behavior.

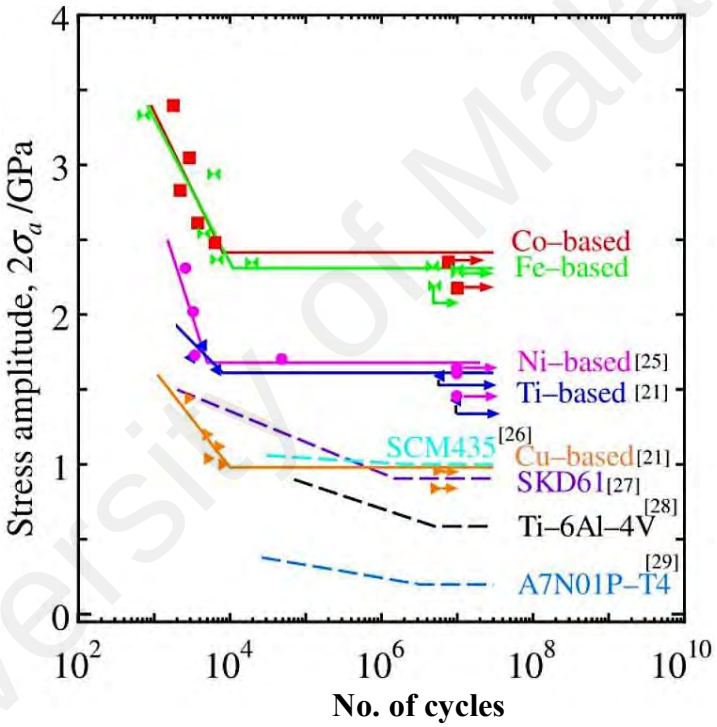

Figure 2.20: S-N curve of different MG systems (Fujita et al., 2012)

2.4.3. Zr-based MGs

The Zr-based MG has high potential since introduced in 1993 by Peker and Johnson (M. Z. Ma et al., 2004) due to their promising mechanical properties and biocompatibility (see Figure 2.12) (Horton & Parsell, 2002). Zr-based MG has high tensile strength, low

Young's modulus, good toughness and good corrosion resistance which in turn become promising in biomedical implants (Horton & Parsell, 2002).

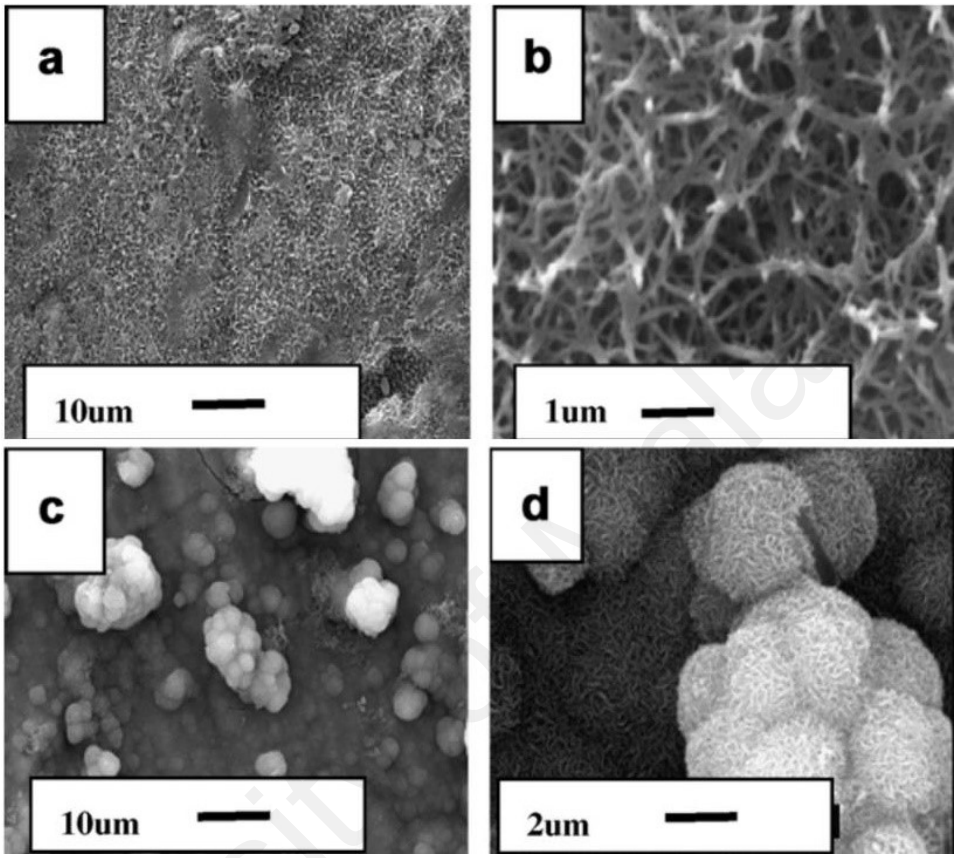

Figure 2.21: SEM image of Ti-based MG showing formation of HA after 15 days cultivation in SBF (Bai et al., 2008)

2.4.3.1. Mechanical Properties of Zr-based MG alloys

Zr-based MG showed relatively high tensile strength (up to 2 GPa), relatively low Young's modulus (about 90 GPa) (Z. Liu, Chan, Liu, & Guo, 2012). In addition, it exhibits good wear resistance, high hardness and high specific strength (Espallargas et al., 2013), but it exhibits lower wear resistance in SBF. This degradation in wear resistance refers to the weak passive layer formed during the wet wear causing progressive wear of the MG (Hua et al., 2015; Yu Wang et al., 2014). It showed to have the same hardness of GCr15 (HRC 60-63), but has higher compressive strength (1900

MPa) and higher fracture toughness (55-59 MPa) (M. Z. Ma et al., 2004), Table 2.11: Mechanical properties of Zr-based MG compared to Ti6Al4V.

Another important property is the fatigue strength. Certain studies revealed that Zr-based MG alloys has fatigue limit which is low as 6-8% of the tensile strength (120-160 MPa) compared to conventional crystalline steel and aluminum alloys (G. Y. Wang et al., 2004). G.Y. Wang et al investigated the fatigue behavior of three different Zr-based MG alloys. The results revealed a comparable fatigue strength of Zr-based MG with high-strength crystalline alloys, Figure 2.22 shows (a) the fatigue behavior and (b) fatigue limits versus tensile strength of different MG and crystalline alloys (G. Y. Wang, Liaw, Yokoyama, Inoue, & Liu, 2008).

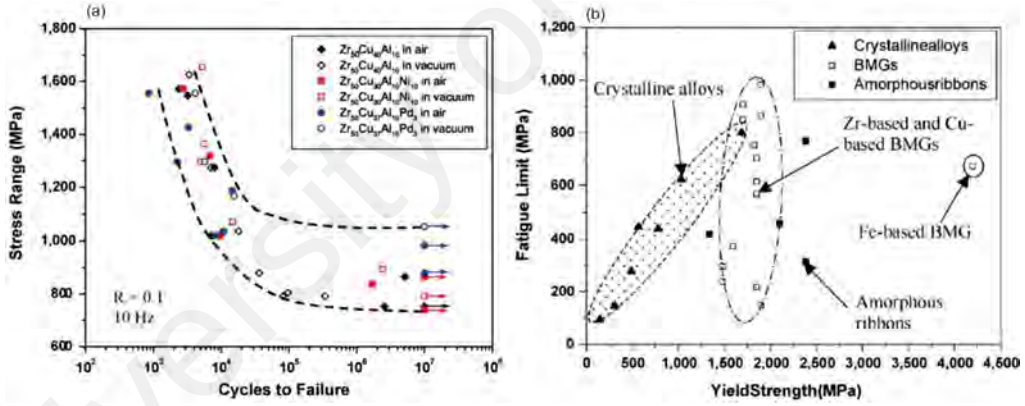

Figure 2.22: (a) Stress-Life curve of three different Zr-based MG alloys in vacuum and in air, (b) Fatigue limit vs yield strength of MG and Crystalline alloys (G. Y. Wang et al., 2008)

Table 2.11: Mechanical properties of Zr-based MG compared to Ti6Al4V

Material	UTS, MPa	Fatigue Strength, MPa*	Young's Modulus, GPa	Hardness, HRC
Zr-based MG	2000	550	90	55-59
Ti6Al4V	896	250	80	30-39

**Fatigue evaluated at 10^7 cycles*

2.4.3.2. Biocompatibility of Zr-based MG

One of the key properties for biocompatible materials is the corrosion resistance. Many studies investigated the corrosion resistance of Zr-based MG in various physiological solutions. The results showed enhanced corrosion resistance than conventional crystalline alloys - like stainless steel, Co- alloys and Ti-alloys (H. F. Li & Zheng, 2016). This because of the passive film formed which is composed of ZrO_2. It was revealed that the addition of Yttria 1% wt. enhanced the biocorrosion resistance of Zr-based MG alloy (L. Huang et al., 2009).

Other studies investigated the biocompatibility of Zr-based MG both in vitro and in vivo. The findings showed superior biocompatibility of Zr-based MG over crystalline stainless steel, Zr-alloys and Ti-alloys (H. F. Li & Zheng, 2016). Yu Sun et al investigated the in vitro and in vivo biocompatibility of Ag-bearing Zr-based MG and compared with pure Ti and Ti6Al4V. Figure 2.23 shows the developed pits on the surface of the specimen. It is cleared that pure Ti and Ti6Al4V alloy exhibited larger pits than that in Zr-based MG (Sun et al., 2015).

Generally, Zr-based MG alloys are promising materials for biomedical applications because of their excellent mechanical and biocompatibility properties. However, Zr-based MG alloys products are limited in size, as well as, they are very brittle in tension and show less plasticity in compression (Gludovatz et al., 2013). Although the fracture strain can be improved from 2% to 5.5% regarding to the existence of crystalline phase within the amorphous matrix, it is still need more investigation (Ye, Bae, Shin, & Stanciu, 2015). In addition, the production processes are expensive as it requires high purity elements and expensive consumables.

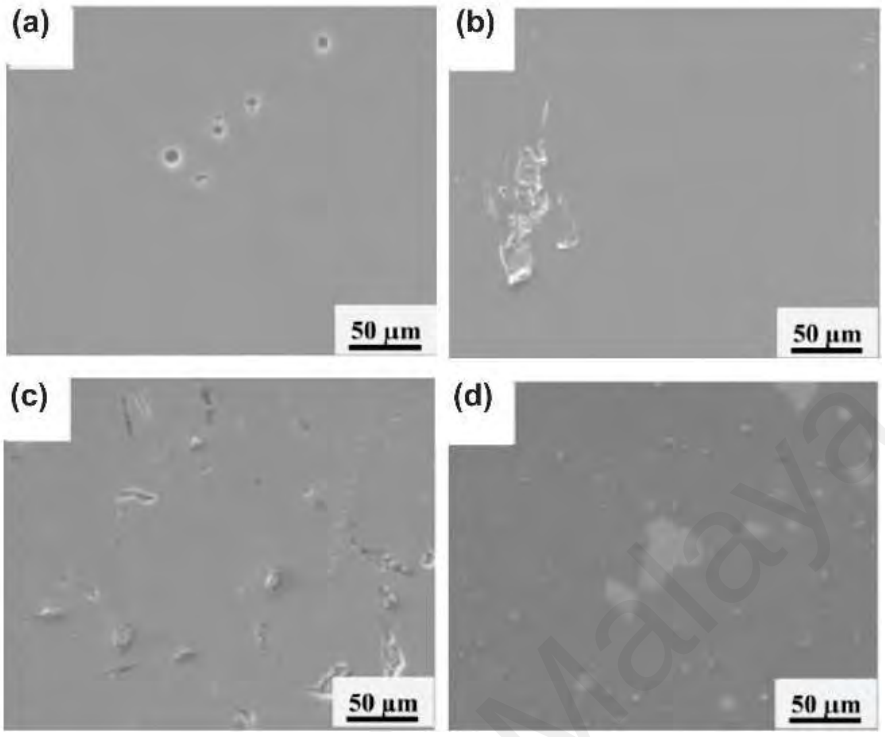

Figure 2.23: SEM image of (a) Zr51.9Cu23.3Ni10.5Al14.3, (b) Zr51Ti5Ni10Cu25Al9, (c) pure Ti, (d) Ti6Al4V after 15 day of immersion in Hank's solution at 37 ^{o}C (Sun et al., 2015)

2.5. Techniques to improve the performance of biomedical implants

Numerous researches focused on improving the performance and durability (nowadays an average 10-15 years lifetime) of biomedical implants (Espallargas et al., 2013). In case of metals, the poor bioactivity, and the release of toxic ions in the human body are the main challenges facing metallic implants. The poor bioactivity result in poor fixation of implant with the bones which may need revision surgery. Also, the rapid bio-corrosion of metals cause release of toxic elements that has severe adverse effect on the health (Rahmati, Sarhan, et al., 2015; Rautray, Narayanan, & Kim, 2011). To overcome this problem, surface treatment techniques are used to improve the chemical, mechanical and biological properties of the surface interfaced with the living tissues. The surface treatment is of two main categories:

1. altering the chemical and microstructure of the surface
2. applying coating material on the surface.

The first category includes techniques to modify the chemical composition of the surface – as carbonization of steels – or modify the surface microstructure or applying both. These modifications affect the wettability, surface charge, and hydrophobicity. These properties showed a significant effect on organic adsorption into the implant surface. Generally, increasing the hydrophobicity of the surface results in better biocompatibility (Thevenot, Hu, & Tang, 2008).

S. Muley et al. evaluated the biological performance of 316L stainless steel by developing ultra-fine grains at the surface. By decreasing the grain size – form 30μm to 0.86μm – the hardness was almost doubled (from 172 VHN to 300 VHN), the wear and pitting corrosion resistance increased, and improved localized corrosion resistance (Muley et al., 2016). X. Zhao et al. introduced surface nanotopographic with chemical modification. The author developed nanotopographic layer of TiO_2 doped with Nb_2O_3 on CP-Ti. They realized enhancement in corrosion resistance, bonding strength and biocompatibility (Zhao et al., 2014).

The second category is coating techniques. Coating techniques have become promising due to the combination of the superior properties of both substrate – such as high strength, fracture toughness and fatigue – and coating materials – such as improved wear and corrosion resistance. For example, a bioactive coating enhances the implant fixation and results in reduced mechanical failure (for fully HA coated implants the mechanical failure ranges from 1% to 6.9% which is much lower than cement type fixation) (Sanli, Arts, & Geurts, 2016), prevent further ion-release form the metallic substrate, and prevent formation of fibrous tissue which may result from micro-movements of uncoated implant. Also, development of MG coating on metallic substrate would enhance the tribology, corrosion, biocompatibility properties, besides the excellent mechanical properties of

substrate. Wide range of coating techniques introduced, but till now an optimal technique has not been introduced yet (Campbell, 2003). The researchers presented vast coating techniques as

- physical vapor deposition (PVD),
- plasma spray,
- laser cladding,
- and solution-based methods as sol-gel and electrochemical deposition.

However, plasma spraying still the only approved method by US-FDA for applying bioactive coatings in biomedical application (Mohseni, Zalnezhad, & Bushroa, 2014).

A high quality coating for biomedical applications should exhibit sufficient adhesion strength (50 MPa approved by US-FDA) (Mohseni et al., 2014), high hardness of final coat, excellent osseointegration and osseoconduction properties, reduced cracks among the coating, and free of inclusions. Recently, the research work is directed towards developing thin and uniform coatings to reduce the fragments and debris produced (Goodman, Yao, Keeney, & Yang, 2013). Next, we will focus on the coating techniques used to enhance the performance of biomedical implants.

2.5.1. Physical Vapor Deposition (PVD)

PVD techniques are based on vaporizing materials from the source material – called target – to be deposited on the substrate. PVD is divided into three categories; vacuum, ion spraying and magnetron sputtering (Suetsugu & Tateishi, 2014). A vacuumed chamber incubates charged substrate and target with positive and negative charge, respectively using DC-power supply. Then the process utilizes gas plasma (argon, neon) which is ionized by means of electric charges. The sputtered ions hit the target causing evaporation, and free-atoms are ejected from the surface which is deposited on the substrate. Usually, magnets are used to accelerate the formation of coatings (Suetsugu &

Tateishi, 2014). Figure 2.24 shows PVD magnetron-sputtering setup layout. It was recognized that the substrate temperature affects the quality of produced coating (Rahmati, Sarhan, et al., 2015).

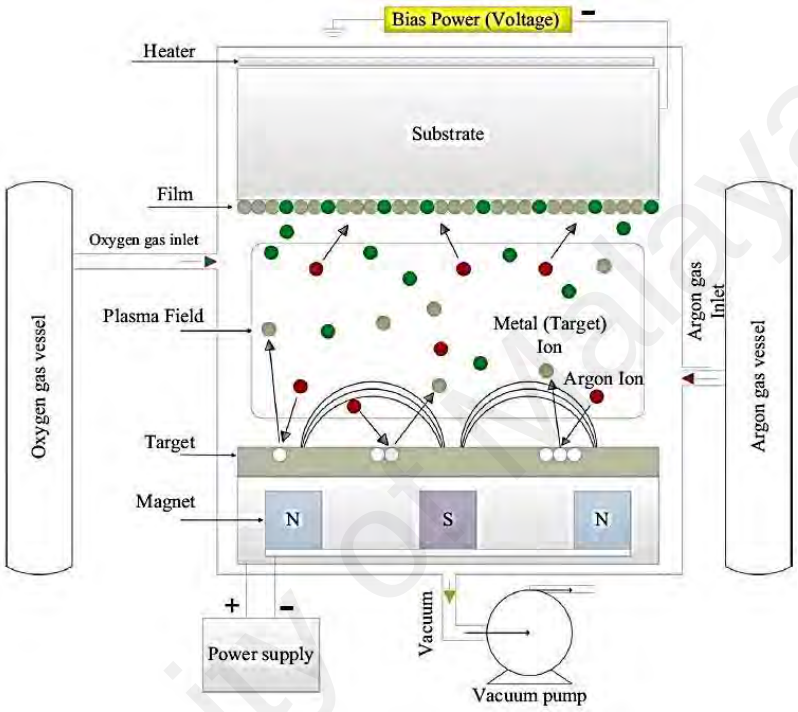

Figure 2.24: PVD magnetron-sputtering setup (Rahmati, Sarhan, et al., 2015)

Numerous researches utilized PVD to coat Ti-alloy with bioceramics to enhance the biocompatibility. PVD is featured as versatile technique, developing high purity and dense coatings, Figure 2.25 show dense Ta_2O_5 coating developed by PVD. Also, it exhibits excellent adhesion strength with the substrate, and can deposit any material (metal, alloy, or compound) on the desired substrate (Baradaran et al., 2013). Another important advantage that PVD operates at relatively low temperatures which leads to lower degradation of the coating and substrate (Kasuga, 2010). B. Rahmati et al. investigated the post heat treatment to enhance the adhesion strength of previously developed Tantalum oxide coating on Ti6Al4V using PVD magnetron-sputtering

technique. They concluded that higher treatment temperature (500 °C) enhance the adhesion strength because of better penetration of Tantalum oxide into the substrate (Rahmati, Zalnezhad, et al., 2015).

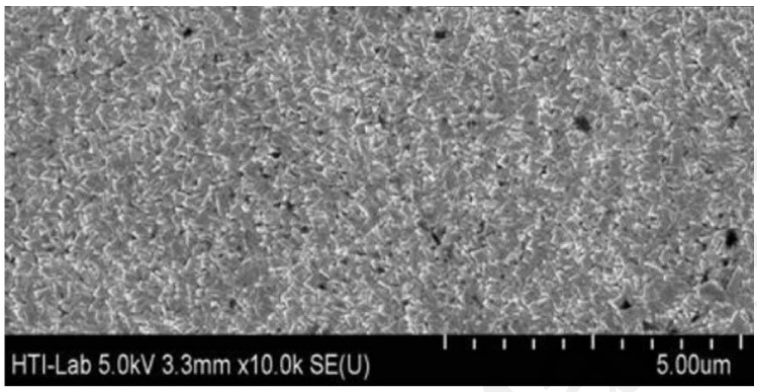

Figure 2.25: TaO coating layer developed on Ti6Al4V developed by PVD (Rahmati, Zalnezhad, et al., 2015)

WU Zhen-Jun et al. presented biocomposite coating (HA/Al_2O_3) on CP-Ti. The authors employed PVD to deposit Al on Ti, followed by anodization process to develop Al_2O_3, and finally using electrodeposition to deposit HA coating. The results revealed that enhanced adhesion strength obtained (21.3 MPa), and improved biocompatibility (Wu, He, & Chen, 2006). Jeong et al. prepared HA coating on nanotubular TiTaHf alloy using PVD, Figure 2.26 shows the morphology of nanotubular array developed. The authors presented great potential for HA deposited on nanotubular surface as it will induce better bioactivity and cell adhesion. This may result from the nano-features of the coating on the surface, Figure 2.27 shows the nano-feature of HA layer in favor of nanotubular array previously developed on the surface (Jeong, Moon, Choe, & Brantley, 2013). E. Mohseni et al. utilized PVD technique to develop multilayer coating (Ti/TiN/HA) on Ti6Al4V. They studied the process parameters on the adhesion strength, coefficient of friction, and surface roughness. The results showed enhanced adhesion strength by 44.57% and surface roughness by 10.52% (Mohseni et al., 2015).

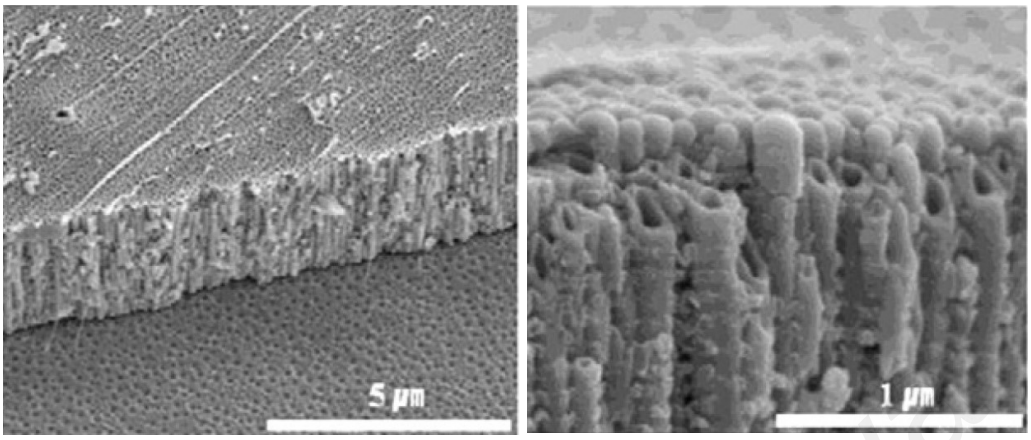

Figure 2.26: Nanotubular array on TiTaHf alloy (Jeong et al., 2013)

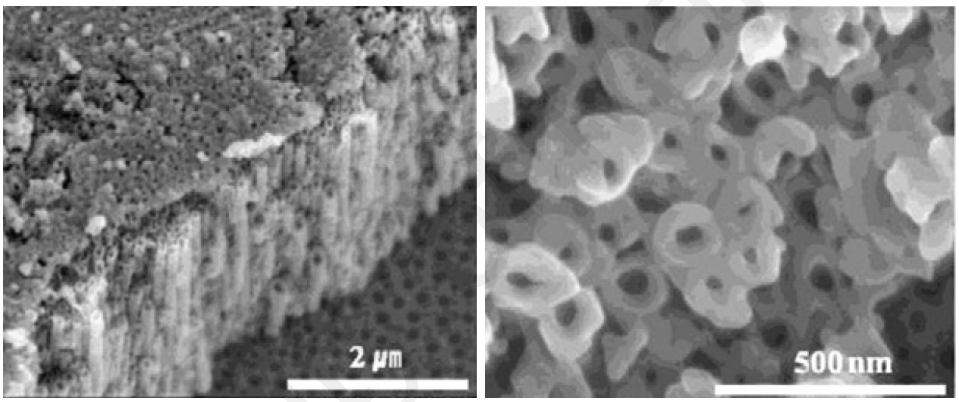

Figure 2.27: HA coating on nanotubular TiTaHf alloy (Jeong et al., 2013)

PVD is successful to develop bioactive coatings on metallic substrate. Although PVD produces high dense, high purity and excellent adhesion strength, PVD technique exhibits disadvantages as expensive and time consuming process, and insufficient bonding strength between the substrate and the coating layer (Mohseni et al., 2014).

2.5.2. Sol-gel technique

The sol-gel technique is based on mixing different organic precursors – including the coating precursor – in aqueous medium to prepare the "sol", then the mixture is polycondensated to form "gel" which can be further used for coating. The gel is deposited

on the substrate and subjected to sintering to form the final coating layer (Omar, Ballarre, & Ceré, 2016). The sintering temperature is considerably low temperature (about 500 °C) (Mohseni et al., 2014).

Sol-gel technique is a simple technique which able to coat complex geometry because of the gel state, produce high purity and homogeneity coating, and provide excellent adhesion, as well as, good corrosion resistance coating (Olding, Sayer, & Barrow, 2001).

Hydroxyapatite is sensitive to the high temperature and may decomposes, so sol-gel technique is considered suitable for processing and depositing HA as the sintering temperature is relatively low. Number of research works employed sol-gel technique for coating Ti-substrate with thin layer of HA (He et al., 2014) or functional graded material (FGM) to improve the biocompatibility (Gross, Chai, Kannangara, Ben-Nissan, & Hanley, 1998).

A. Stoch et al. deposited HA on Ti6Al4V using sol-gel technique. The authors added animal gelatin to the sol to enhance the formation of amorphous phase of HA and studied the pH effect of sol on the final coating. The result showed the most favorable pH was 6.5-7.8 and the gelatin improved the stability of sol. The developed HA coatings showed excellent in-vitro bioactivity which reflects the success of the proposed technique, Figure 2.28 shows the resulted morphology after immersion in PBS for 19 days (Stoch et al., 2005).

P. Choudhury et al. proposed pure HA and composite HA and ZrO_2 coatings on Ti by sol-gel. They concluded that pre-passivation of Ti substrate increase the roughness which in turn enhance the bonding strength of the coating. In addition, the composite coating of HA and ZrO_2 exhibited higher bonding strength (Choudhury & Agrawal, 2011).

Few researches focused on coating SS alloys with HA using sol-gel technique. Dean-Mo Liu et al. investigated different sintering temperature levels effect on the coating

properties of SS. The results showed that at temperature greater than 400 ^{o}C produce better crystallinity, higher bonding strength (up to 44 MPa), and micro-pores, Figure 2.29. However, the developed coating exhibited surface micro-cracks and non-uniform thickness (D.-M. Liu, Yang, & Troczynski, 2002).

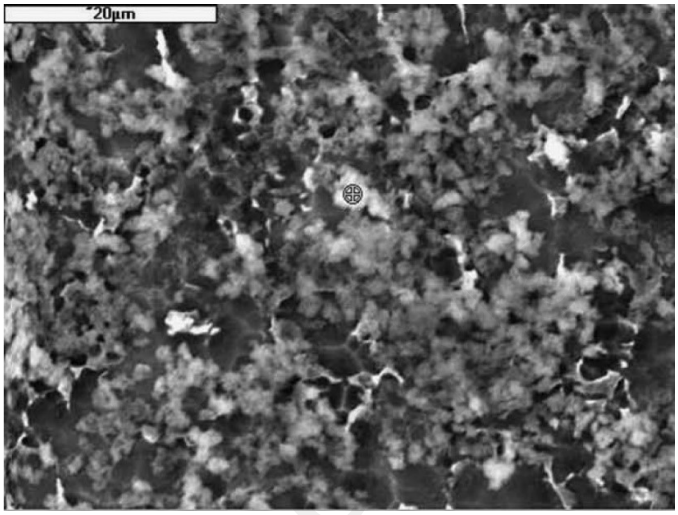

Figure 2.28: SEM morphology of sol-gel HA coating after immersion in PBS for 19 days (Stoch et al., 2005)

There are few researches considered Bioglass coatings using sol-gel techniques. S. Pourhashem and A. Afshar prepared 45S5 Bioglass coating on 316L SS by sol-gel technique. The obtained coatings were crack-free, Figure 2.30, have good crystalline structure and exhibited improved corrosion resistance. The results showed bioactivity behavior and HA formation was realized on the surface (Pourhashem & Afshar, 2014).

The sol-gel technique is featured as simple coating technique. Also, it is suitable for complex shapes as the gel-nature can fill gaps, exhibits relatively low sintering temperature, and produce thin layers of coating. In the other hand, sol-gel has limitations as cracking, low wear resistance, and high permeability. The sol-gel technique is sensitive to the substrate material as the difference in thermal properties between the coating and

the substrate which cause delamination of coating and hence, process failure (Olding et al., 2001). Hence, further research is needed to overcome major drawbacks as poor adhesion strength, and cracking.

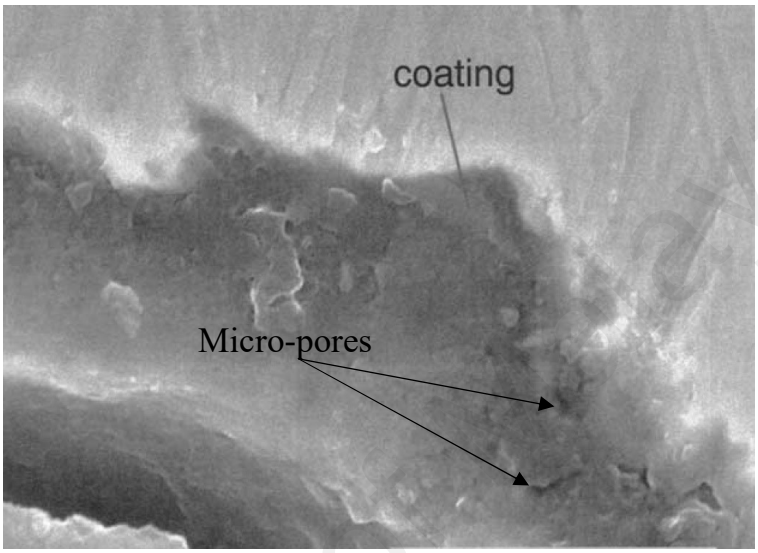

Figure 2.29: Micro pores at the surface of HA layer (D.-M. Liu et al., 2002)

2.5.3. Plasma spraying

Plasma spraying is the most common method deployed for coating metallic substrates with bioceramics and the only approved – by US FDA – technique for biomedical application. Also, many researchers utilized plasma spray for developing MG coating layer (An et al., 2014; D. Li et al., 2017). The process involves melting material powder using high temperature plasma gas (up to 15000 °C). The molten powder is sprayed over the surface and the coating is developed. Figure 2.31 shows the principle of plasma spraying technique (Mohseni et al., 2014).

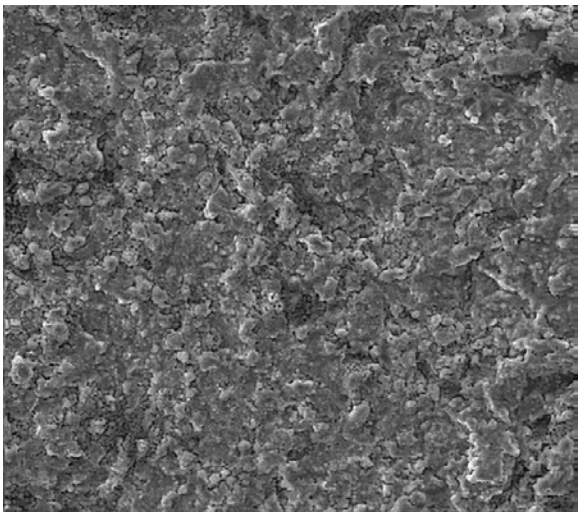

Figure 2.30: SEM of Bioglass coating on 316L SS (Pourhashem & Afshar, 2014)

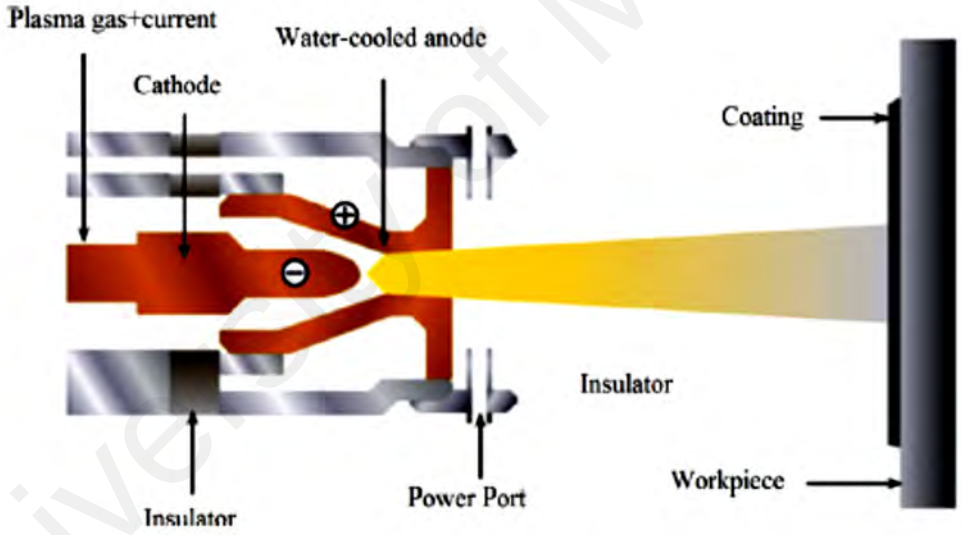

Figure 2.31: Schematic of plasma spray setup (Mohseni et al., 2014)

Plasma spraying is a low-cost technique and has rapid deposition rate as well as reduced thermal degradation compared to other thermal techniques. However, plasma spraying still lacks to offer high adhesion strength, induce cracks (Tlotleng, Akinlabi, Shukla, & Pityana, 2014) and may cause microstructure changes in the developed coating (Mohseni et al., 2014).

Recently, many researchers focused on coating metallic substrate with HA using Plasma spraying technique as it is approved by FDA. Kulpetchdara et al. employed plasma thermal spraying in coating SS substrate with nanostructured HA for hip joint implant. The authors used commercial and synthesized nano-sized HA and compared the resulting microstructure (Figure 2.32), hardness and bioactivity. The nanostructured HA exhibits higher hardness (VHN 2.15 GPa compared to VHN 1.06 GPa for commercial HA), higher degree of crystallinity, and excellent osseoconduction which can replace the conventional HA in prosthetic applications (Kulpetchdara, Limpichaipanit, Rujijanagul, Randorn, & Chokethawai, 2016).

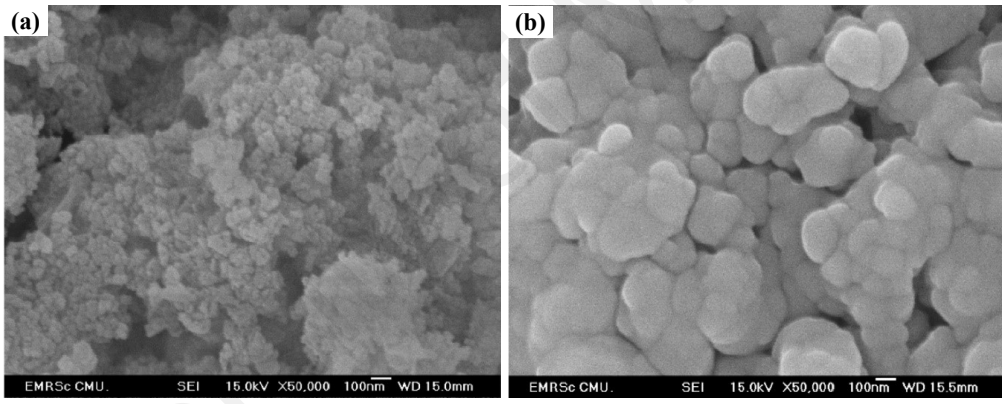

Figure 2.32: SEM of plasma sprayed (a) commercial HA coating, (b) synthesized nano-sized HA coating (Kulpetchdara et al., 2016)

The bonding strength of plasma sprayed HA coating with Ti6Al4V is a weak point. M.J. Filiaggi et al. proposed post heat treatment of plasma sprayed HA coatings. The results showed dramatically increase in mechanical properties – bonding strength up to 40 MPa and fracture toughness reaching 3 MPa.$m^{1/2}$. However, the chemical composition of the coating was changed which affected the bioactivity of HA coating (Filiaggi, Pilliar, & Coombs, 1993).

Manoj Mittal et al. investigated the corrosion behavior of HA coated 316L SS and Ti and compared the results with the uncoated ones. The authors used plasma spray to deposit HA on SS and Ti substrate. The results showed that a certain decomposition of HA took place, as well as micro-cracks on the surface, and porosities, Figure 2.33 shows the induced micro-cracks and porosities in HA coating on SS and Ti. The electrochemical test showed enhanced corrosion resistance of coated samples. In addition, the HA coated Ti showed better results than HA coated 316L SS which reveal the effect of the substrate material (Mittal, Nath, & Prakash, 2011). Y. Wang et al. studied HA coatings on Ti using micro-plasma spraying. The results showed improved crystallography and higher crystallinity than atmospheric plasma spraying. The in-vitro tests showed higher HA stability in Hank's solution for 14 day (Yiming Wang et al., 2017). V. Shamray et al. proposed preheated substrate to promote the HA coating using plasma spray. The authors noticed that the composition and structure of the final coating has been affected. The surface of coating appears to have flattened splats which is formed from molten particles as shown in Figure 2.34 (Shamray et al., 2017).

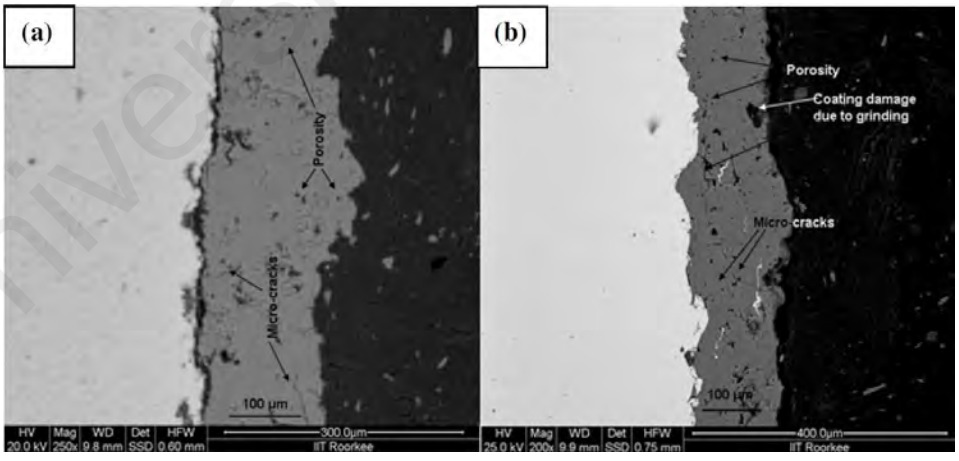

Figure 2.33: Micro-cracks and porosities included in HA coating on (a) 316L SS, (b) Ti (Mittal et al., 2011)

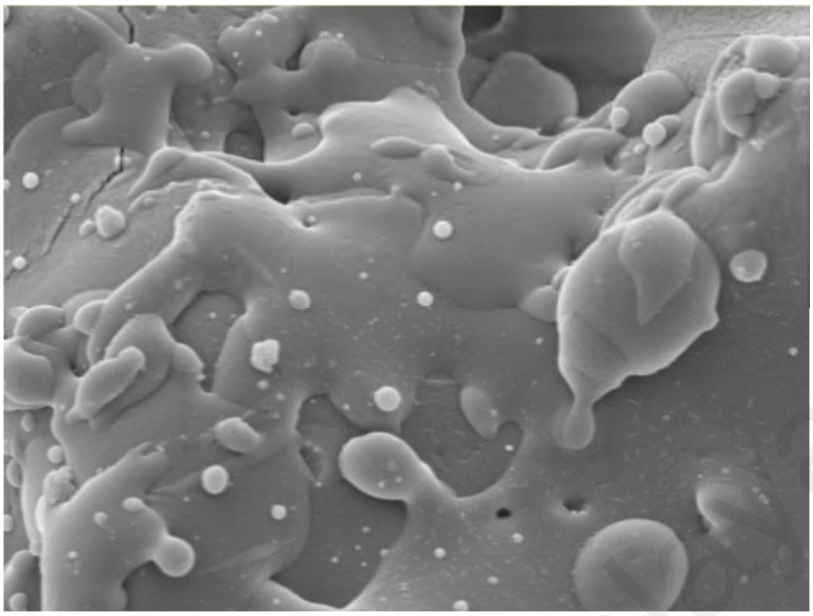

Figure 2.34: SEM of HA coating on preheated Ti to 300 ^{o}C (Shamray et al., 2017)

2.5.4. Laser cladding technology (LCT)

Laser is a promising technique applied in various applications. Recently, laser was successfully employed in welding dissimilar materials (Ezazi et al., 2015), surface melting and treatment (Alavi & Harimkar, 2015), metal additive manufacturing (Frazier, 2014) and prototyping (Pinkerton, 2016), and coating processes (Xu, Li, Jiang, & Li, 2015). Laser techniques found wide applications in different industries; aerospace, marine, oil and gas, and biomedical applications.

Laser cladding technique was developed to deposit coating material on substrate using laser energy. The coating material is usually in powder form which may be preplaced (Barekat, Shoja Razavi, & Ghasemi, 2016) over the substrate surface or injected under pressure (Shu et al., 2016) or gravity (Wai Yip, Barnes, & Aly Diaa Mohmmed Sarhan, 2015). Laser beam melts the powder – the process involves rapid heating and cooling – and creates melt pool without melting the substrate. As the laser scans the surface, the

pool solidifies building a firm and dense coating on the surface. Figure 2.35 illustrates methods used in laser cladding.

Laser cladding (LCT) is a promising technique because it produces full-dense coatings with outstanding properties (Herzog, Seyda, Wycisk, & Emmelmann, 2016), forms strong metallurgical bond between substrate and coating (Zeng, Tian, Liao, & Hua, 2016), able to deposit ceramics or metals on metallic substrate (Sola, Bellucci, & Cannillo, 2016), and leads to reduced heat affected zone (HAZ), Figure 2.36 shows different zone induced at cladding area (Quazi et al., 2016). Also, it provides controlled shape of the coating, flexible process, controlled degree of dilution, low surface roughness with high deposition rate, and requires minimum surface preparations (Comesaña et al., 2010).

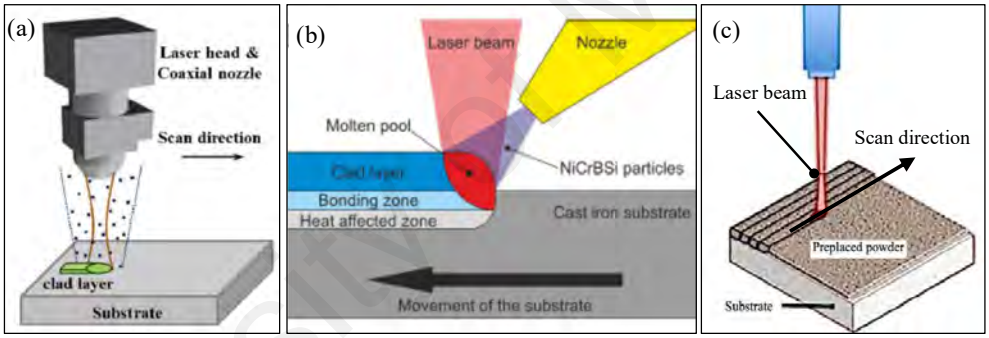

Figure 2.35: Laser cladding process using (a) by gravity (H. Liu et al., 2016), (b) injected powder (Arias-González et al., 2016), (c) preplaced powder (Quazi et al., 2016)

LCT offers metallurgical bonding between coating and substrate, as well as, excellent full-dense coating layer. Different works investigated coating Ti-alloys and SS – as the most common alloys used in implants – with different bioceramics and metallic glasses to enhance the corrosion resistance, besides the bioactivity behavior.

Many studies were held to improve the microstructure of the coating and the bonding strength. These improvements were attained, for example, by developing functionally graded carbon nano-tubes (CNT) with HA composite coating. The coating consisted of

three layers: bottom layer (5% CNT), intermediate layer (3% CNT), and top layer (pure HA), Figure 2.37 shows the coating layers and it is noted no existence of separation between layers. X. Pei et al. found that CNT increased the crystallinity of HA coating and bonding strength from 14.6 to 29 MPa, besides the excellent bioactivity as shown in Figure 2.38 (Pei et al., 2011).

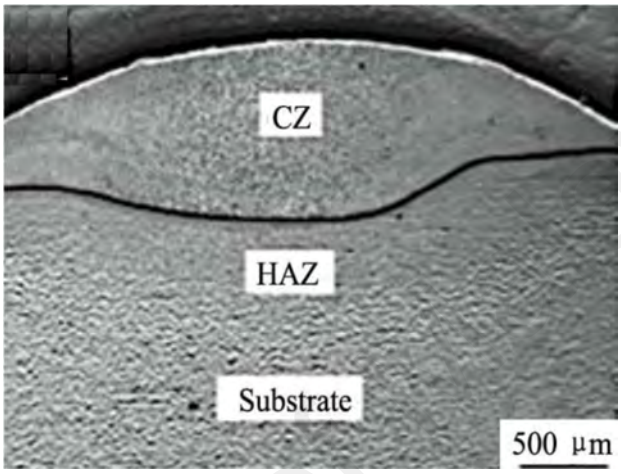

Figure 2.36: Cross-section of single laser cladded track showing substrate, HAZ, and cladded track (Quazi et al., 2016)

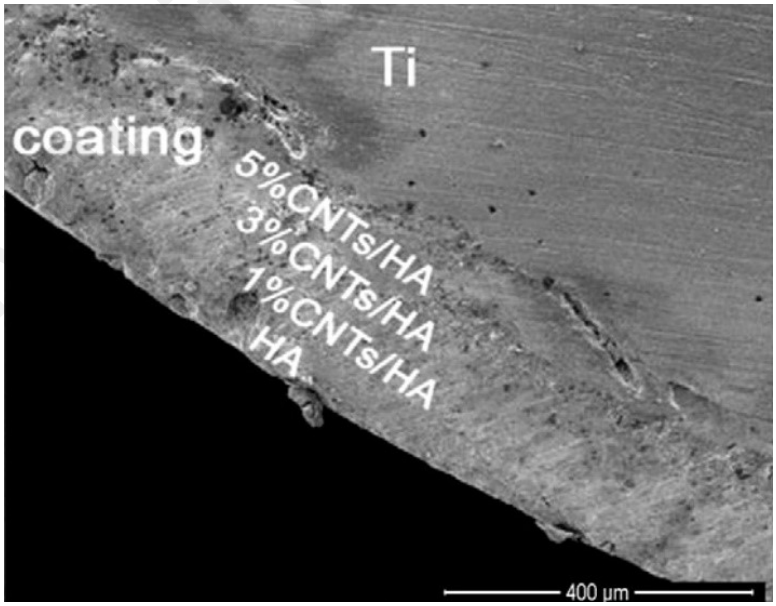

Figure 2.37: Coated Ti with FG CNT/HA composite (Pei et al., 2011)

Not many studies focused on coating SS with bioactive materials using laser cladding technique. Q. Wei studied the selective laser melting of SS/nHA composite implant to offer uniform metallurgical bonding of metal and ceramics. The nano-HA powder showed better bioactivity performance (FAN et al., 2009). They reported that increasing the laser scanning speed decreases the degree of cracks (Wei et al., 2015). Fathi et al. investigated the coating of 316L SS with pure HA, pure Ti, and double-layer coating of Ti and HA. The double-layer showed positive improvement in corrosion resistance behavior compared to the other specimen (Fathi, Salehi, Saatchi, Mortazavi, & Moosavi, 2003). M. R. Mansur et al. proposed composite coating of HA and TI6Al4V on SS. The study revealed that Ti diffused into the substrate in the heat affected zone. At the top layer, Ca/P ratio was 1.66 which is near to the human bone composition (Mansur et al., 2013).

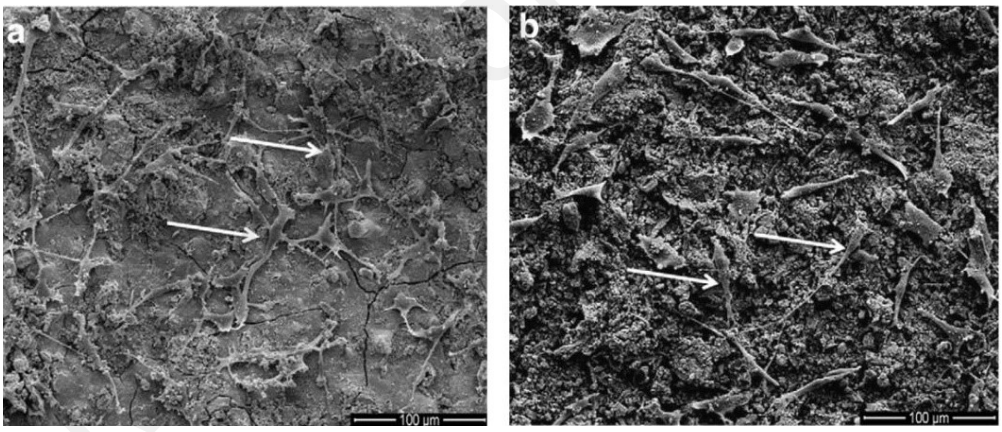

Figure 2.38: SEM image of (a) pure HA, (b) FG CNT/HA composite after 7 days of cell-culture (Pei et al., 2011)

Functionally graded materials (FMGs) approach was proposed because the HA coating deteriorates during working period due to poor interface bonding. This method reduces the dilution rate of HA and reduces the cracking possibilities. M. A. Hussain proposed a hybrid mixture of HA, 316L SS and CNT to build FGMs, Figure 2.39 shows SEM morphology of the resulting coating layer. The HA powder was 50% micro-sized and

50% nano-sized to increase the density of the HA. The proposed coatings showed increased hardness and enhanced mechanical properties (Hussain et al., 2014).

On the other hand, laser cladding was applied to develop MG coating on metallic substrate. Due to the close matching of chemical composition and physical properties between, the MG and metallic alloys, the laser cladding technique succeeded to produce a defect-free coating layer. In addition, the rapid heating and cooling induced during the laser cladding process helped the control of the microstructure and the amorphicity of the MG (Balla & Bandyopadhyay, 2010; Ibrahim et al., 2018; Lu et al., 2018; Y. Zhang et al., 2015).

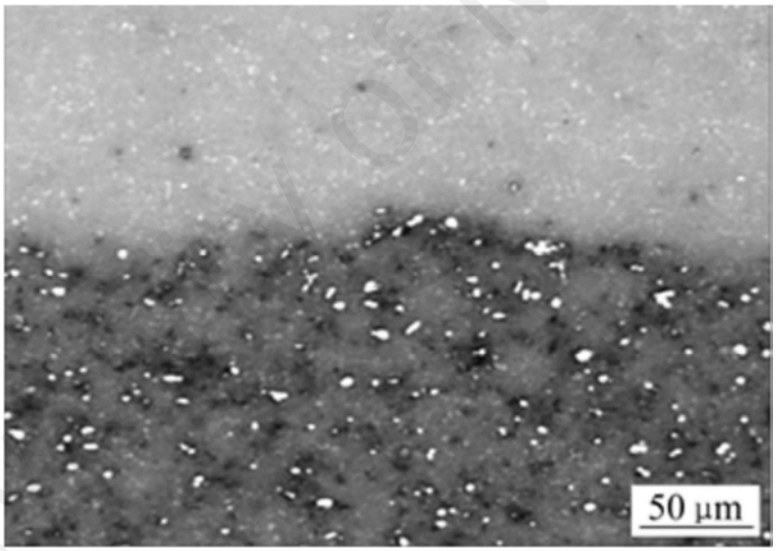

Figure 2.39: HA/316L SS composite coating layer (white particles are 316L SS and grey color is HA) (Hussain et al., 2014)

Generally, laser cladding technique is a promising technique to develop bioceramics or MG coating layer on metallic substrate with high bonding strength, controlled microstructure and less cracks and defects. Besides, the LCT is cost-effective compared to other present coating technique (Leyens & Beyer, 2015).

2.6. Conclusion

There is a wide variety of metallic biomaterials introduced; Ti, Co and SS alloys are the most popular alloys used in biomedical implants due to their excellent mechanical prperties. Nickel-free SS is another candidate with acceptable mechanical and biocompatibility properties.

Recently, the researchers considered the MG alloys in biomedical applications because of their superior wear, corrosion and biocompatibility especially, Fe, Zr and Ti-based MG. However, the lack in fatigue properties and limitations to fabricate in large sizes are the main challenges for application of MG in bone-implants.

The metallic alloys failed to show bioactivity properties and to sustain their mechanical properties in corrosive media, which result in reduced durability. In addition, the studies reported hazardous ion release from some metallic alloys when implanted in human body. In the other side, MG proved superior mechanical properties, corrosion resistance and biocompatibility properties. These studies reported the excellent tribology behavior.

Many techniques have been developed to coat metallic substrate with MG materials to promote the surface properties of metallic alloys, besides preventing further ion release of hazardous elements. The techniques covered in this review are plasma spraying, sol-gel coating, PVD, and laser cladding.

Currently, only plasma sprayed HA coating is approved by FDA and further researches are needed to improve the properties of resulted coatings by different techniques which may offer better adhesion or higher stability. The research trend is to present improved performance and durability of biomedical implants as the current technique still lack to meet these objectives.

2.7. Research gap

Recently, many research works focused on developing materials for bone-implants with longer life-span (more than 25 years). More studies and investigations should consider new developed alloys as Ni-free SS and new Ti-alloys as TiAlNb which offer lower ion release and less hazardous effect. Also, more studies and investigations are needed to improve the toxicity and biocompatibility of Co-alloys.

The current implants life is 15-20 years, and the objective is to reach 40 years to minimize the revision surgeries. However, the current coating techniques are still lack meeting higher life-span because of the lack in sufficient adhesion strength. The improvement in adhesion strength will enhance the durability and will overcome the problems of coating separation and lamination during implanting process.

A new trend is to develop coatings from MG on conventional used metallic bone-implants to enhance the wear and corrosion resistance with acceptable biocompatibility.

CHAPTER 3: METHODOLOGY

3.1. Introduction

This chapter deals with the materials, equipment, methods and tests used in this research. First section is describing materials used in this research. Next, the methods and techniques used for preparing and fabricating the samples, as well as, the description of the experimental steps and arrays. The last section is describing all the tests, characterizations and examinations, besides the equipment and devices that have been utilized in this research. Figure 3.1 shows the flowchart of the research methodology.

3.2. Materials

3.2.1. Substrate material

Based on the literature review, a nickel-free high nitrogen SS (ASTM F2229) commercially known as Cronidur30 was selected as a substrate material. This alloy showed better mechanical properties than conventionally used 316L SS. A 400x65 mm and 3-mm thickness strips supplied by Energietecknic GmbH, Germany – the elemental composition shown in Table 3.1 and the mechanical properties in Table 3.2 – were cut using wire-EDM into 30x30 mm coupons.

Table 3.1: Elemental composition of Cronidur30 as provided by the supplier

Element	Fe	Cr	Ni	Mo	Mn	Si	N	C
ASTM F2229	balance	16.00	0.50	1.10	1.00	1.00	0.50	0.35

** All values are in wt.%*

The microstructure of the as received material is shown in Figure 3.2. The optical microscope reveals a fine microstructure of Corindur30. The small particles appeared represent the carbonitride phases. Three sharp peaks were recognized in the X-ray diffraction (XRD) pattern showing a typical crystalline structure of SS, Figure 3.3.

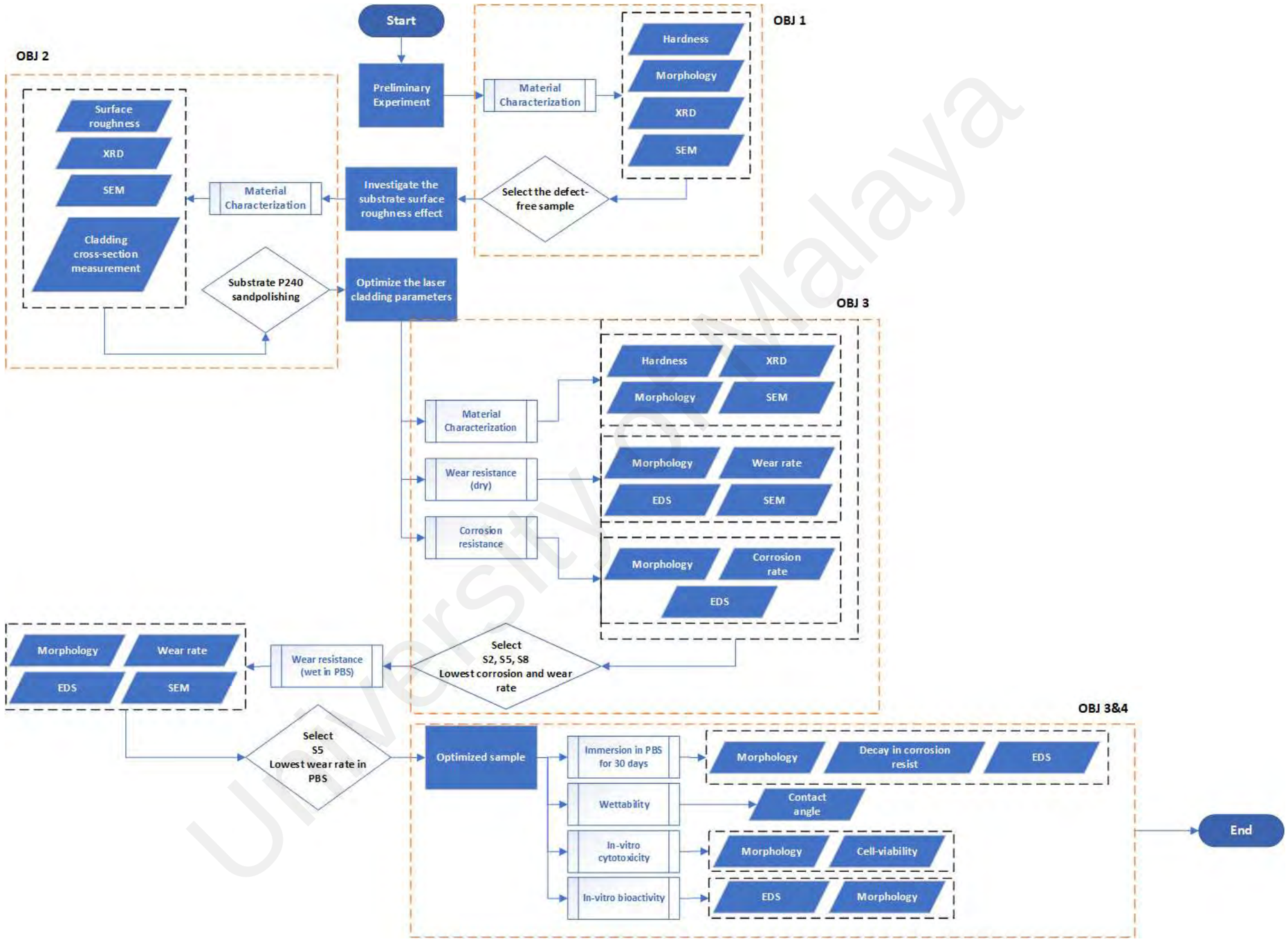

Figure 3.1: flowchart of the research methodology

Table 3.2: Mechanical properties of Cronidur30 as given by the supplier

Hardness (HRc)	Yield strength (MPa)	Tensile strength (MPa)	Fracture elongation (%)	Fracture toughness ($MPa.m^{1/2}$)
> 58	1850	2150	3	> 20

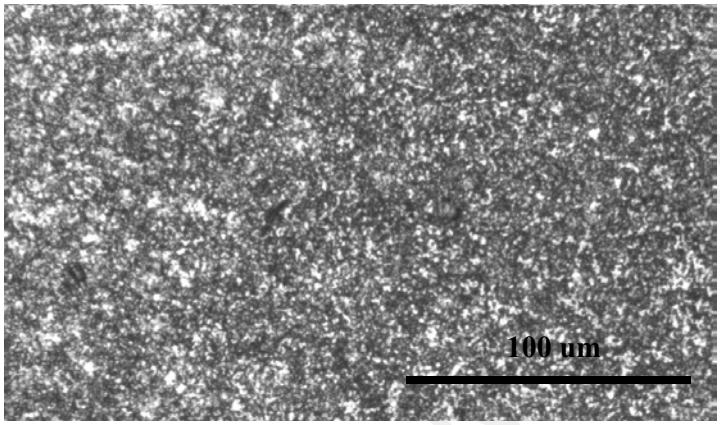

Figure 3.2: Optical microscope image of the microstructure of Cronidur30

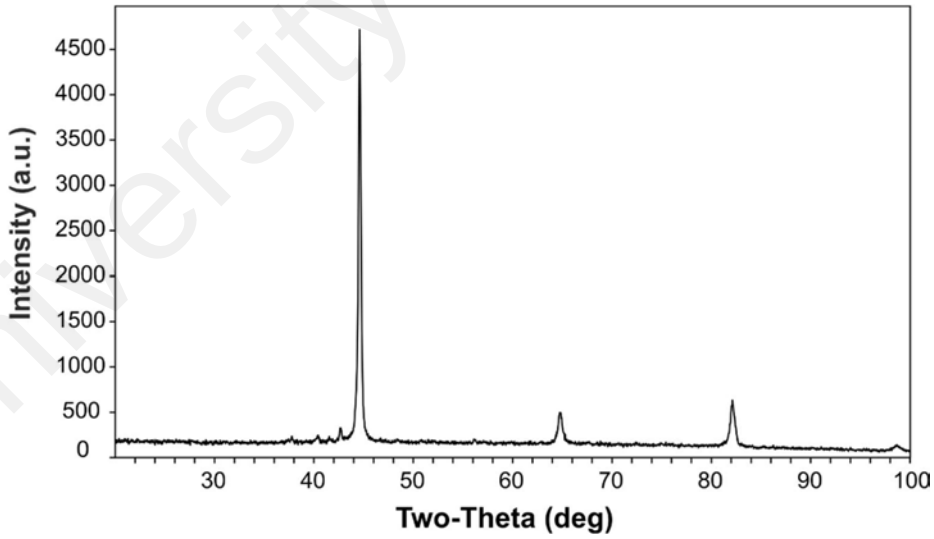

Figure 3.3: XRD pattern of Cronidur30

3.2.2. Coating material

Fe-based amorphous powder – noted as FeCrMoCB – with nominal particle size 20 to 70 μm was supplied by LiquidMetal Coatings® Corp., USA. The particles are homogeneous and spherical as shown in Figure 3.4. The elemental composition provided by the supplier is listed in Table 3.3, and the XRD pattern is shown in Figure 3.5. The XRD shows a halo peak between 40° to 46° without any sharp peak confirming full amorphous structure.

Table 3.3: elemental composition of the FeCrMoCB amorphous powder

Material	Fe	C	Cr	B	Mo
FeCrMoCB	Balance	3% max	30% max	3% max	20% max

** All values are in wt.%*

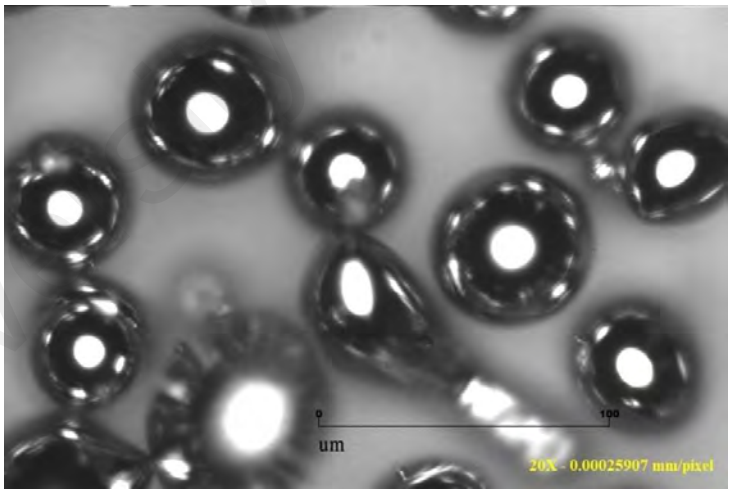

Figure 3.4: OM image of the FeCrMoCB powder

3.3. Sample preparation

The previously cut samples (30x30 mm) were ground using 240-grit SiC sandpaper, cleaned with ethanol, washed out using deionized (DI) water in ultrasonic bath to remove

grease, dirt, and other contaminations on the surface. Then the sample is dried in ambient air.

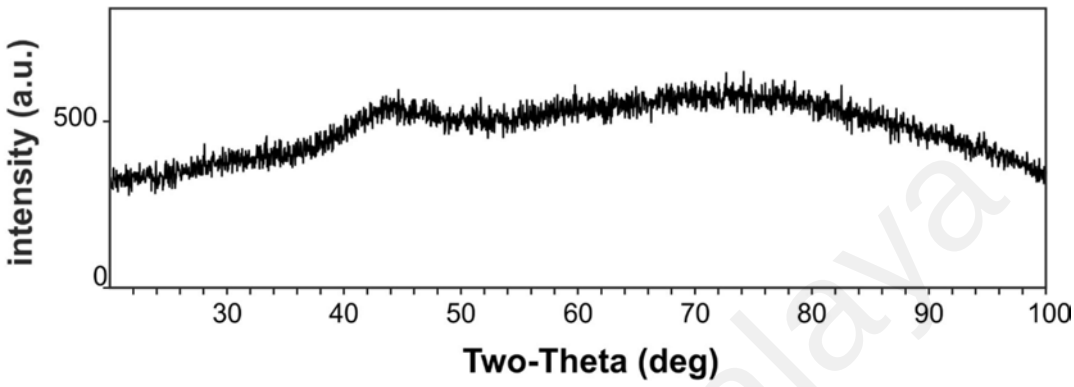

Figure 3.5: XRD pattern of as-received FeCrMoCB amorphous powder

First, the amount of powder needed for coating is calculated using equation (3.1).

$$mass = density \times area\ of\ sample \times thickness\ of\ preplaced\ layer \quad (3.1)$$

Where the density of the FeCrMoCB amorphous powder was 7.8 g/cm^3 and the desired thickness of preplaced layer is 300 to 400 μm which is assumed to be larger than 4 times of the particle size to ensure uniformity and homogeneous coating. Second, the powder was preplaced by spreading dry powder on the substrate surface, then ethanol is poured to facilitate distribution of particles, and then the samples were put in ultrasonic bath to ensure uniform preplaced layer. Finally, the preplaced layer was dried in ambient air.

A high-power diode laser machine – LDF 4000-60, LaserLine, Germany, with maximum power 4.4 kW, wavelength 978-1025 ±10 nm – was used to develop the coating. The laser head was attached to robotic arm to provide the scanning movement along the specimen. The LC process was held under shielding argon gas (10 liter/min.) to prevent oxidation during the process, Figure 3.6. The used laser head supports changeable spot size from

4x4 to 38x38 mm allowing flexible choice of spot size in the experiment, while a fixed working distance was set to 138 mm as recommended by the manufacturer.

3.3.1. Laser cladding parameters

Laser power (P), scanning speed (v) and spot size (d) are the three main parameters which affect the coating layer structure and properties. Due to the sensitivity of MG to the cooling rate, the overlap percentage – which defines the overlap between two adjacent cladding tracks – was considered in this study. Moreover, a study on the effect of the substrate surface roughness was investigated to optimize the coating layer geometry and structure.

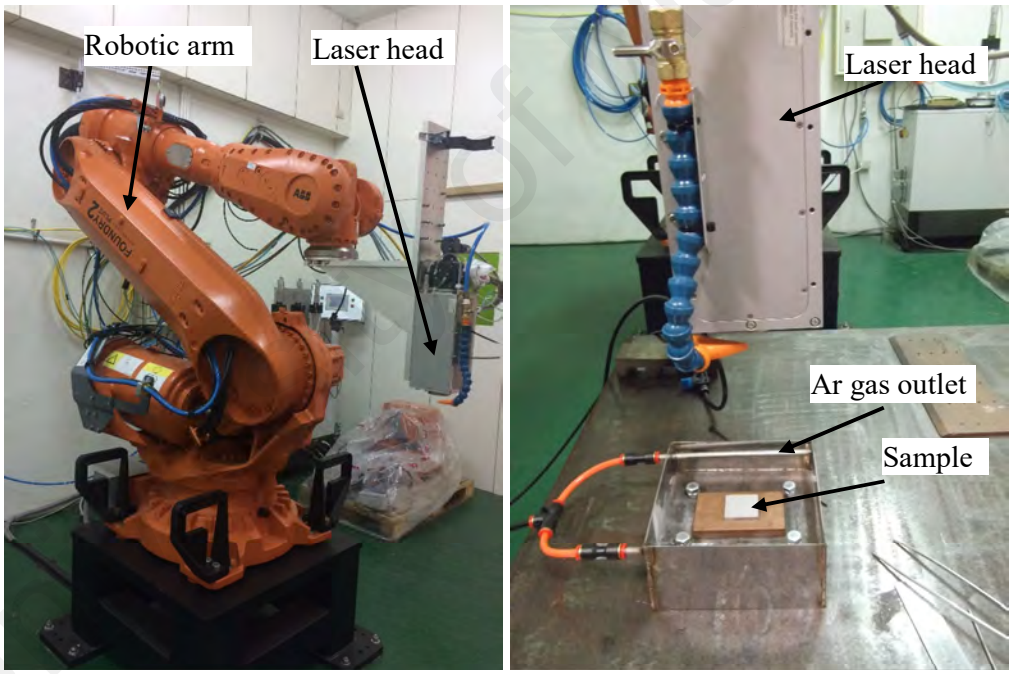

Figure 3.6: The laser head attached to the robotic arm and laser cladding setup

3.3.2. Laser cladding experiment

In order to optimize the characteristics of the coating layer, the experiments went into three stages; preliminary experiment, optimization of the substrate surface roughness, and optimization of the laser parameters.

3.3.2.1. Preliminary experiment

Preliminary experiments were held to determine the range of laser cladding parameters for a successful coating. So, single cladding tracks were fabricated according the array listed in Table 3.4 with a fixed spot size of 4x4 mm.

Table 3.4: Parameters array for preliminary experiment

Power (*P*), W	Scanning Speed (*v*), mm/s			
	Level 1	**Level 2**	**Level 3**	**Level 4**
500	3	5	10	20
1000	8	10	15	30
1500	5	10	20	50
2000	15	20	40	50
2500	50	60	75	85

3.3.2.2. Optimization of substrate surface roughness

It is important to study the geometry of the cladding tracks to optimize the overlap percentage in order to minimize the accumulated heat transferred to the coating layer during the laser cladding process. From the preliminary experiments, it is found that the width of the single cladded track was less than 2 mm of the spot size width (4 mm). So, an investigation to the effect of the substrate surface roughness on the geometry, phase transformation and hardness was made. To attain different substrate surface roughness, two techniques are used to prepare the substrate surface includes; SiC sandpaper (SP) polishing and sandblasting (SB). Two substrate samples were ground using SiC 150- and 240-grit sandpaper. Another two samples were sandblasted using Al_2O_3 abrasive particles with different sizes, 40- and 100-grit sizes to attain higher surface roughness. Then the samples were cleaned using deionized (DI) water then ethanol in the ultrasonic bath to remove any contamination and abrasive particles from the surface. The amorphous powder was preplaced on the substrate surface set to 300 μm layer thickness and the selected parameters are listed in Table 3.5.

Table 3.5: Parameters combination used to study the effect of substrate surface roughness on the geometry and properties of the FeCrMoCB MG coating layer

Sample code	Power, W	Scanning speed, mm/s	Spot size, mm	Surface Polishing method (mesh No.)
S1	2000	45	4x4	SP 240
S2				SP 150
S3				SB 100
S4				SB 40

3.3.2.3. Optimization of laser parameters

The laser parameters of concern in this study are laser power (P), scanning speed (v), laser beam spot size (d), and overlap percentage ($OL\%$). Conventionally, the specific energy (E_s) – calculated according to equation (3.2) – is considered a more descriptive index of the cladding process.

Table 3.6: Experiment array to optimize the laser cladding parameters

Sample	Laser Power, W	Scanning speed, mm/s	d (w*b), mm	OL, %	E, J/mm^2
S1	2000	30	4x4	25	4.17
S2	2000	25	4x4	35	5.00
S3	2000	20	4x4	50	6.25
S4	3000	25	6x4	25	5.00
S5	3000	30	6x4	35	4.17
S6	3000	20	6x4	50	6.25
S7	4000	20	8x4	25	6.25
S8	4000	30	8x4	35	4.17
S9	4000	25	8x4	50	5.00

$$E_s = \frac{P}{d \times v} \qquad (3.2)$$

Where E_s is in J/mm^3, P in W, d in mm^2, and v in mm/s. The E_s can be a measure of transmitted heat to the fabricated sample. Thus, the different E_s values will affect the

structure and the amorphicity of the FeCrMoCB MG coating layer. From the preliminary experiments, it is found that the range of E_s leading to successful and sound coating was from 4 J/mm^3 to 6 J/mm^3. However, as there might be an interaction effect between the studied parameters, three levels of each parameter were set according to Table 3.6. The parameters combination was built using Taguchi method to minimize the number of total experiments runs.

3.4. Tests and characterization

3.4.1. Material characterization

3.4.1.1. Morphology, macro-examination and surface roughness measurement

The morphology and macrostructure of the developed coating layer were investigated to ensure the defect-free coating (i.e. porosities, cracks, etc.). To ensure proper imaging, the samples morphology was ground to remove the top-formed oxide layer. The morphology and macro images were taken using optical microscope (OM, Olympus BX51M, Japan).

The surface roughness measurements were taken using confocal laser microscope (Keyence VK-X200, Japan). At least 3 points were taken and the average value was recorded. The surface roughness measurements were applied to substrate (after the sandblasting and sandpaper polishing), and wear-test samples.

3.4.1.2. Microstructure examination

For microstructure reveal, cross-sectional coupons of the fabricated samples were cut using abrasive grinding cutting machine. The cut-coupons were mounted on conductive phenolic mount to utilize the polishing and microstructure imaging.

The coupons were ground using rotating-disc polishing setup using 150, 240, 400, 600, 800-grit SiC paper under running stream of water, then polished using 1000, 1500, 2000, 2500, 4000-grit SiC paper, and finally polished using cloth-disc and 40 nm alumina

particles suspended in ethanol until mirror-like surface is obtained. For best results, each run last for 2 to 3 min. and the coupon was rotated 90° every 0.5 min to minimize scratches resulted from the polishing process. After each run, the coupons were rinsed with running water to remove ground particles and debris remained on the surface. Finally, the coupons were cleaned using DI water, then ethanol in ultrasonic bath to ensure particles and dirt-free surface. The polished coupons were etched using Linsenätzmittel solution (1000 mL ethanol, 70 mL HCl, 40 g $FeCl_3$, and 30 g $CuCl_2$) – recommended by the supplier – for 0.5 to 1 min.

The microstructure images were obtained using scanning electron microscope (SEM, Hitachi S-3000N, Japan) attached with energy dispersive spectroscopy (EDS, Falcon 60 EDS) to examine the elemental composition. The default operating voltage was 15 kV and 15 mm working distance.

3.4.1.3. X-ray diffraction examination

X-ray diffraction (XRD) examination was performed using Bruker D2 Phaser, Germany, using Cu K_α λ = 0.154060 nm, 2θ range of 0~140° and scanning rate 3° min^{-1}. A sample of 15x15 mm was cut from each sample. The sample surface was flattened using 80-grit SiC sand paper and polished with 150 to 800-grit SiC sandpaper under continuous stream of water, then the samples were cleaned with DI water and ethanol in ultrasonic bath.

The XRD pattern was analyzed using X'Pert HighScore Plus and the amorphous content (AC) was estimated using the constant background method by applying equation (3.3) (Ibrahim et al., 2019; Manne, Bontha, Ramesh, Krishna, & Balla, 2017).

$$AC = \frac{Area\ under\ the\ amorphous\ background}{Area\ under\ the\ XRD\ pattern}. \quad (3.3)$$

Figure 3.7 shows the area under the crystalline peaks and amorphous background. It should be noted that the area under the XRD pattern is equal to the area under the

crystalline peaks plus the area under the amorphous background. The both areas under the XRD pattern was determined using Microsoft Excel 2016.

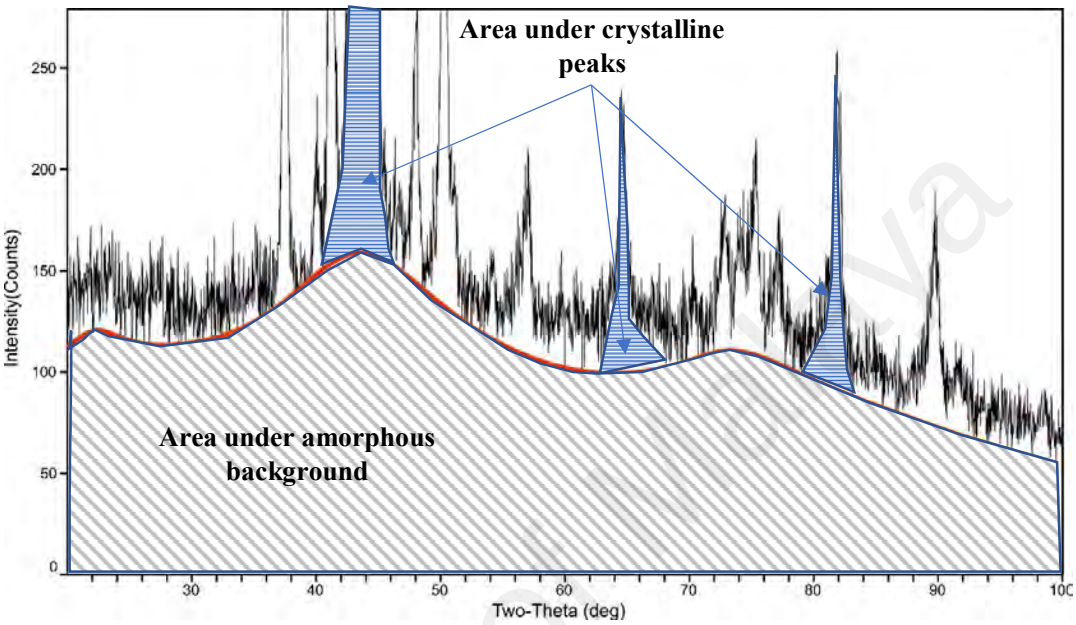

Figure 3.7: Area under crystalline peaks and amorphous background in the XRD pattern

3.4.1.4. Microhardness and nano-indentation measurements

The surface micro-hardness is measured using Vickers's micro-hardness tester (Mitutoyo HM-1300, Japan). The test load used was 100 g and the dwell time was 10 second. The average hardness of at least three points for each measurement was recorded. The hardness profile along the cross-section was taken at the coating layer, transition layer, interface and substrate with 0.1 mm distance between successive points to avoid the interference between the hardness indents.

The nano-indenter (MTS Nano G200, USA) was used for nano-indentation measurements. Three points for each sample were applied with maximum depth 1000 nm

and test rate of 10 nm/s. The nano-indentation was used to determine the surface hardness and Young's modulus of the coating layer.

3.4.2. Electrochemical corrosion and 30 days immersion tests

An electrochemical corrosion – potentiodynamic polarization – test was performed in SBF solution (pH 7.4) at 37° C to evaluate the corrosion resistance of the FeCrMoCB MG coating and compare it to the bare stainless steel (Cronidur 30). The samples were mounted in cold epoxy mold as shown in Figure 3.8, so the coating surface is only exposed during the test. The sample was set as working electrode (WE), Saturated Calomel Electrode (SCE) as reference electrode (RE) and platinum strip as counter electrode (CE) immersed in 250 ml of electrolyte. The phosphate buffer saline (PBS), prepared from lab-grade reagents were used as electrolyte with the composition listed in Table 3.7. The temperature of the electrolyte was kept at 37±1° C using hot plate and monitored using thermometer. The open circuit potential was kept for 40–60 min until saturation attained. Then, linear sweep voltammetry was applied from -1.5 to 1.5 V with scanning rate 10 mV/s using AutoLab Potentiostat/Galvanostat – PGSTAT204, by Metrohm, Netherland – supported with Nova software. The test setup is shown in Figure 3.9.

Table 3.7: PBS solution composition

PBS					
DI water	**NaCl**	**KCl**	**Na_2HPO_4**	**KH_2PO_4**	**HCl**
800 mL	8.00 g	0.20 g	1.44 g	0.24 g	Add to pH 7.4

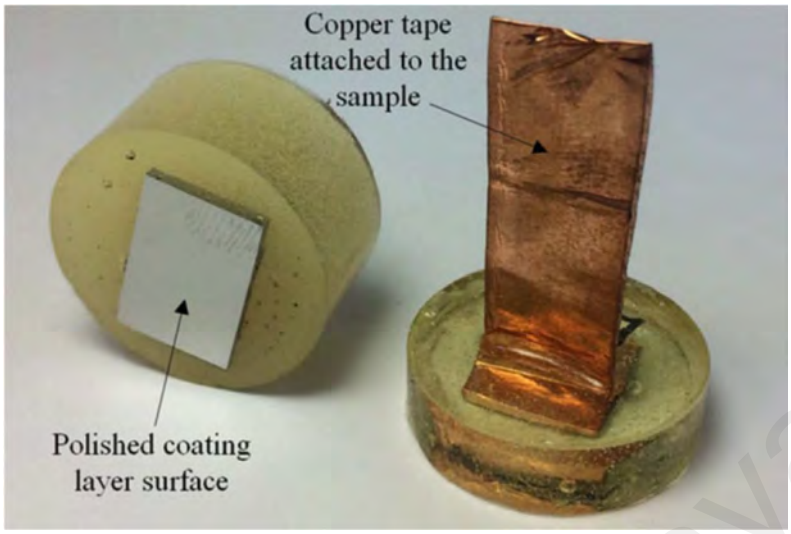

Figure 3.8: Prepared sample for electrochemical corrosion test

The corrosion current (i_{corr}) and corrosion potential (E_{corr}) were determined form the potentiodynamic polarization curve using the Tafel extrapolation method, and hence the corrosion rate (CR) was evaluated by applying equation (3.4).

$$CR = i_{corr} K \frac{EW}{\rho} \qquad (3.4)$$

Where i_{corr} is the corrosion current density in A/cm^2, K is a unit conversion constant (3.28 for mm/y), EW is the equivalent weight of the FeCrMoCB (19.16 atomic weight), and ρ is the density of the alloy.

A corrosion resistance of the FeCrMoCB coating over 30 days period was evaluated. The samples were immersed in PBS for 30 days, and every 3 days an electrochemical corrosion test was performed. This test gives the decay of the corrosion resistance in PBS over 30 days period of time. This test was performed on the optimized FeCrMoCB MG coating layer and compared with the uncoated substrate (Cronidur30). The corroded surfaces were gold coated using sputter coating and examined using SEM and EDS.

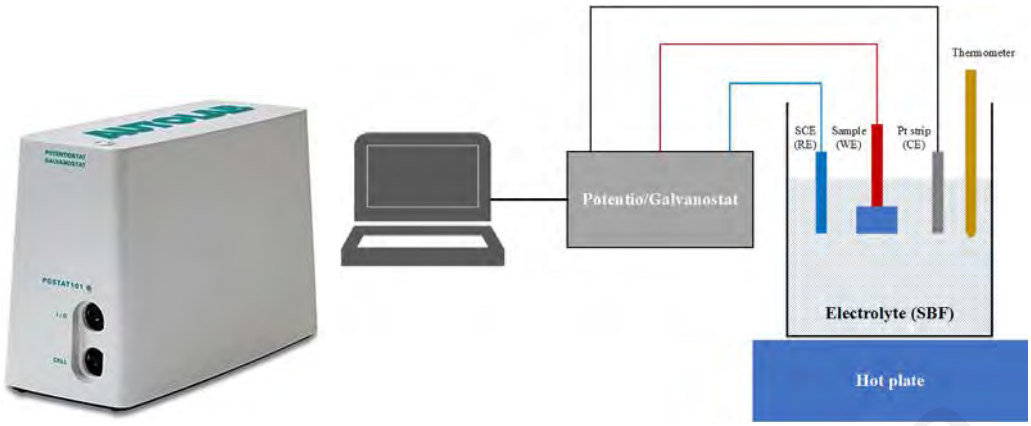

Figure 3.9: AutoLab Potentiostat PGSTAT204 and the 3-electrodes cell

3.4.3. Wear testing in dry and SBF environment

A dry wear test was done using the ball-on-disc test machine developed by Nanotechnology Research Center, Southern Taiwan University of Science and Technology, Taiwan. A schematic drawing of the wear test machine is shown in Figure 3.10. The sample 30x30 mm were ground to obtain flat surface, then polished to a mirror-like surface according to ASTM G-99-95a. A total 10 N normal load was applied to the 6.5 mm diameter alumina ball, and the sliding speed was set to 0.25 m/s for a total distance 500 m at room temperature. The mass of the samples before and after the test was measured using high precision balance with 0.1 mg accuracy, and the wear rate of the fabricated samples and the uncoated substrate was calculated according to equation (3.5) (ASTM G-99-95a, 2000).

$$W_r = \frac{V_{loss}}{D \times F} \qquad (3.5)$$

Where W_r is the wear rate (mm^3/N.m), V_{loss} is the volume loss in mm^3 ($V_{loss} = (m_{before} - m_{after})/\rho$), D is the total sliding distance (m), and F is the applied normal load (N).

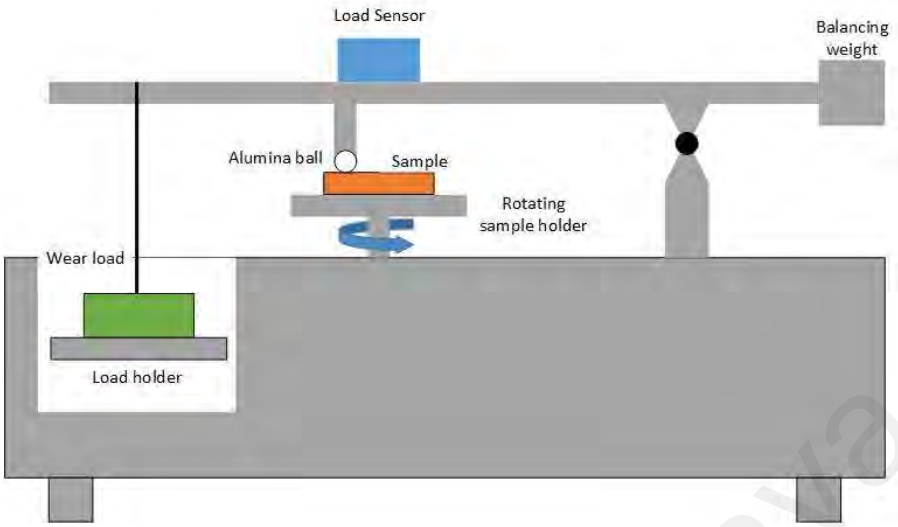

Figure 3.10: Schematic drawing of wear test machine

The bio-wear test was performed in SBF (Ringer's solution, pH 7.4) at 37±1 ^{o}C. Three samples with different amorphous content were selected to study the change in wear resistance with the amorphous content. The selected samples were S2, S5 and S7 and denoted as R1, R2, R3 respectively.

The wear test was performed for 500 m at 0.25 m/s sliding speed with a normal load (10 N) subjected to 6.5 mm diameter alumina Al_2O_3 ball. The wear scars were examined by SEM, EDS and the average surface roughness was evaluated using confocal laser microscopy.

3.4.4. Wettability test

A DI water drop test was performed and the contact angle was measured using the sessile drop technique. All the samples surfaces were polished to mirror-like surface. The resulting contact angle for the coated samples was compared to the contact angle of the uncoated substrate. Three points were taken and the average contact angle is recorded.

3.4.5. In-vitro bioactivity behavior in SBF

The SBF used for the in-vitro bioactivity test was prepared from lab-grade reagents according to a previous protocol proposed by Kokubo et. al (Kokubo & Takadama, 2006) with pH of 7.4, Table 3.8, and ion concentrations nearly equal to those found in human blood plasma. The test was performed by soaking 9x9 mm^2 4-mm thick coupons cut from the fabricated samples in 30 ml SBF using lab polymer bottles following the setup shown in Figure 3.11, and kept at 37±0.5 ^oC using lab incubator for 1 day, 3 days, 7 days, and 21 days. This setup minimizes the precipitates of compounds on the surface due to the gravity. Every two days, the test coupons were rinsed gently with DI water and the SBF was replaced with a fresh one. After each designated period, the samples were rinsed with DI water and dried in a desiccator to avoid damaging the apatite layer.

Table 3.8: SBF composition prepared for in-vitro bioactivity test

DI water	NaCl	$NaHCO_3$	Na_2CO_3	KCl	$K_2HPO_4.3H_2O$	$MgCl_2.6H_2O$	0.2M NaOH	HEPES	$CaCl_2$	Na_2SO_4	1M NaOH
750 ml	5.403 g	0.504 g	0.426 g	0.225 g	0.230 g	0.331 g	100 ml	17.892 g	0.293 g	0.072 g	To pH7.4

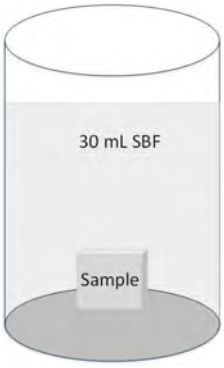

Figure 3.11: Schematic of in-vitro bioactivity test setup

Finally, the samples were gold coated using sputter coating and the apatite layer was examined by SEM and EDS to check the apatite layer morphology and Ca/P ratio.

3.4.6. Cell-culture test and in-vitro cytotoxicity test

Human bone osteoblast MG63 cells (Chi-Mei Foundation Hospital, Tainan, Taiwan) were used for cell-culture and in-vitro cytotoxicity tests. The cells were incubated at 37 ^{o}C and 5% CO_2 environment in DMEM (Dulbecco's modified eagle medium, Hyclone, USA) supplemented with 10% fetal calf serum, 100 U/ml penicillin and 100 U/ml streptomycin. For collecting the cells, the cell-medium was removed carefully, then cleaned with PBS. The cells were detached using LE express enzyme (Gibco, Denmark) and transferred to centrifuge tube. The cells were centrifuged at 1000 rpm for 5 min., the detaching enzyme was removed and finally, the cells were suspended in 10 ml prewarmed (37 ^{o}C) cell-medium. The cells per 1 ml were counted using hemocytometer with trypan blue stain.

The FeCrMoCB MG coated and Cronidur30 samples were cleaned by DI water, acetone, then ethanol in ultrasonic bath for 15 min for each. Then, the samples were kept in sealed packages. After that, the samples were sterilized in autoclave at 120 ^{o}C for 1 hr.

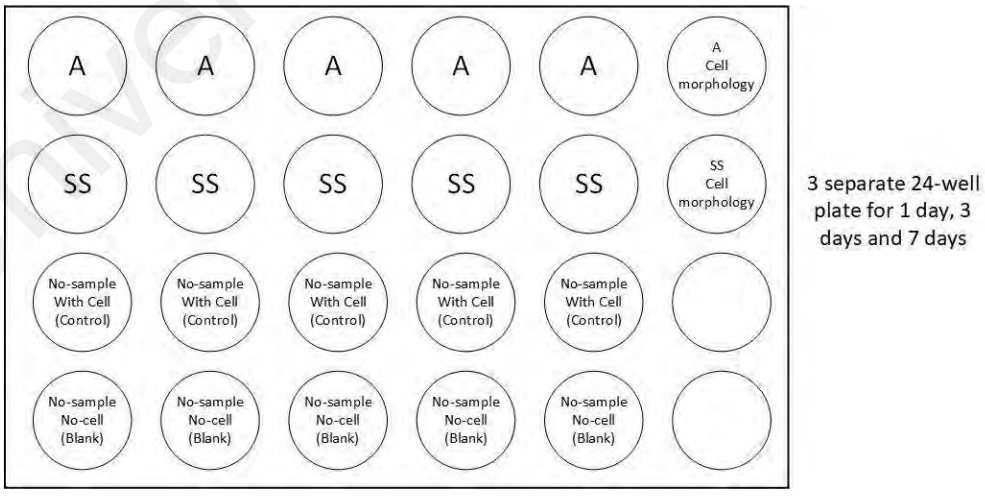

Figure 3.12: Samples layout in 24-well plate for cell-culture test

The samples were put into sterilized 24-well plate. The cells were seeded with total number of 10^4 cells for each sample. A no-sample well (control) and no-cell no-sample well (blank) were used to compare and normalize the results, respectively. A total of 18 samples (9x9 mm) of each were prepared for the cell-culture; 5 samples for cytotoxicity test and 1 sample for cell morphology, Figure 3.12, and cultured for 1 day, 3 days and 7 days in incubator at 37 ^oC and 5% CO_2. The cell-medium has been changed every 2 days. The test has been performed also for corroded samples (samples obtained after the electrochemical corrosion test).

3.4.6.1. Cell morphology protocol

First, the cells were fixed through the following protocol

1. Rinse the sample with warm PBS.
2. Fix with warm 2.5% glutaraldehyde in SEM buffer and incubate for 2 hrs.
3. Washout fix with SEM buffer (*0.1 M Na-phosphate buffer, pH 7.4 containing 0.1M Sucrose*) (2 times for 5 min each).
4. Dehydrate tissue with the following series (15 min in each wash):
   - 35% Ethanol.
   - 50% Ethanol.
   - 70% Ethanol.
   - 95% Ethanol.
   - 100% Ethanol.
5. Immediately, replace the final 100% Ethanol wash with hexamethyldisilane (HDMS), let HDMS evaporate in the hood.

Finally, the samples were gold coated using sputter coating method and the cell-morphology was examined using SEM.

3.4.6.2. Cytotoxicity evaluation

To evaluate the cytotoxicity of the FeCrMoCB MG was evaluated using MTT assay and compared with Cronidur30 and control samples. The protocol followed was

1. Remove the medium and wash the samples with PBS.
2. Add fresh 1 mL cell-medium.
3. Add 100 µL MTT solution (*3-(4,5-Dimethylthiazol-2-yl)-2,5-diphenyltetrazolium bromide*).
4. Incubate the cells for 2 hours in incubator at 37 ºC and 5% CO_2. Ensure the formation of formazan crystals using OM.
5. Remove MTT and add 500 µL DMSO.
6. Incubate for 10-30 minutes.
7. Transfer the purple solution to 96-well plate and measure the absorbance at 570 nm.

The absorbance at 570 nm was measured using Thermo-Fisher Multiskan 60, USA and the indices were recorded for each sample, control and blank. The cell-viability % was calculated according to equation (3.6).

$$cell\ viability\ \% = \frac{absorbance\ reading\ of\ test\ sample - absorb \quad reading\ of\ blank}{absorbance\ of\ control - absorbance\ reading\ of\ blank} \qquad (3.6)$$

3.5. Conclusion

In this chapter, we have discussed the materials used and the methods applied to prepare the test samples as well as the examinations and tests to evaluate the performance and the

biocompatibility of test samples. This chapter included the methodology followed to characterize the coating layer, the corrosion and wear resistance evaluation, the bioactivity and the cytotoxicity behavior.

CHAPTER 4: RESULTS, ANALYSIS AND DISCUSSION

4.1. Introduction

This chapter discusses the results and findings of the experimental work, the analysis of these findings and discusses with previous results obtained by other research works.

This chapter will be ordered according to the experimental steps mentioned in chapter 3; preliminary results, optimization of substrate surface roughness, and optimization of laser parameters.

4.2. Preliminary results

4.2.1. Macro surface morphology of single cladded tracks

Figure 4.1 shows the morphology of fabricated samples. The first and second group which are fabricated at 500 W (3 and 5 mm/s) and 1000 W (10 and 15 mm/s) showed irregular cladding tracks. The cladding tracks 500 W, 10 and 20 mm/s were unsuccessful because of insufficient input energy leading to non-melted preplaced powder, while the cladding track 1000 W, 30 mm/s resulted in droplets of FeCrMoCB MG which is a result of insufficient heating, and hence, the substrate surface temperature was below the required level to establish the metallurgical bonding. So, the melt pool shrinks forming small spherical droplets because of the surface tension phenomena (Barekat, Shoja Razavi, & Ghasemi, 2016). The cladding track 1000 W, 8 mm/s was sound with shiny surface, however, it was not considered as an optimum condition due to the low scanning speed which would decrease the productivity.

The third (1500 W) and fourth group (2000 W) had the same pattern and trend. At relatively low scanning speed (5 and 15 mm/s, respectively), the cladding tracks were dull and cladding marks were recognized along the surface. The excessive increase in the

scanning speed (50 mm/s) resulted in forming droplets of FeCrMoCB MG and incomplete cladding track. In contrast, the in-between scanning speeds lead to sound and smooth cladding tracks.

The last group (2500 W) showed irregular cladding tracks with unsmooth surface. It should be noted that higher power would lead to overheating the substrate and cause wrapping and distortion of the samples. So, the medium power levels (1500 and 2000 W) are preferred in this case and considered for further examinations.

Figure 4.1: Morphology of single cladded tracks

Figure 4.2 shows magnified images for the morphology of the fabricated samples at 1500 W. The cladding marks are clear at 5 mm/s, Figure 4.2 (a), while in Figure 4.2 (b) and (c), smooth surfaces were observed. Higher scanning speed resulted in formation of droplets (sphere-like) due to extremely high cooling rate. It is noted that no surface cracks were recognized on the surface of the developed FeCrMoCB MG cladded tracks indicating sound coating.

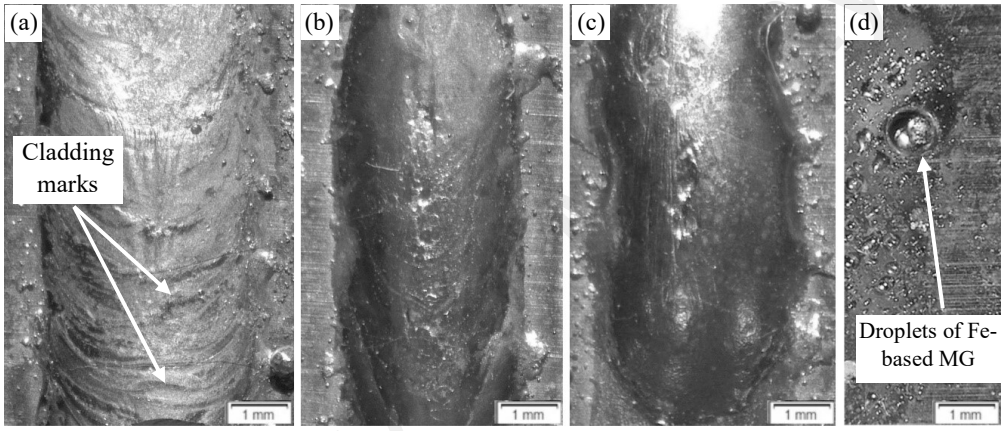

Figure 4.2: Magnified morphology of laser cladded tracks at 1500 W (a) 5 mm/s (b) 10 mm/s, (c) 20 mm/s, and (d) 50 mm/s

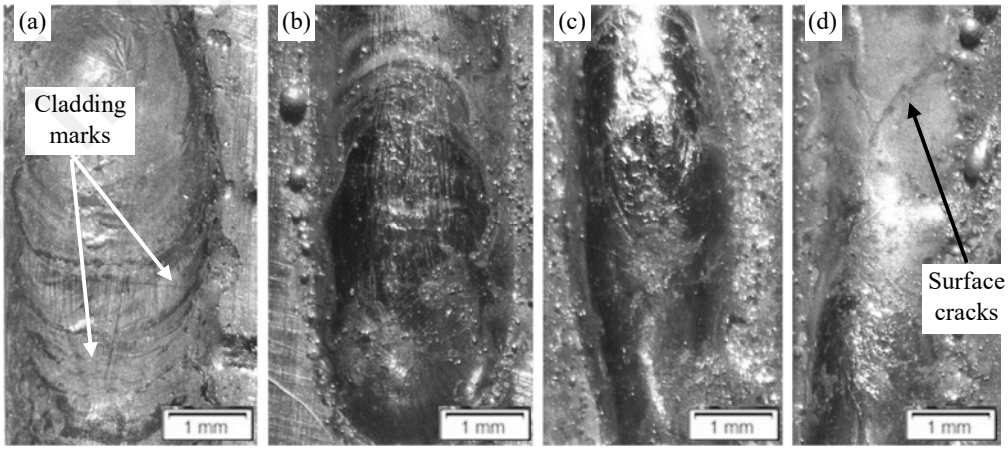

Figure 4.3: Magnified morphology of laser cladded tracks at 2000 W (a) 5 mm/s (b) 10 mm/s, (c) 20 mm/s, and (d) 50 mm/s

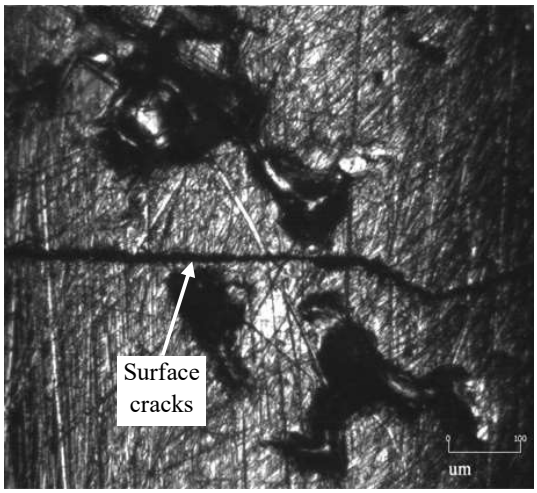

Figure 4.4: Optical microscope image showing crack on P2000 S50 surface (x100)

Figure 4.3 shows the fabricated samples at 2000 W at different scanning speeds; 15, 20, 40 and 50 mm/s, respectively. As can be seen in Figure 4.3, the cladded tracks showed smooth surfaces at scanning speeds 20 and 40, while the cladded marks existed at 15 mm/s. It is important to note that further increase in the scanning speed resulted in surface cracks on the cladded track, Figure 4.3 (d) and Figure 4.4 shows magnified image for the crack. The surface cracks usually result from relatively large difference in the thermal expansion between the coating layer and substrate caused by relatively high cooling rate (Li et al., 2015).

4.2.2. The microstructure of cladded tracks

In this section, the SEM imaging for the microstructure of laser cladded FeCrMoCB MG tracks at the cross-section was introduced. Figure 4.5 shows SEM imaging of the samples at 1500 W, 5 mm/s, 10 mm/s and 20 mm/s. Two SEM images were provided for each sample with 40x and 2000x magnification to investigate both coating layer (CL) and transition (TL), and the microstructure at the interface (IF). All the samples showed crack-free coating. At lower scanning speed (5 mm/s) shown in Figure 4.5 (a) and (b), the SEM

image showed a high degree of crystallinity within amorphous matrix near the interface. Inversely, at higher scanning speeds (10 and 20 mm/s shown in Figure 4.5 (c, d, e and f)), the coating tends to have higher percentage of amorphous structure within the CL as the cooling rate is higher and sufficient for amorphous forming (Chien, Liu, & Kuo, 2016; Gao et al., 2003). Furthermore, the TL with crystalline structure would prove a good dilution which indicates enhanced adhesion strength between the coating and the substrate (Shu et al., 2016; Yue, Su, & Yang, 2007). But, at higher scanning speed, Figure 4.5 (f), columnar-shaped crystals were formed at the interface and equiaxed crystals were formed at the TL within amorphous matrix. The columnar crystals are formed because of the directional cooling at the interface and higher cooling rate, while the equiaxed crystals result from isotropic directional cooling in TL.

As can be seen in Figure 4.6, the samples also showed crack-free coating layer along the cross section the same as the samples fabricated at 1500 W. Furthermore, in Figure 4.6, the CL and TL are formed with various thicknesses at different scanning speeds. The top coating showed amorphous structure with low degree of crystallinity. At the TL, crystals are formed within the amorphous structure.

Comparing the microstructure obtained in samples fabricated at 1500 W and 2000 W, it is observed that samples fabricated at 1500 W, 5 mm/s and 10 mm/s showed almost the same microstructure of the samples fabricated at 2000 W, 15 mm/s and 20 mm/s, respectively. This indicates that the laser power has more significant effect on the microstructure as the increasing of the laser power by 33.33% (from 1500 to 2000 W) required increasing the scanning speed by 150%-200% (from 5 to 15 mm/s) to obtain similar microstructure features.

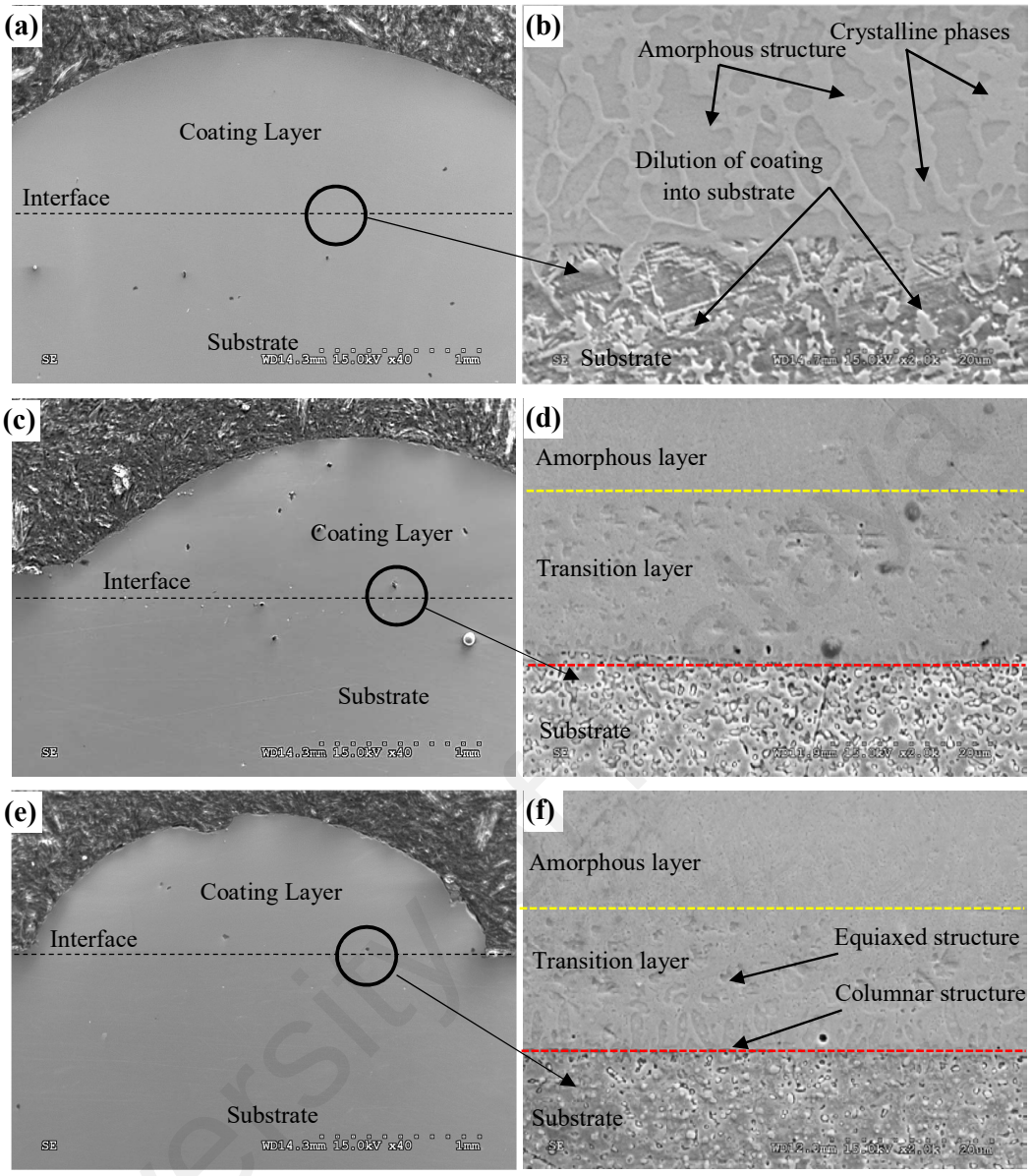

Figure 4.5: SEM imaging of CL at 1500 W (a) 5 mm/s 40x, (b) 5 mm/s 2000x, (c) 10 mm/s 40x, (d) 10 mm/s 2000x, (e) 20 mm/s 40x, (f) 20 mm/s 2000x

4.2.3. XRD examination

Figure 4.7 shows the XRD pattern of the as-received FeCrMoCB amorphous powder, Figure 4.7 (a), ASTM F2229 and the yellow tape, Figure 4.7 (b). As can be seen, the FeCrMoCB amorphous powder has full amorphous structure, while ASTM F2229 SS has a typical crystalline structure with peaks at $2\theta = 44.6^{o}$, 64.8^{o}, 82.17^{o} and 98.2^{o}. The yellow tape peaks were at $2\theta = 29.6^{o}$, 31.1^{o}, 36.2^{o}, 39.5^{o}, 47.8^{o}, and 48.6^{o}.

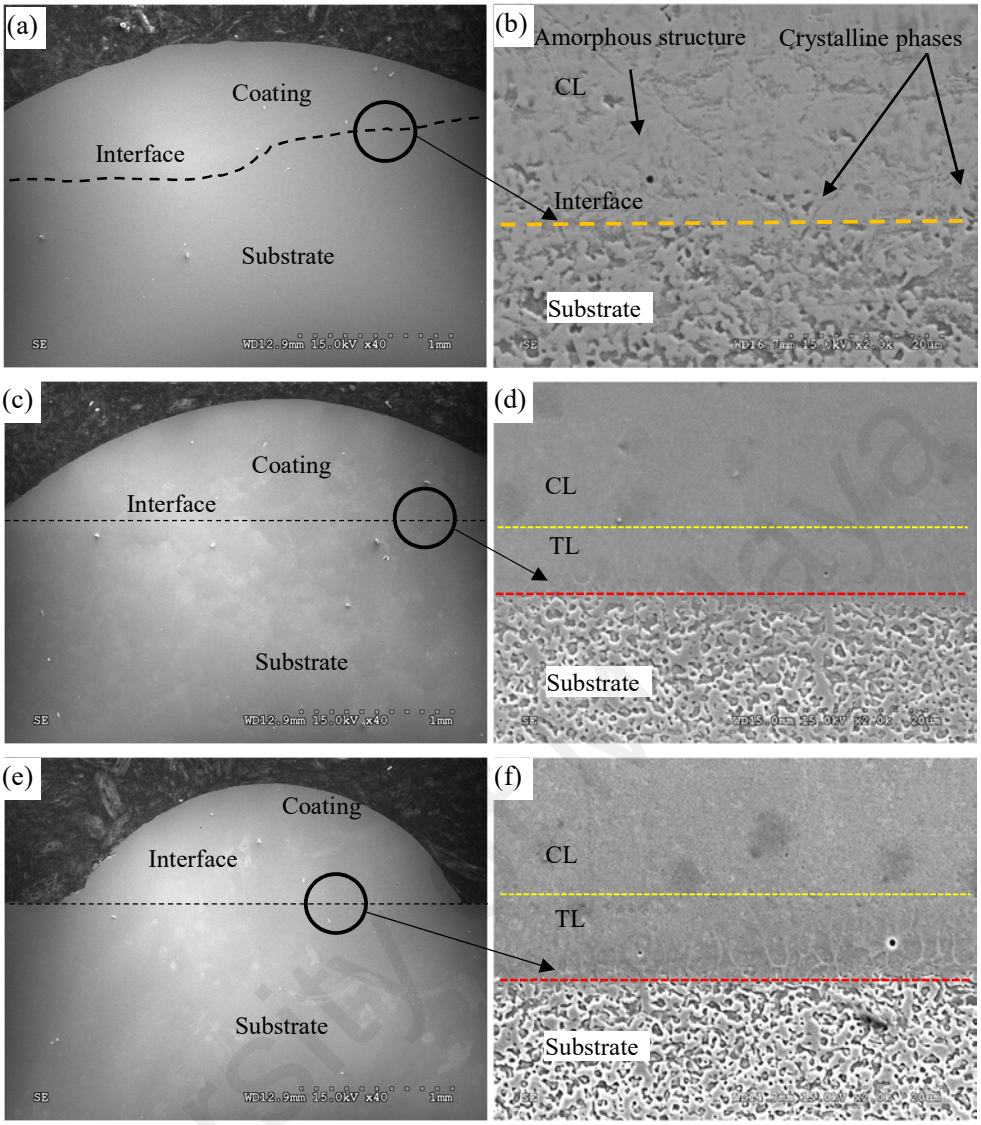

Figure 4.6: SEM imaging of CL at 2000 W, (a) 15 mm/s 40x, (b) 15 mm/s 2000x, (c) 20 mm/s 40x, (d) 20 mm/s 2000x, (e) 40 mm/s 40x, (f) 40 mm/s 2000x.

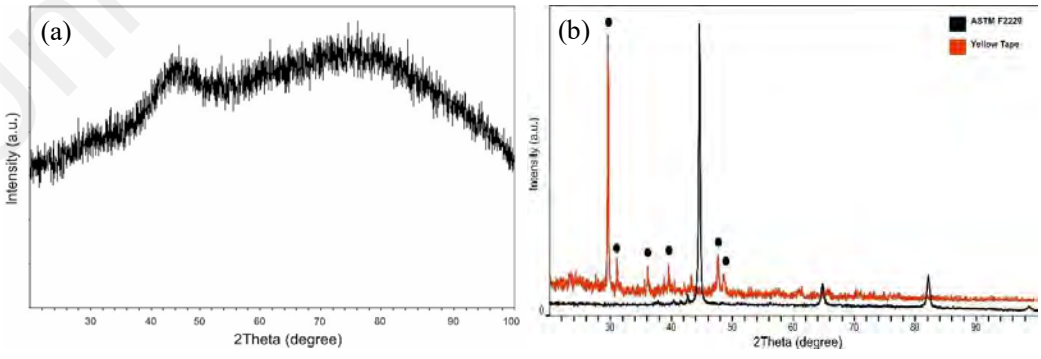

Figure 4.7: XRD pattern of (a) Fe-based amorphous powder, (b) ASTM F2229 sample and Yellow tape

Figures 4.8 shows the XRD patterns of cladded tracks. It is noticed that all samples exhibited formation of α-Fe crystalline phase. However, different amorphous content percentage was found as stated in Table 4.1. It is obvious that increasing the laser power resulted in decreasing the amorphous content within CL and increasing the degree of crystallinity. Contrary, the increase of scanning speed resulted in enhancing the amorphous structure.

Table 4.1: Amorphous content percentage exhibited in the CL for the fabricated samples

Sample	Amorphous content, %
P1500 *v*5	76.6
P1500 *v*10	83.2
P1500 *v*20	87.8
P2000 *v*15	76.8
P2000 *v*20	82.5
P2000 *v*40	84.5
P2000 *v*50	84.7

**The (P) denotes to the used power and (v) denotes to the scanning speed*

From the XRD patterns, it is noticed that at the same power level, the increase in the scanning speed results in increasing amorphous content within CL. Further increase in scanning speed does not cause significant enhancement, but over increase in scanning speed resulted in unsuccessful coating as shown in Figure 4.1 and 4.2 (for example P1500 *v*50). This can be explained by the effect of cooling rate; at the same power level, as the scanning speed is increased, higher cooling rate takes place, which facilitate amorphous structure formation. However, over increase in the scanning speeds results in decreasing the interaction time (interaction time = spot size/scanning speed) which leads to insufficient heating, and hence, the substrate surface temperature was below the required level to establish the metallurgical bonding.

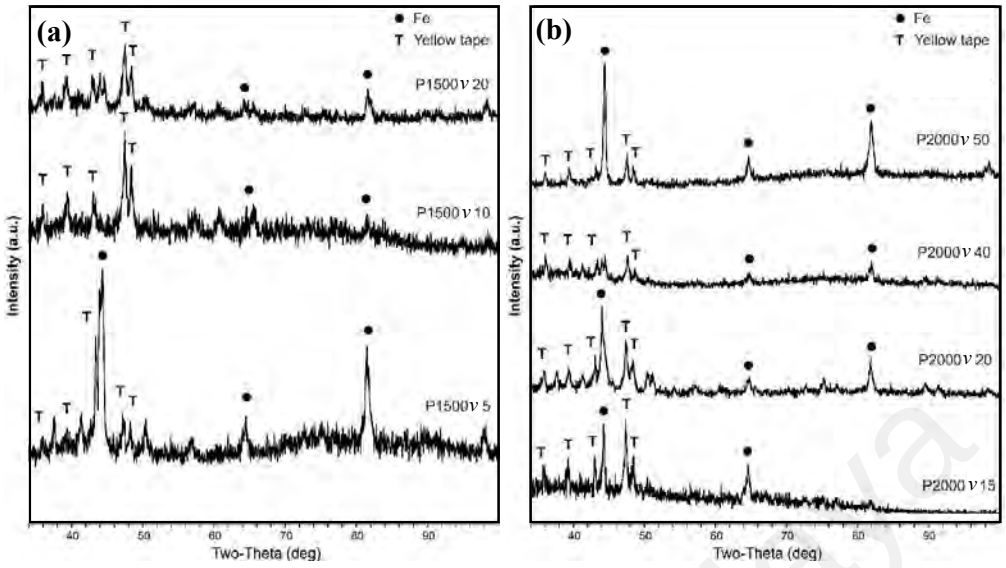

Figure 4.8: XRD pattern of fabricated samples (a) at 1500 W (b) at 2000 W

In the meanwhile, it is found that the changing of the power level simultaneously with scanning speed is also significantly affects the amorphous structure formation, but laser power has stronger effect on the obtained structure. As an example, by increasing laser power by 33.3% and increasing the scanning speed by 100%, the sample P1500 v10 showed almost the same amorphous content as sample P2000 v20. This can be explained as the increasing laser power leads to higher heat transferred and deeper penetration of laser beam which leads to higher degree of crystallinity of CL although increasing the scanning speed increases the cooling rate. This confirms the significant effect of laser power on the phases obtained within CL.

4.2.4. Line scan analysis

Line scan analysis is performed to investigate the elemental distribution through the CL, TL, interface and substrate. Figure 4.9 shows line scan along the cross-section of cladded tracks P1500 v5, P1500 v10 and P1500 v20. As can be seen, line scan showed excellent dilution between the CL and the substrate at the interface especially at relatively low scanning speed, P1500 v5 in Figure 4.9 (a), as the distribution trend of Fe, Cr, and Mo

along the CL, TL, interface and substrate is almost the same. However, in the other two samples - P1500 *v*10 and P1500 *v*20, sudden increase in Cr and Mo, and sudden decrease in Fe took place at the interface, Figure 4.9 (b) and (c), interpreting the composition difference between the substrate and the CL.

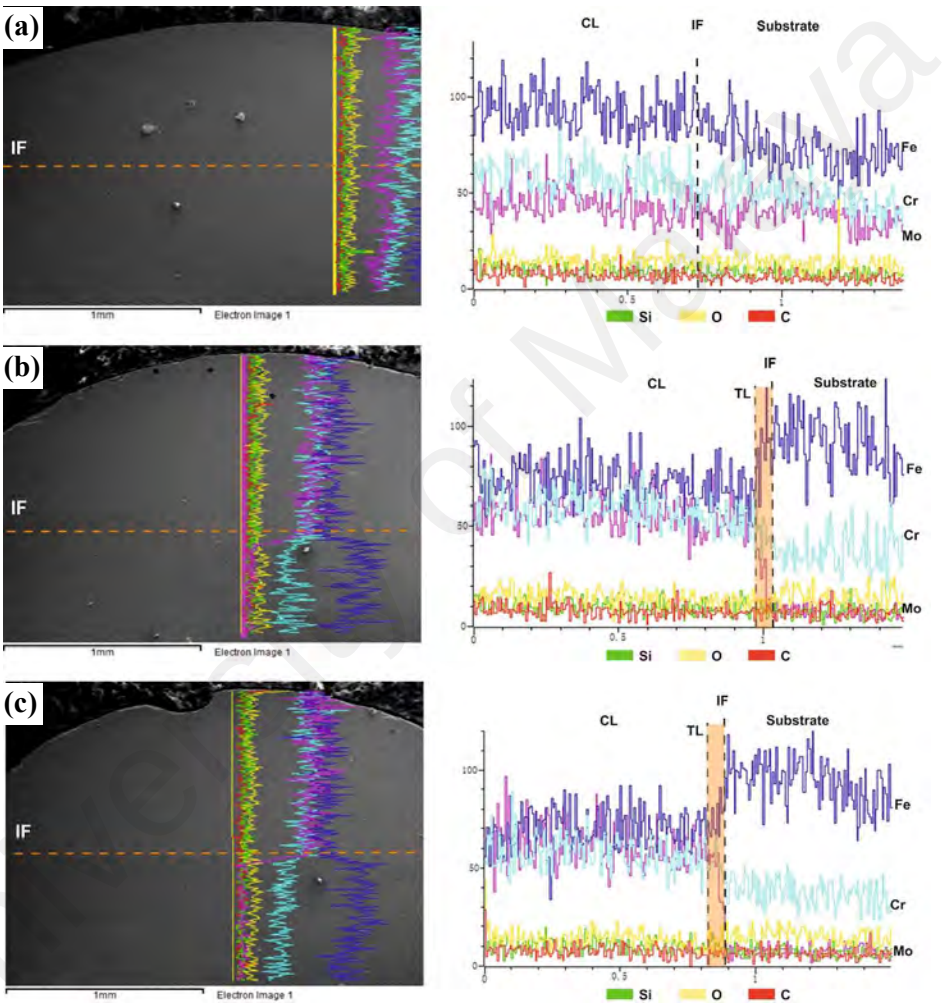

Figure 4.9: Line scan of FeCrMoCB MG coating (a) P1500 *v*5, (b) P1500 *v*10, (c) P1500 *v*20

Figure 4.10 (a, b, c, d) shows the line scan of samples P2000 *v*15, P2000 *v*20, P2000 *v*40 and P2000 *v*50. As can be seen in Figure 4.10 (a), a gradual increase of Fe and Cr content from the substrate to CL is detected. This reveals good dilution between the CL and

substrate at the interface and confirms the formation of high degree of crystallinity coating. However, in Figure 4.10 (b), (c), and (d), the sudden increase of Cr and Mo and decrease of Fe content in the substrate zone to the CL indicates the less dilution and confirms higher percentage of amorphous coating.

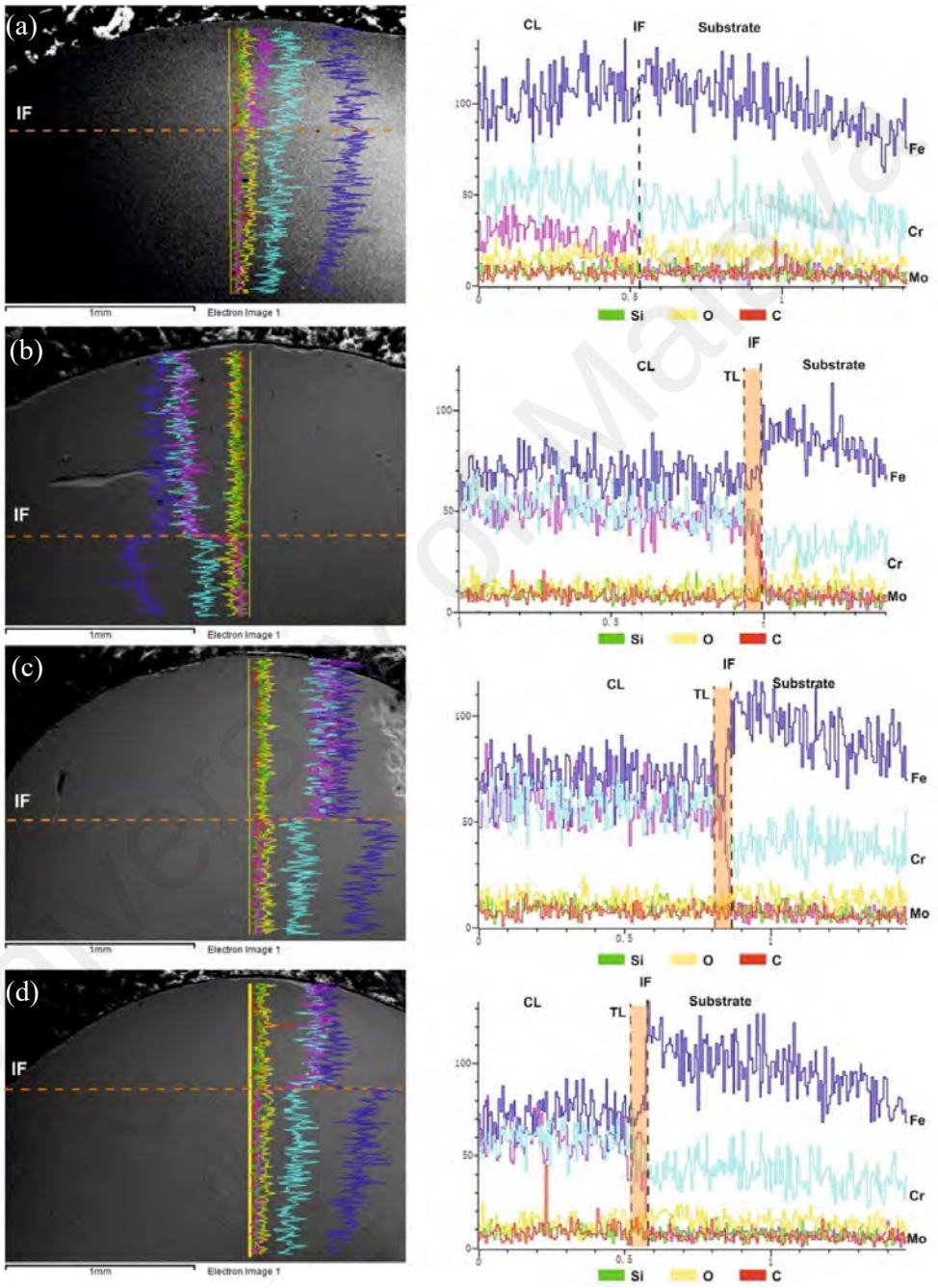

Figure 4.10: Line scan of samples (a) P2000 *v*15, (b) P2000 *v*20, (c) P2000 *v*40, (d) P2000 *v*50

4.2.5. Hardness Measurements

Figure 4.11 shows the hardness values measured along the samples P1500 *v*5, P1500 *v*10, and P1500 *v*20 cross-sections illustrating the CL, TL, HAZ and substrate zones.

It is noticed that the hardness of the FeCrMoCB MG CL is near to 1300 HV0.1 – which is comparable to those obtained by others (Lee, Nam, Lee, & Kim, 2006; D. Liang et al., 2018; X. Liang, Chen, Mora, Fernandez Urdaneta, & Zeng, 2017; Sun et al., 2014; Wu & Hong, 2001; Zhu et al., 2013) – for P1500 *v*10 and P1500 *v*20, while the substrate hardness is around 230 HV0.1, confirming about 6 times increase in the hardness in CL. TL shows lower hardness value than CL (500-600 HV0.1), but higher than the substrate hardness. This reveals the existence of crystalline phases at the TL which decrease the hardness value (Tlotleng, Akinlabi, Shukla, & Pityana, 2014). It is also observed that the HAZ induced higher hardness than the substrate because the effect of dilution between the CL and substrate. Furthermore, it is noted that the thickness of CL, TL and HAZ are affected by the scanning speed. As the scanning speed is decreased, the formed layers thicknesses are increased, shown in Figure 4.11.

In the contrast, at the lower speed (P1500 *v*5), the crystalline structure within CL showed significant drop of the hardness to less than 900 HV0.1. This can be explained such that at the same power level and lower scanning speed lead to higher heat transmitted to the melting pool and lower cooling rates. The temperature increases significantly up to the recrystallization level and hence the CL has higher degree of crystallinity which is revealed in SEM and XRD examinations. However, in the TL section, hardness value of P1500 *v*5 is almost same as P1500 *v*10 and P1500 *v*20 as they have the same crystalline structure within amorphous matrix. In addition, The HAZ layer became deeper into the substrate and lead to increase the hardness value.

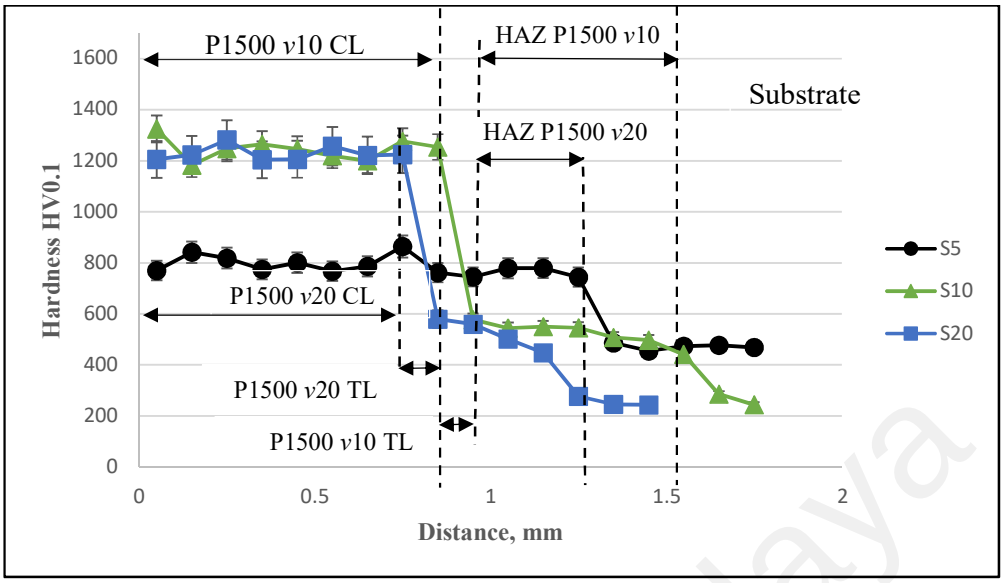

Figure 4.11: Hardness profile along the cross-section of samples P1500 *v*5, P1500 *v*10 and P1500 *v*20

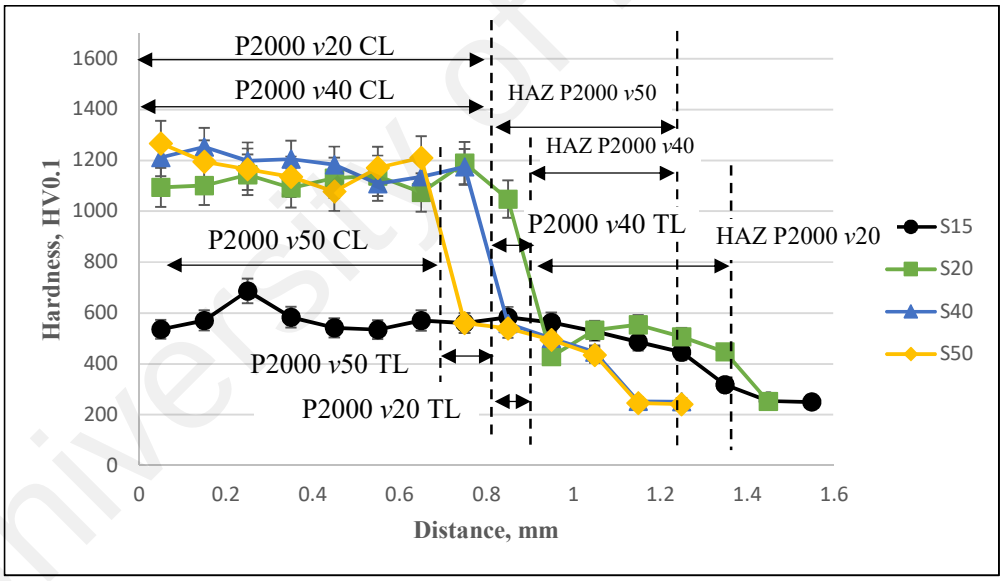

Figure 4.12: Hardness profile along the cross-section of fabricated samples P2000 *v*15, P2000 *v*20, P2000 *v*40 and P2000 *v*50

Figure 4.12 shows the hardness value along the cross-section of fabricated samples P2000 *v*15, P2000 *v*20, P2000 *v*40 and P2000 *v*50. As can be seen in Figure 4.12, the hardness trends of the samples fabricated at 2000W are almost similar to hardness trends of the

samples fabricated at 1500W. In Figure 4.12, it is noticed that at scanning speed of 20, 40, 50 mm/s, the hardness value of CL is exceeding 1200 HV0.1. However, at lowest scanning speed of 15 mm/s, the hardness value drops below 600 HV0.1, which indicates the existence of crystalline phases within the CL.

As a conclusion from the previous discussion, the hardness behavior at the CL and TL at different scanning speed revealed that scanning speed has a significant effect on the resulted coating hardness. This because of that the degree of crystallinity is increasing inversely with the scanning speed, leading to lower hardness, but improves the dilution between the CL and the substrate.

4.3. Optimization of substrate surface roughness

4.3.1. The surface roughness of the substrate samples

A 3D profile of the samples produced at SP-240, SP-150, SB-100 and SB-40 are shown in Figure 4.13 (a, b, c and d), respectively. As can be seen in Figure 4.13 (a) and (b), the sandpaper polished samples showed smooth and flat surface pattern, but the samples exhibited scratch marks resulted from the polishing process. However, from Figure 4.13 (c) and (d), the sandblasted samples showed homogeneous roughness pattern. Using 40-grit resulted in coarse surface pattern while using 100-grit resulted in a fine surface pattern. The average R_a values of three points with the corresponding standard deviation are stated in Table 4.2. As can be seen, the R_a values of the sandblasted samples were significantly higher than the R_a of the sandpaper polished samples.

Table 4.2: Average R_a values of different substrate surface preparation

Sample	Polished		Sandblasted	
	S1 (SP-240)	S2 (SP-150)	S3 (SB-100)	S4 (SB-40)
R_a	0.348±0.032	0.486±0.030	1.824±0.049	2.157±0.060
Standard deviation	0.0261	0.0244	0.0400	0.0489

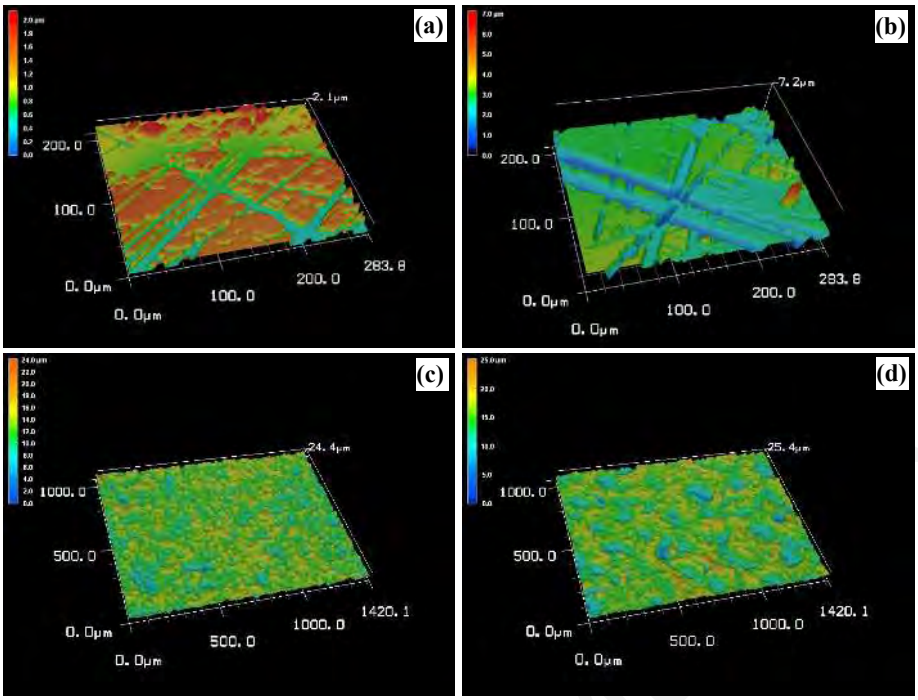

Figure 4.13: 3D profile of substrate surface (a) SP-240, (b) SP-150, (c) SB-100, (d) SB-40

4.3.2. The geometry of laser cladded tracks

Figure 4.14 shows a sample of the OM images of the laser cladded samples cross-section on different substrate surface roughness. The laser cladded tracks average width (L1) and height (L2) of five measurements are listed in Table 4.3. In addition, the laser cladded tracks width (L3) is measured at the heights of 300 μm (equal to the preplaced layer thickness). Finally, the penetration of the coating layer into the substrate (L4) is measured and recorded in Table 4.3. L4 is mainly representing the penetration of the cladded track into the substrate. As can be seen in Figure 4.14, for SP samples, the increase of the R_a caused increasing the L4 which was the same for the SB samples. As L4 does not follow a certain trend with R_a, this can be a random variation took place during the laser cladding process.

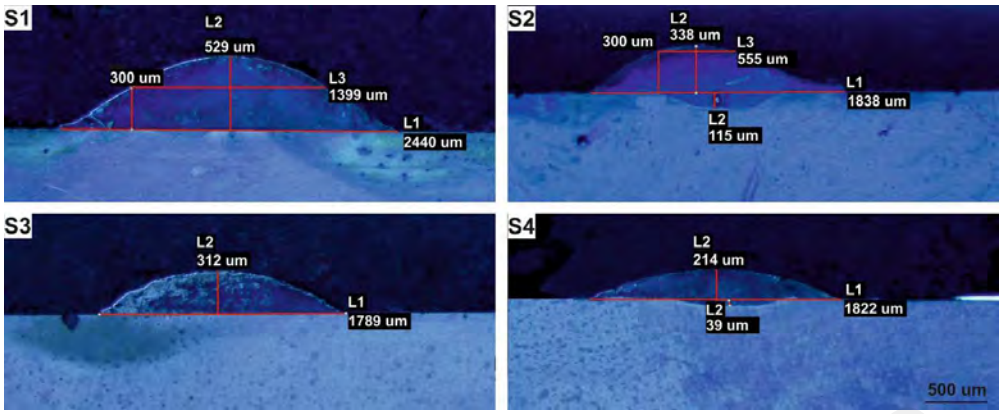

Figure 4.14: OM images for the laser cladded profile with the geometry measurements

Table 4.3: Track geometry dimensions represented by L1, L2, L3 and L4 in mm

Sample	Geometry dimensions, mm			
	L1	**L2**	**L3**	**L4**
S1	2.562±0.122	0.514±0.015	1.497±0.098	N/A
S2	1.946±0.110	0.338±0.016	0.595±0.040	0.120±0.005
S3	1.780±0.089	0.330±0.018	N/A	N/A
S4	1.822±0.127	0.212±0.008	N/A	0.040±0.001

Figure 4.15 shows a comparison between the obtained values; width, height, a width measured at 300 µm height, and the penetrations per different substrate surface roughness. As can be seen, it is clearly observed that sample S1 (SP-240) has the widest and highest clad track with negligible penetration depth (L4) into the substrate. So, increasing the R_a values of the substrate resulted in decreasing the width and height of the cladded track. According to previous studies (Liu, Qin, Huang, Hu, & Ni, 2018; Nenadl, Ocelík, Palavra, & Hosson, 2014), the laser cladded track tends to have the concave shape because of the cohesive forces (F_c) of the molten coating material. However, the adhesion force (F_a) between the molten coating layer and the substrate is in the opposite direction of F_c which hinder the flow of molten material toward the center. Normally, the F_c is constant as the

coating material is the same, but F_a is increasing with increasing R_a. So, the geometry of the laser cladded track is affected by the resultant force (F_c - F_a) as illustrated in Figure 4.16. Furthermore, the increase of F_a leads to forming droplets and decreasing the cross-section area of the laser cladded tracks ($A_{S1}>A_{S2}>A_{S3}>A_{S4}$). The cross-section area of laser cladded track is inversely proportional to the surface roughness.

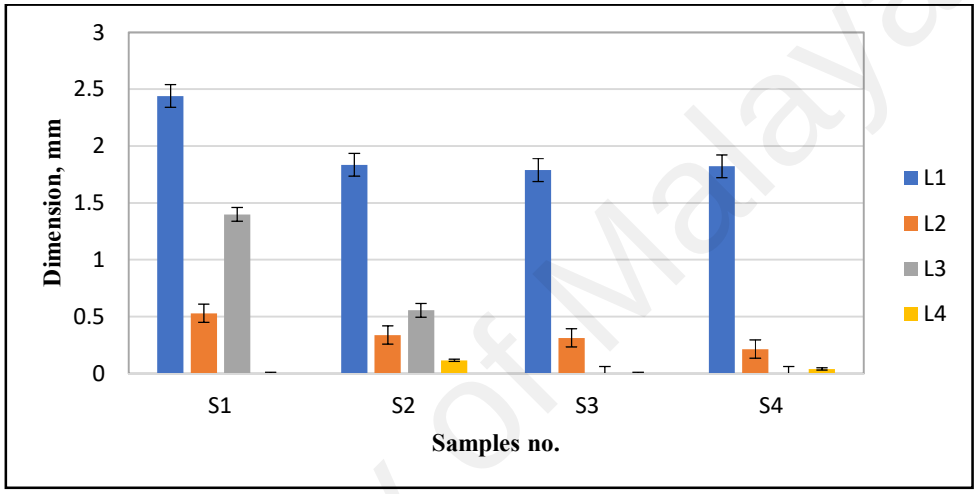

Figure 4.15: Comparison of the obtained values of the geometry L1, L2, L3, and L4

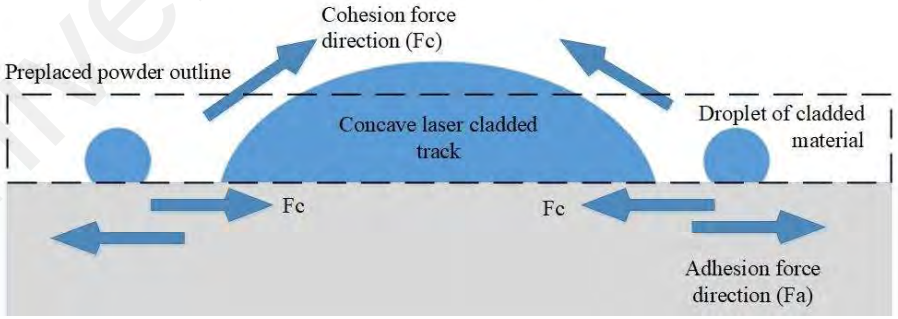

Figure 4.16: Illustration of the effect of the cohesion and adhesion forces on forming droplets of cladded material

Based on this finding we can conclude that the substrate surface roughness has a significant effect on the Fe-based MG cladded track geometry. The SP samples showed better results than SB samples in terms of larger dimensions and higher penetration.

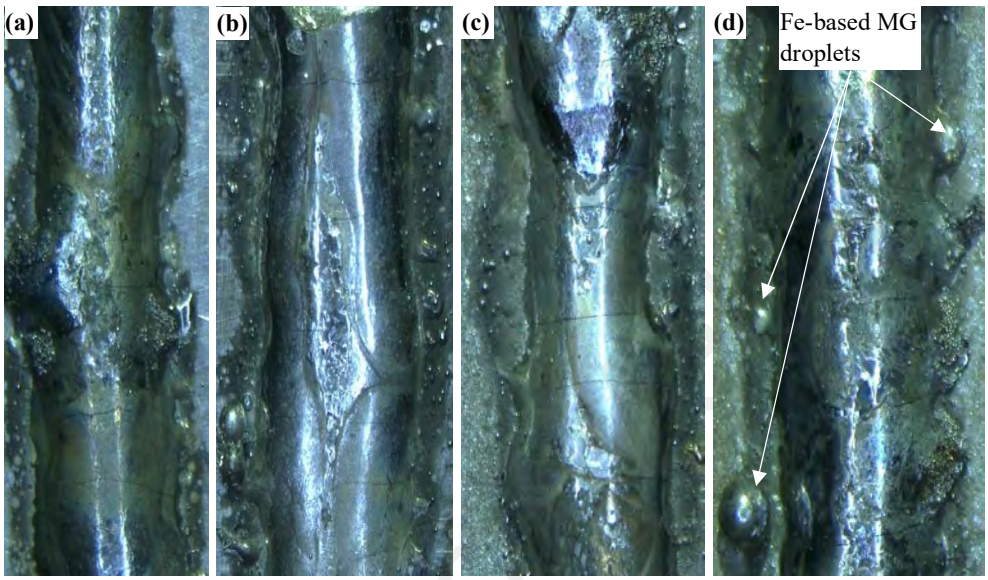

Figure 4.17: Fe-based cladded tracks of (a) S1, (b) S2, (c) S3, (d) S4

4.3.3. XRD analysis

Figure 4.18 shows the XRD of samples S1, S2, S3 and S4. It is noted that all samples showed halo peak (40^o to 50^o) which confirm the amorphous structure, besides crystalline phases. The amorphous content percentages for each sample are presented in Table 4.4. It is observed that the SB samples showed relatively higher amorphous content than the SP samples with an average of 3%. The major parameter affecting the amorphous formation (glass forming ability (GFA)) is the cooling rate such that the higher the cooling rate, the higher amorphous content percentage is obtained. Since the heat within the molten coating layer is dissipated through conduction from the bottom with the substrate and through convection with the Ar gas stream from the top. The apparent area of the cladding track would affect the cooling time as the smallest apparent area should decrease

the cooling time resulting in higher amorphous content. This can explain the increase of the amorphous contents with the increase of R_a values as the cross-section area of laser cladded tracks is decreasing.

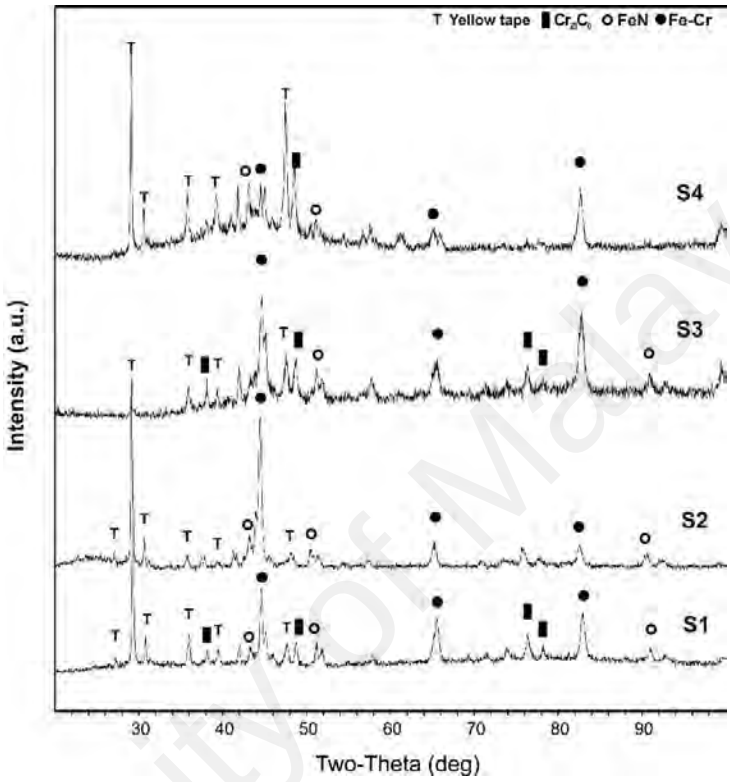

Figure 4.18: XRD pattern of the samples

Based on Table 4.4, samples S1 and S2 exhibited slower cooling rate with less amorphous content with higher intermetallic compounds ($Cr_{23}C_6$ and FeN) percentage (Kartik, Veerababu, Sundararamanc, & Satyanarayana, 2015) besides the metallic phase Fe-Cr, while samples S3 and S4 exhibited higher amorphous contents with higher metallic phase Fe-Cr percentage. Although, the difference in amorphous content is not significant, the intermetallic compounds percentages showed significant differences. The combination between the amorphous content and the intermetallic compounds percentage would affect the resultant hardness of the coating layer.

Table 4.4: Amorphous content percentage of the fabricated samples

Sample	S1 (SP 240)	S2 (SP 150)	S3 (SB 100)	S4 (SB 40)
Amorphous content, %	76.0	77.6	81.5	78.1
Metallic phase	15.2	18.7	17.8	20.9
Intermetallic compound	8.8	3.7	0.7	1.0

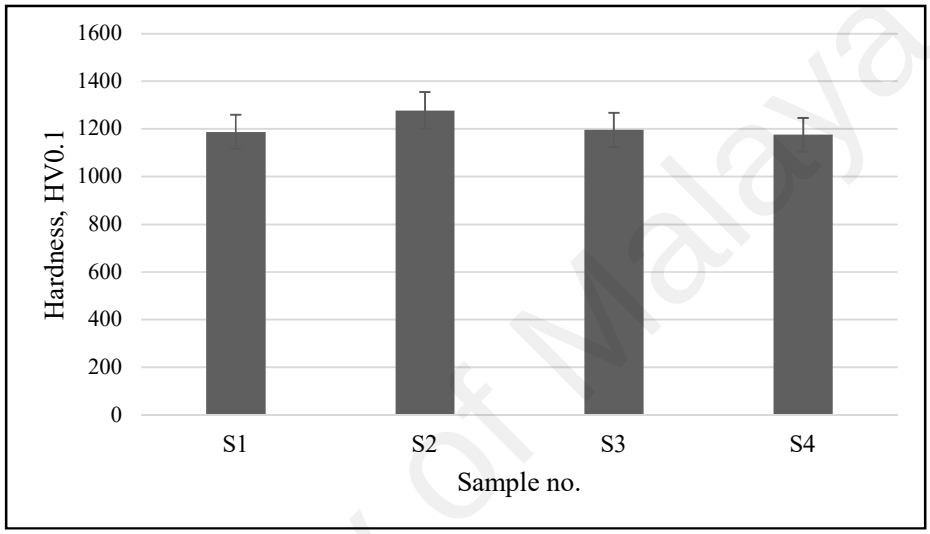

Figure 4.19: Surface hardness values of fabricated samples

4.3.4. Microhardness measurement

The obtained average micro-hardness values are shown in Figure 4.19. The hardness value of the fabricated samples showed insignificant variations with the change of the substrate R_a. This can be explained based on the effect of the recognized phases within the coating layer. Generally, the higher amorphous content would have higher hardness value (Audebert, Colaço, Vilar, & Sirkin, 2003; Ramasamy et al., 2016; Trexler & Thadhani, 2010). However, the metallic phases degrade the hardness value while the intermetallic compounds enhance the hardness. The resulting hardness is the combined hardness of the three phases; amorphous structure, metallic and intermetallic compound phases. In samples S1 and S2, the intermetallic compounds ($Cr_{23}C_6$ and FeN) which have

high hardness values showed high percentages with lower amorphous content, while in the samples S3 and S4 the metallic phase (Fe-Cr) percentage were high with higher amorphous content. So, the hardness values were very close in fabricated samples.

4.4. Optimization of laser parameters

The samples array generated using Taguchi method was rearranged as shown in Table 4.5 and the scanning path used to develop the FeCrMoCB MG layer is shown in Figure 4.20.

Table 4.5: Experimental array used to optimize the laser cladding parameters

Sample	E_s, J/mm^2	d (hxw), mm	*c, mm*	*OL*, %	*v*, mm/s
S1	6.25	4x4	6.0	50	20
S2		4x6	9.9	35	20
S3		4x8	14.0	25	20
S4	5.00	4x4	6.6	35	25
S5		4x6	10.5	25	25
S6		4x8	12.0	50	25
S7	4.17	4x4	7.0	25	30
S8		4x6	9.0	50	30
S9		4x8	13.2	35	30

4.4.1. Material characterization

Figure 4.21 shows the XRD of the coated samples. As can be seen in Figure 4.21, although all samples exhibited amorphous structure within CL, different phases are recognized such as intermetallic compounds – B_6Fe_{23} and Fe_3C – which are hard and brittle, besides metallic phases as Fe, Fe-Mo and Cr. These phases comply with the phases reported by Guo et. al (Guo & Su, 2017).

It is recognized from the XRD analysis that the amorphous content varies according the applied E_s. This can be explained with the fact of that the E_s denotes the total transmitted

heat to the molten pool affecting its temperature. The increase of E_s would increase the temperature, and hence prolong the cooling time allowing crystalline phases to form and decrease the amorphous content, Table 4.7. It is also worthy to mention that increasing the *OL%* would have the same effect as increasing the *ED* due to the accumulation of heat along the specimen. On the other hand, the spot size has an inverse effect as the increase of the spot size (*w*: width size) would decrease the OL% and hence decrease the total accumulated heat.

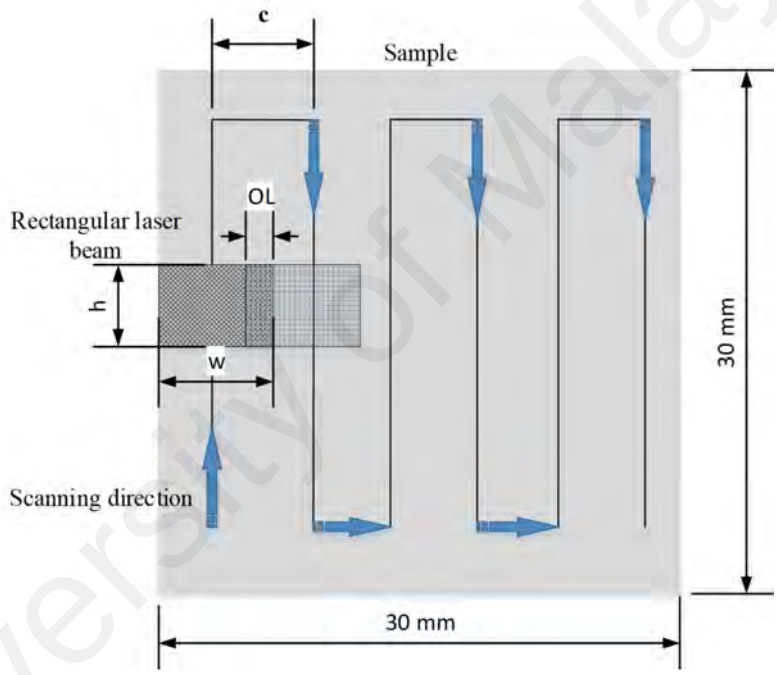

Figure 4.20: Scanning path to develop FeCrMoCB MG layer

Table 4.6: Amorphous content percentage induced within CL of the fabricated samples

Sample	S1	S2	S3	S4	S5	S6	S7	S8	S9
E_s, J/mm^2	6.25			5.00			4.17		
Amorphous content %	76.5	77.2	78.4	78.9	79.4	78.4	79.4	80.7	81.9
Average amorphous content %	77.4±0.9			78.9±0.5			80.6±1.3		

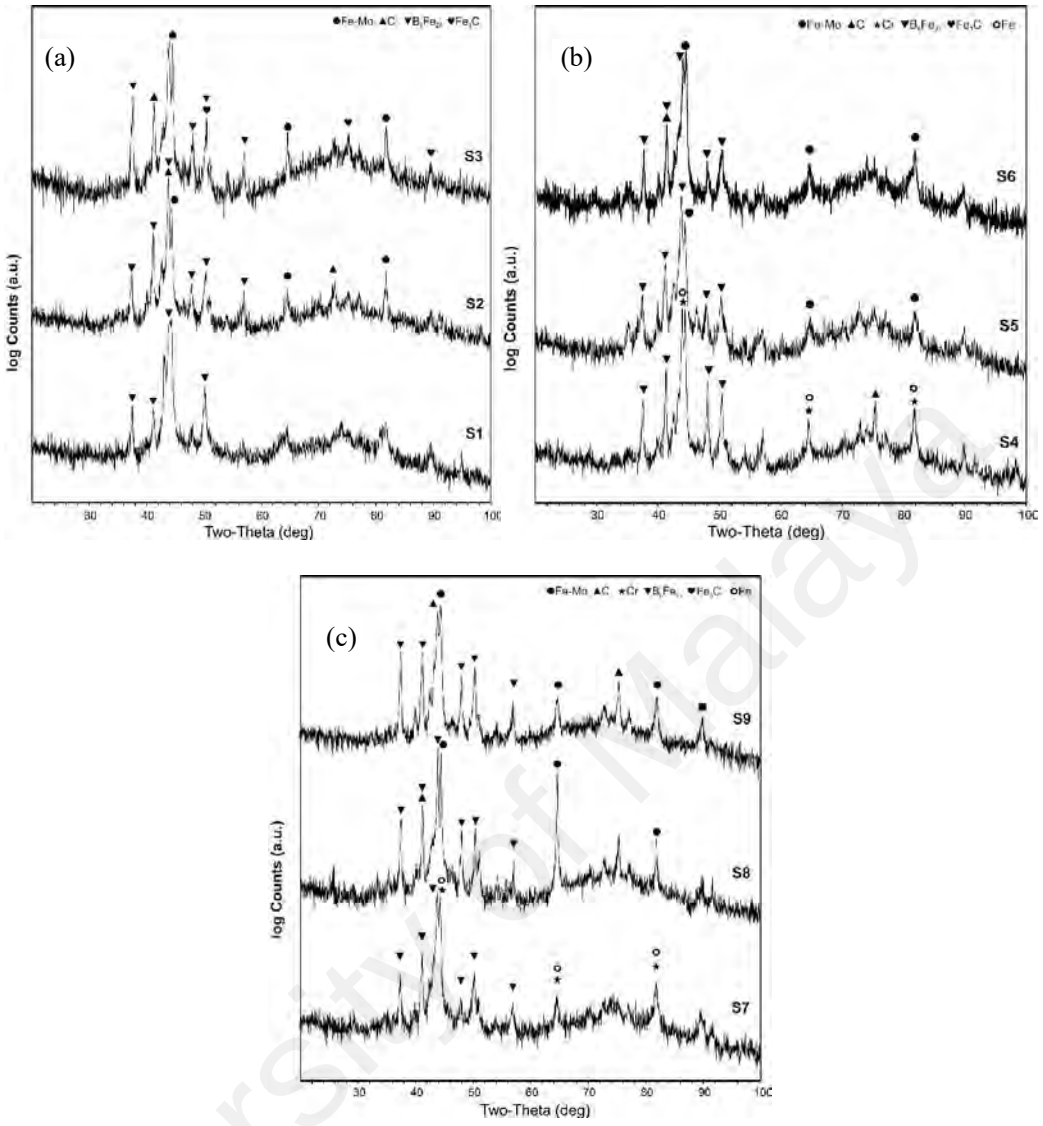

Figure 4.21: XRD pattern of the coated samples (a) samples S1, S2, S3, (b) samples S4, S5, S6, (c) samples S7, S8, S9

The hard phases recognized are featured with high wear resistance and stability, however, they are brittle (low fracture toughness) (Bell & Richards, 1987; Weber et al., 1995). On the contrary, the crystalline phases as Fe and Cr have lower hardness, but with higher ductility. According to this context and as the wear resistance of MGs is affected by the hardness, ductility, and the fracture toughness, the balance of hard phases and ductile phases within the amorphous structure would improve the fracture toughness and hence, the wear resistance (Guo & Su, 2017).

Figure 4.22 shows the microstructure images obtained within the CL. The imaging revealed the existence of micro and nano-sized crystalline phases embedded in the amorphous structure (appeared as plain grey background). As reported before, the amorphous structure, in addition, the existence of Fe-Mo beside the hard phases would enhance the wear behavior although the hardness value maybe degrades. It is reported that the composite structure – amorphous and crystalline, specially nano-sized crystalline structure – proved better fracture toughness which in turn affect the wear resistance property (Guo & Su, 2017; X. Liang et al., 2017).

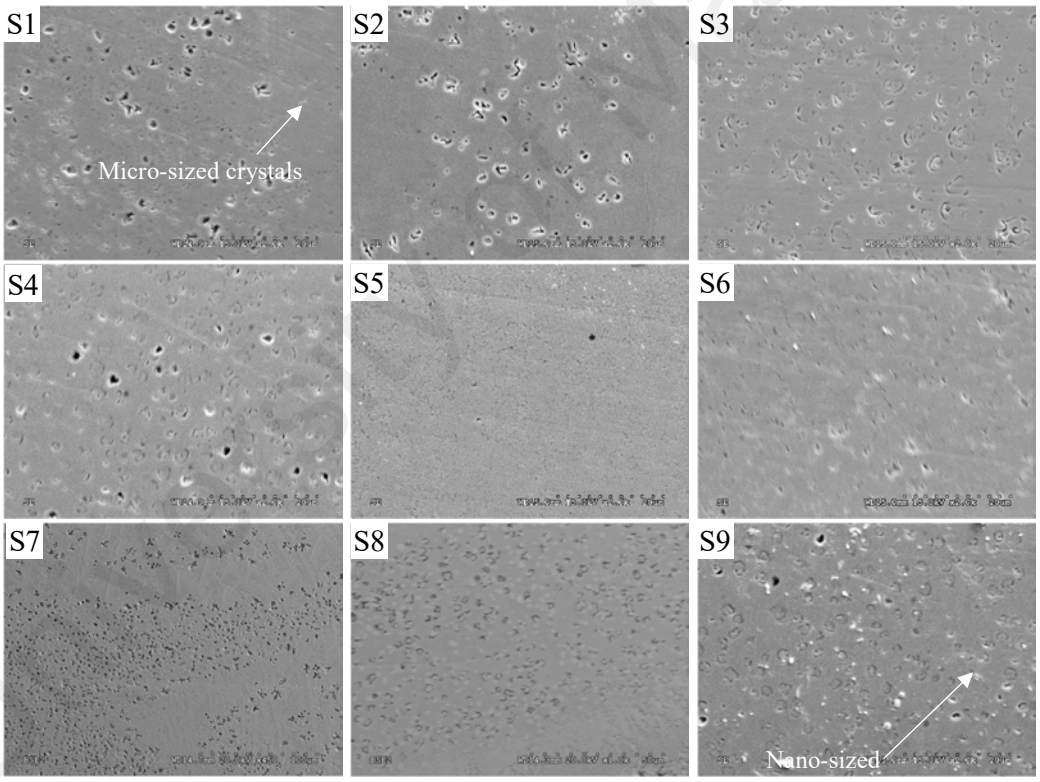

Figure 4.22: SEM image of microstructure obtained within the CL

It is also found that the decrease of E_s resulted in refining the crystal structure and the nano-sized crystals became dominant (Zhu et al., 2013). On the other side, the increase of *OL* leads to accumulating heating between adjacent tracks resulting in micro-sized

crystals and the reduction of the amorphous content (Li, Roberts, O'Keeffe, & Sercombe, 2016).

4.4.2. Micro-Hardness measurements

The average values of the surface micro-hardness are shown in Figure 4.23. The hardness value of the FeCrMoCB MG coating showed variation from 1100 to 1415 HV0.1. Generally, the hardness of the MG is affected by the amorphous content and the phase transformation. The metallic phases are usually ductile and exhibit low hardness value, while the intermetallic compounds are brittle and hard. So, increasing the amorphous content and the intermetallic compounds would enhance the hardness value, while the metallic phases would degrade the hardness. Since the difference in amorphous content is not significant, the intermetallic compounds would have the major effect on the hardness value (Ibrahim et al., 2019, 2018).

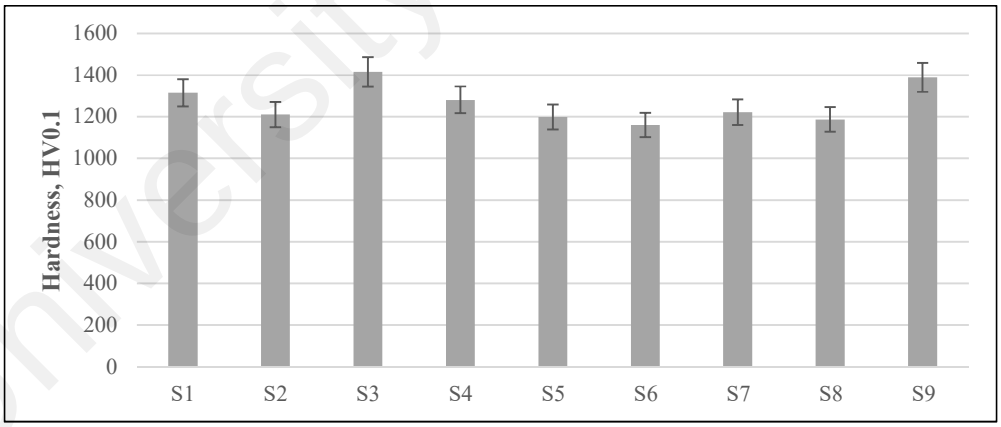

Figure 4.23: Surface micro-hardness average values

Although the samples S7, S8, S9 showed higher amorphous content than S4, S5, S6 and S1, S2, S3, the hardness value did not show a significant variation. This can be understood based on that the hardness of the fabricated samples is affected by amorphous content and

the type of phases exited within the coating layer. Normally, the higher cooling rates result in higher amorphous content and vice versa. Simultaneously, the metallic phases will form at higher cooling rate, while the intermetallic compounds will form at lower cooling rates (Ibrahim et al., 2018; Lu et al., 2018). Thus, lower amorphous content will induce higher content of intermetallic compound compensating the hardness drop caused by the crystalline phase.

4.4.3. Electrochemical corrosion test

The polarization curve resulted from the linear sweep voltammetry is presented in Figure 4.24, where the horizontal axis represents the potential against the RE and modified to the saturated Hydrogen electrode (SHE) and the vertical axis is the current density in logarithmic scale.

By analyzing the obtained Tafel plot, the corrosion potential and corrosion current, besides the corrosion rate are listed in Table 4.7 and a comparison between the tested samples are shown in Figure 4.25. It is clear from the analysis that FeCrMoCB MG has better corrosion resistance than Cronidur30. This effect is referred to the amorphous structure where no crystalline defects existed as grain boundaries which acts as weak points where the corrosion is initiated. However, the existence of crystalline pure metallics as Fe and Cr within the amorphous structure contribute in the degradation of the corrosion resistance of FeCrMoCB MG.

Table 4.7: corrosion potential, corrosion current and corresponding corrosion rate of tested samples

Sample	CR30	S1	S2	S3	S4	S5	S6	S7	S8	S9
E_{corr}, V	-0.809	-0.916	-0.700	-0.880	-0.876	-0.898	-0.834	-0.806	-0.795	-0.803
I_{corr}, A/cm^2	1.13E-05	1.34E-06	1.13E-05	1.28E-05	1.19E-05	6.28E-06	2.21E-05	1.26E-05	2.39E-05	2.20E-05
CR, mm/year	2.65E-04	1.08E-05	9.14E-05	1.03E-04	9.56E-05	5.06E-05	1.79E-04	1.02E-04	1.93E-04	1.77E-04

**CR30 is denoted for Cronidur30*

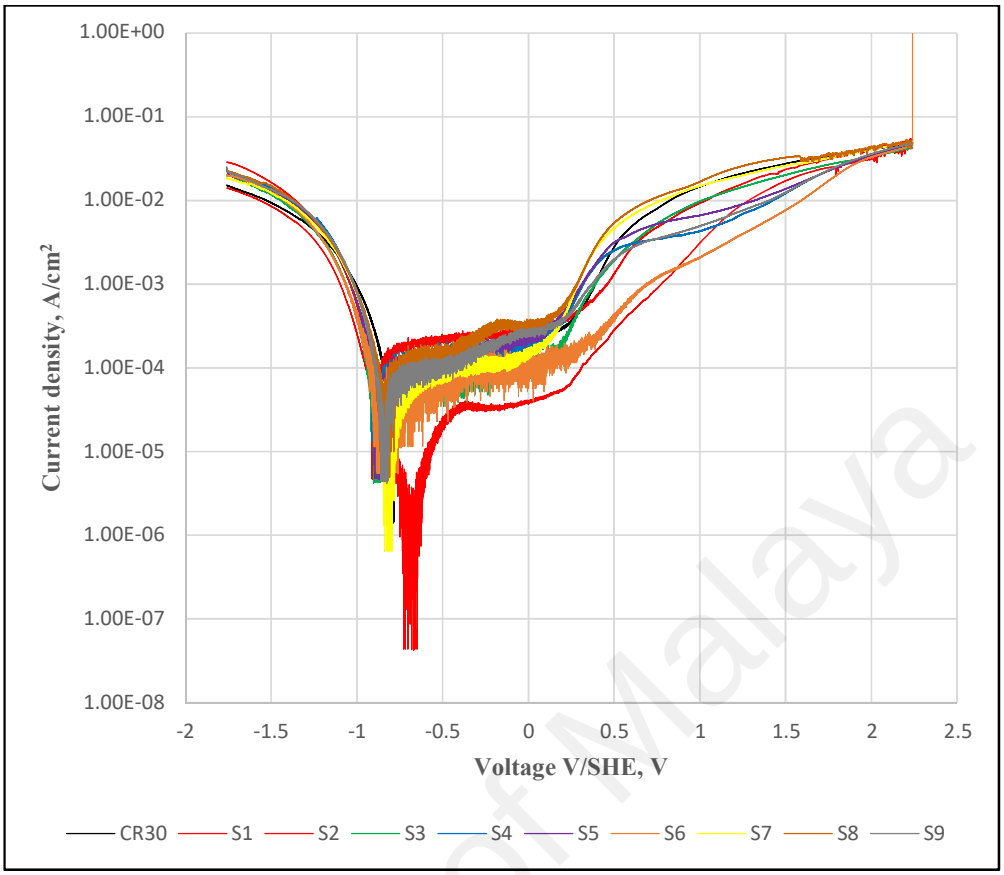

Figure 4.24: Tafel plot of the linear sweep voltammetry

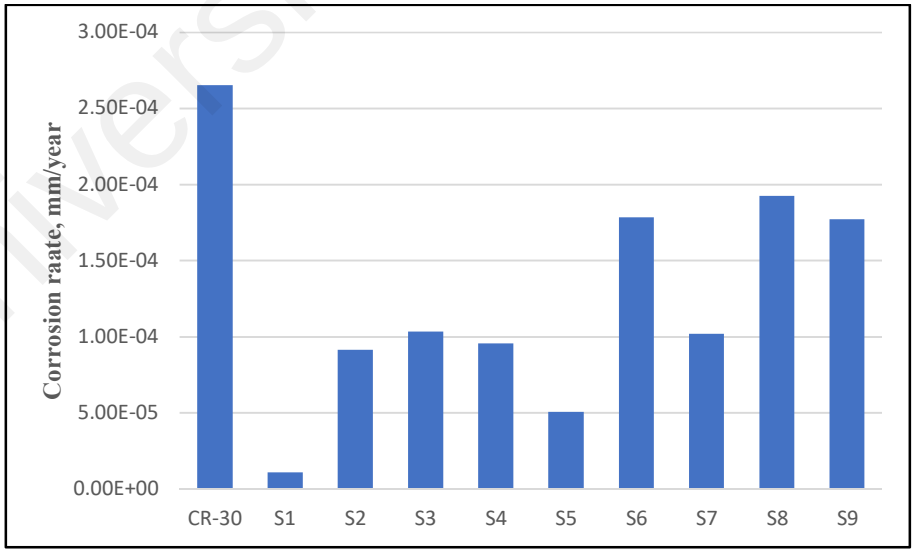

Figure 4.25: Corrosion rate of the tested samples

Normally, the higher amorphous phase would induce higher corrosion resistance due to the absence of crystalline structure defects. However, from the results it has been noticed that the type of crystalline phases affects the corrosion resistance. As mentioned above, the pure metallic phases degrade the corrosion resistance and increase the corrosion rate, while the intermetallic compounds existed within the amorphous structure – which are chemically stable – helped in improving the corrosion resistance.

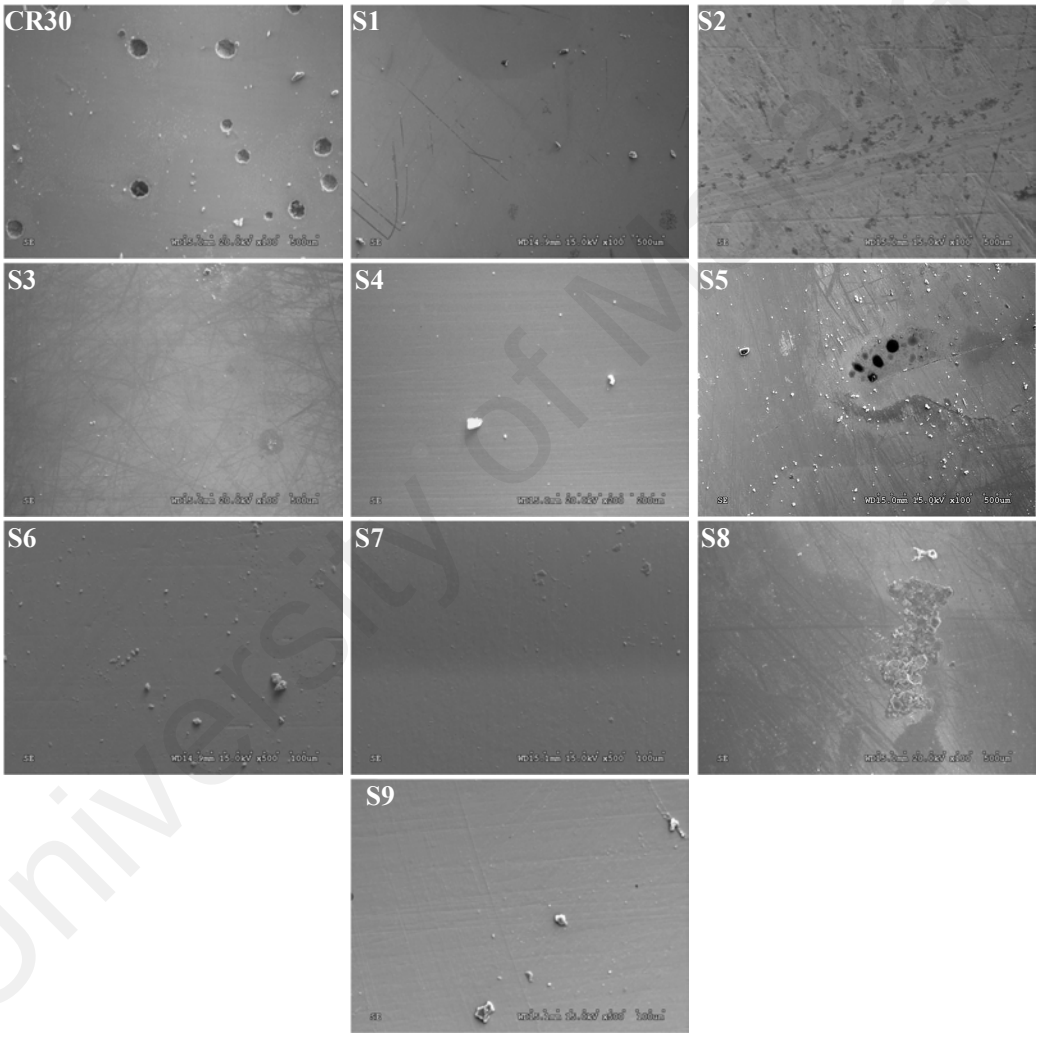

Figure 4.26: Morphology of the samples after electrochemical corrosion test

SEM images of the corroded samples morphology were taken for further investigation. The morphology of the Cronidur30 showed clear pitting corrosion while the FeCrMoCB

MG had a smooth and clean surface with some deposits of particles resulted from the corrosion process.

4.4.4. Wear testing and nanoindentation measurement

4.4.4.1. Dry wear testing

Figure 4.27 shows the wear rate values of the FeCrMoCB MG cladding compared to the uncoated stainless steel. The wear rate of cladded samples was very low compared to the uncoated substrate. Samples S1 and S3 showed the highest wear rate within the fabricated samples, while samples S5 and S8 showed the lowest wear rate as shown in Figure 4.27. From literature (Liao, Hua, Chen, Huang, & Zhang, 2017; Rahaman, Zhang, & Ruan, 2013), it is reported that the wear resistance of MG is not directly proportional to the hardness unlike metallic alloys because the metallic alloys exhibit strain hardening during the wear resulting in increasing the hardness and the wear resistance, while MGs are brittle and does not exhibit strain hardening. So, it is found that the increase in amorphous content would increase the brittleness and hence reduce the wear resistance. As long as the differences in amorphous content is insignificant, the recognized phases as well as the microstructure would have the major effect on the wear resistance. The intermetallic compounds and fine microstructure enhance the wear properties, however, the existence of metallic phases as Fe-Mo, Cr and Fe will improve the ductility and hence the wear resistance.

The SEM imaging of the wear scars is shown in Figure 4.28. It is found that wear marks existed on all samples. These marks indicate that the removal of wear debris caused by brittle fracture which is usually found in MG. Traverse cracks are noticed in S9 where the highest amorphous content, which means the most brittle CL causing a failure in toughness during the wear test (Segu, Choi, Yi, & Kim, 2012). The other samples did not

show cracks because of the composite crystalline-amorphous structure which imposes less brittleness.

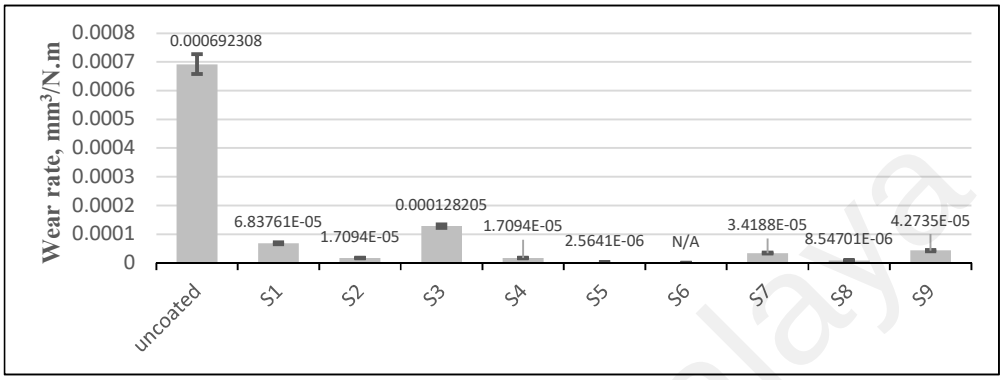

Figure 4.27: Wear rate of Fe-based MG coating and uncoated SS

The surface roughness average values of each wear scar are shown in Table 4.8 and the corresponding 3D profile in Figure 4.29. From the average values of R_a, it is noticed that high E_s (6.25 J/mm^2) induced the least R_a values and low E_s (5.00 J/mm^2) induced the highest R_a values while the R_a values induced by the medium E_s (4.17 J/mm^2) lied in between. This can be described as the R_a value has a direct relation to the amorphous content and the formed phases within the CL which affect the wear mechanism. The amorphous structure exhibits sliding wear, while ductile phase exhibits adhesion wear. Thus, the mixed amorphous-crystalline structure resulted in a combination of sliding wear and adhesion wear. However, it is found that cracks appeared in higher amorphous contents which facilitate the fracture and releases of debris which may increase the surface roughness of the wear scars. These findings showed that the increase of spot size and overlap would result in increasing the R_a values as they affect the amorphous content and formed phases within the CL as discussed previously.

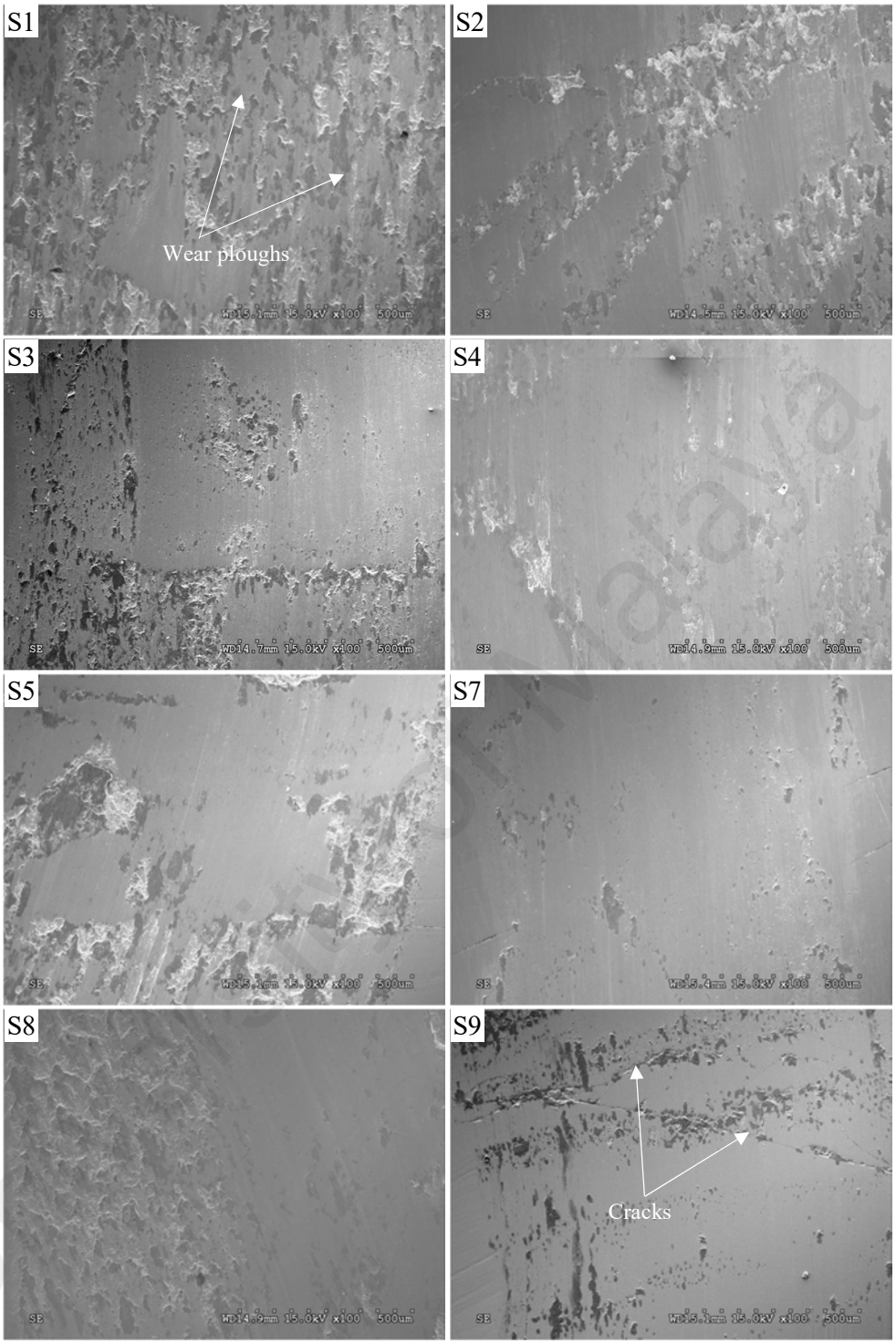

Figure 4.28: SEM images for the wear scars on the surface of FeCrMoCB MG coatings

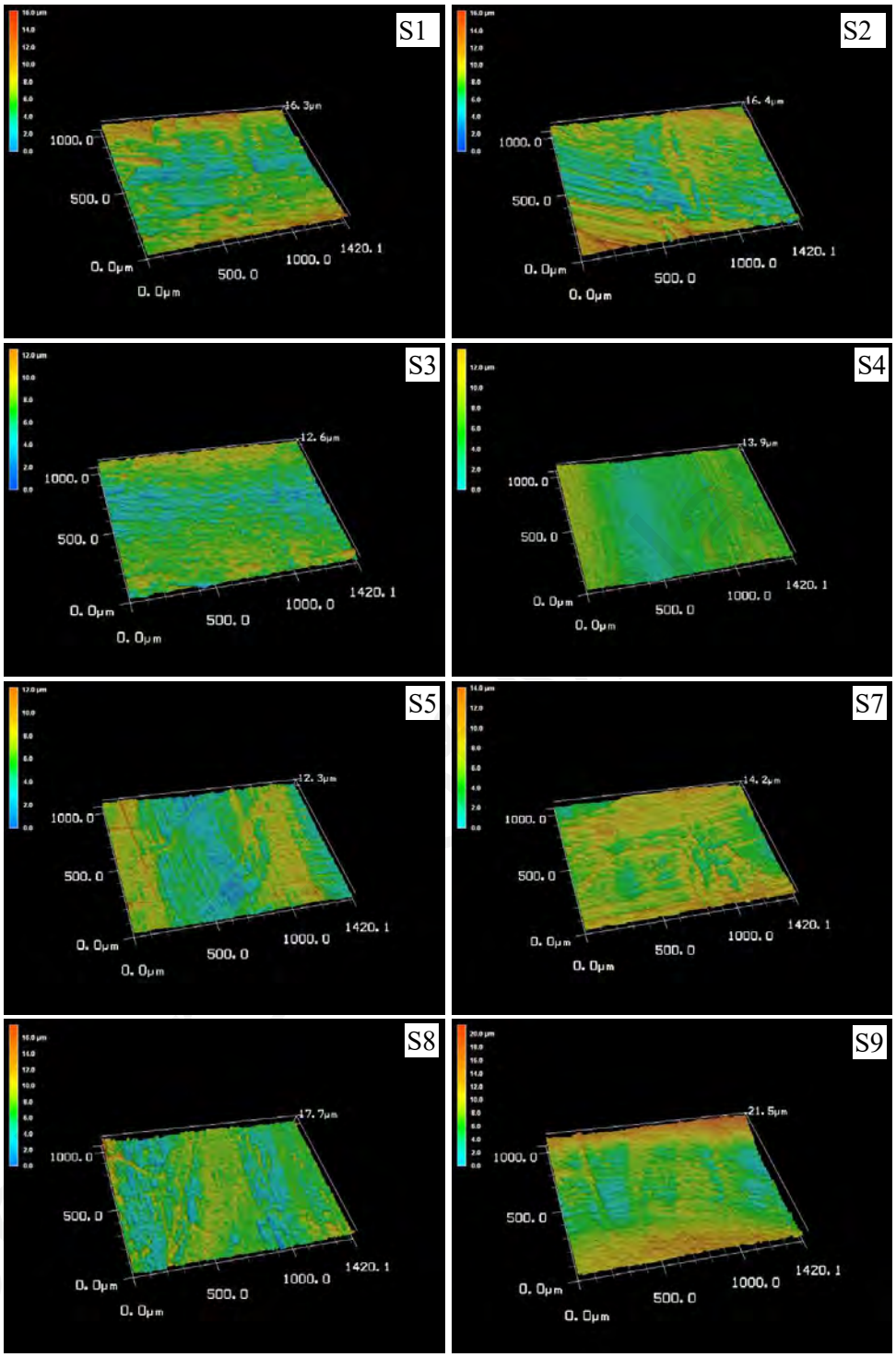

Figure 4.29: 3D profile of the surface roughness measured at wear scars

Table 4.8: Average surface roughness (R_a) values taken at the wear scar

Sample	Uncoated	S1	S2	S3	S4	S5	S6	S7	S8	S9
R_a	2.583	1.205	1.627	1.9215	1.615	1.758	N/A	1.831	2.234	2.1905

4.4.4.2. Wear testing in Simulated Body Fluid

Table 4.9 shows the wear test results of R1, R2, R3 (representing S2, S5 and S7 respectively) and the uncoated substrate, the wear rate (W_r) of the uncoated substrate was enhanced significantly after the laser cladding of FeCrMoCB glassy amorphous-crystalline MG CL. The *Wr* of the uncoated substrate was about 4 times higher than the MG layer. The *Wr* of FeCrMoCB-MG in SBF (1.54x10-5 mm3/N.m) was found to be significantly lower than the exhibited *Wr* of other common MGs and biomaterials; Zr-based MG (2.5x10−4 mm3/N.m), Ti6Al4V (5.5x10−4 mm3/N.m), 316L SS (7x10−5 mm3/N.m), and CoCrMo alloy (5x10−5 mm3/N.m) in SBF (Wang, Shi, Duan, Li, & Xu, 2014), and even lower than those exhibited by Fe-based MG in a dry environment (2.11x10−5 mm3/N.m) (Lu et al., 2018). The enhanced wear resistance of FeCrMoCB-MG in SBF is referred to the high hardness and excellent mechanical properties as strength, the excellent corrosion resistance and the formation of a stable and strong passive layer, besides, the SBF served as a lubricant between the CL and the counterpart.

Table 4.9: Wear test results of R1, R2, R3 and uncoated substrate

Sample	Uncoated substrate	R1	R2	R3
W_r, mm^3/N.m	$8.21x10^{-5}$	$1.54x10^{-5}$	$1.88x10^{-5}$	$3.08x10^{-5}$
Average coefficient of friction	0.634	0.140	0.185	0.226
Wear scar R_a, µm	3.418±1.059	0.468±0.062	0.604±0.354	0.743±0.248

Figure 4.30 and 4.31 shows the SEM image of the wear scar and the corresponding EDS. The SEM shows a smooth worn surface confirming smooth sliding wear. However, The EDS revealed traces of Al in all worn surfaces indicating adhesion wear between the MG layer and the alumina counterpart. Hence the wear mechanism is a combination of sliding and adhesion wear behavior. In addition, recognizable traverse cracks appeared in R2 and

R3. These cracks indicate brittleness induced at higher AP, while the uncoated substrate exhibited abraded surface.

It is found that Cl appeared in all samples besides Na in (R1) and (R2), and Ca in (R3) which refers to a deposition of SBF compounds on the worn-out surface. It is notable that Cr, O, Fe and Mo intensities are higher in R1 compared to R2 and R3. This can be attributed to the formation of a passive layer of chromium oxide at the surface beside corrosion particles of iron and molybdenum chlorides. This passive layer is much stronger in R1 than R2 and R3 resulting in lower W_r in R1.

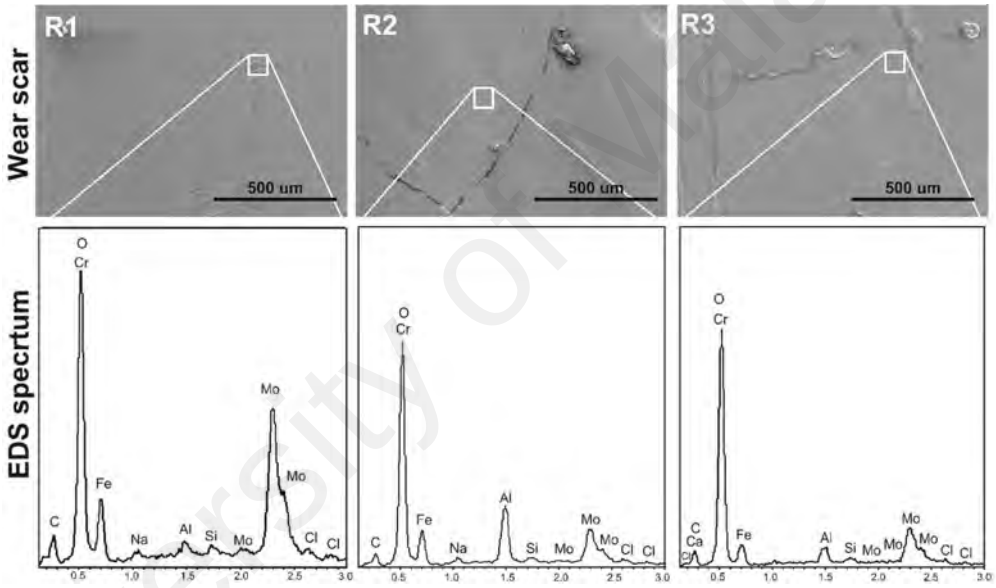

Figure 4.30: SEM image of wear scars and EDS spectrum of R1, R2 and R3

It is observed that the average coefficient of friction (*COF*) and the wear scar roughness (R_a) increased with increasing amorphous phase and decreasing E_s. The increase of the average coefficient of friction ($COF_{R1}<COF_{R2}<COF_{R3}$) with the increase of W_r indicates the increase of contact area and is attributed to the successive formation and breakage of the passive layer during the wear test.

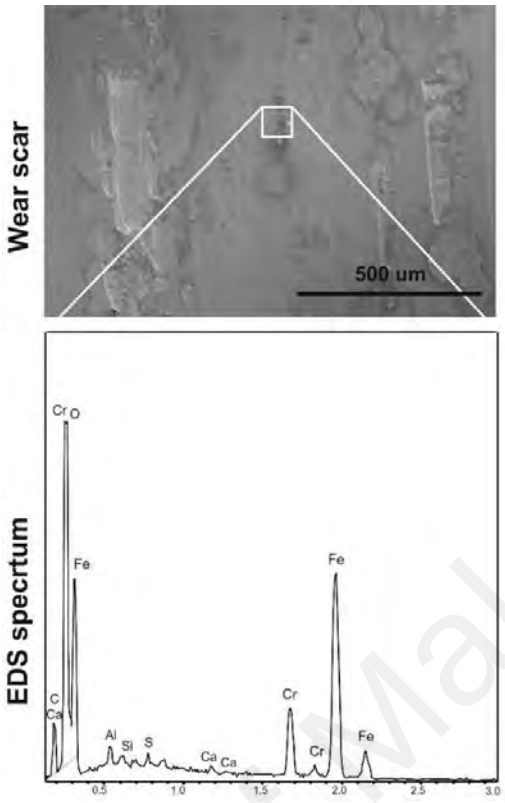

Figure 4.31: SEM image of wear scars and EDS spectrum of uncoated substrate

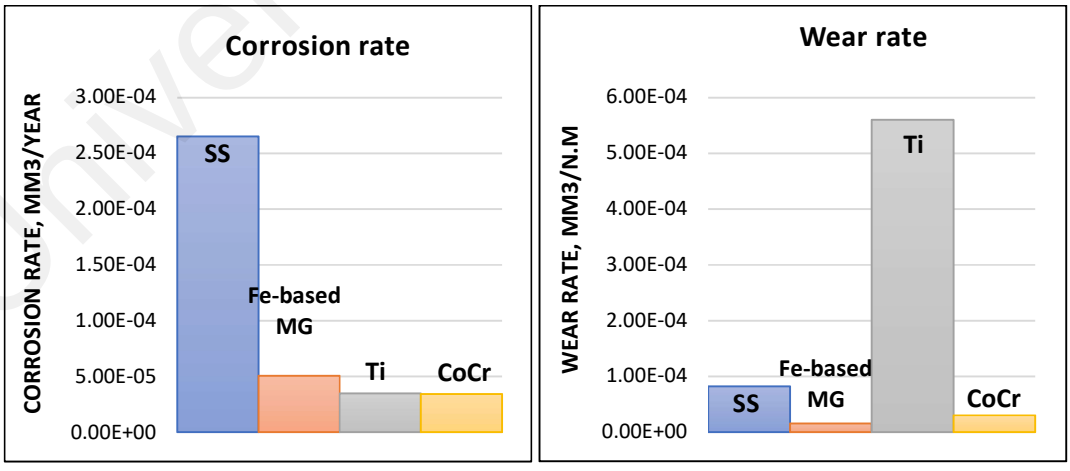

Figure 4.32: Corrosion and wear rate of FeCrMoCB MG coating layer compared to the popular metallic biomaterials

Figure 4.32 shows that the proposed FeCrMoCB MG has a comparable tribological properties and corrosion resistance to the popular metallic biomaterials, even it shows better wear rate in PBS. The presented comparison is using the values obtained in this study and the results presented by N. Hua et al. (Hua et al., 2015). However, it is important to perform the wear and the electrochemical corrosion tests for the presented materials in the same conditions and using the same testing apparatus.

4.4.4.3. Nanoindentation measurement

Table 4.10 lists the nano-indentation measurement results. The hardness measurements are consistent with the micro-hardness measurement and showed a significant increase in the hardness of the FeCrMoCB MG compared with the uncoated substrate and compared to other studied MGs (800 to 1000 HV0.1) (Segu et al., 2012; Wu & Hong, 2001). Normally, the hardness of MG is increased with increasing AP, but the existence of MP degrades the hardness while the existence of IMC enhances it. This can explain the close values of the hardness of R1, R2 and R3.

Table 4.10: Nano-indentation measurement results

Sample	Uncoated substrate	R1	R2	R3
Average hardness, GPa	2.72±1.00	14.97±1.20	15.47±0.70	14.77±1.09
Young's Modulus, GPa	218.0±2.4	296.7±6.2	287.5±4.1	285±3.4

On the other hand, Young's modulus of FeCrMoCB MG was higher than that of the uncoated substrate and showed inversely proportional with the AP. It is found that there is a slight increase in Young's modulus with the decrease of the AP and the increase of the MP increases the ductility and hence increases Young's modulus. These results can

explain the direct proportional of the W_r with AP as the higher Young's modulus will decrease the contact area between the surface and the counterpart according to the Hertz contact theory (Hertz, Reine, & Angew, 1881).

Finally, according to the previous investigations, optimized laser cladding parameters were set according to Table 4.11. Further FeCrMoCB MG samples were fabricated and investigated to ensure the different properties.

Table 4.11: optimized laser cladding parameters

Parameter	Power, W	Scanning speed, mm/s	Spot size	OL%
Optimized sample (A)	3000	25	6x4	25%

4.5. Optimized FeCrMoCB MG coating layer

Further investigations have been performed on the optimized coating layer; 30 days immersion-corrosion test in PBS, wettability test, in-vitro bioactivity and in-vitro cytocompatibility.

4.5.1. 30 days immersion-corrosion test

The corrosion potential and corrosion current besides the corrosion rate during 30 days are showed in Table 4.12. Figure 4.33 compares the corrosion rates of FeCrMoCB MG coating and Cronidur30. The results showed a superior corrosion resistance of FeCrMoCB MG compared to Cronidur30 during the 30 days immersion-corrosion test. Also, the corrosion resistance of FeCrMoCB MG was stable until day 22 where FeCrMoCB MG exhibited a dramatical increase in the corrosion rate, then decayed until day 30. On the other side, the uncoated substrate experienced an increase in the corrosion

rate in the first 9 days, then decreased until day 22 to reach the minimum corrosion rate. Unlike the MG coating, Cronidur30 exhibited an increase in corrosion rate to reach the peak in day 25 and decrease again in the day 30. Further SEM and EDS analysis are provided in to understand this phenomenon.

As can be seen in Figure 4.34, the morphology of corroded coating layer in the first 9 days revealed increasing of corrosion rate as the corrosion deposits increased – P and Na was deposited on the surface. In day 12, the morphology had a smooth and clean surface – a passive layer has formed referred to chromium oxide - and minor corrosion particles appeared indicating lower corrosion rate, Figure 4.33. In the next days 16, 19 and 22, the corrosion rate is increased – Cl ions appeared in EDS spectra which has compounds with Fe, besides pitting started to appear on the morphology. Finally, a strong passive layer is formed, besides intensive deposits of Na and P compounds coming from the PBS which protects the coating layer from further corrosion.

Table 4.12: 30 days immersion test results of the optimized FeCrMoCB MG and Cronidur30

	FeCrMoCB MG			**Cronidur30**		
Days	**E_{corr}, V**	**I_{corr}, A/cm^2**	**CR, mm^3/year**	**E_{corr}, V**	**I_{corr}, A/cm^2**	**CR, mm^3/year**
3 days	-0.851	5.34E-06	3.76E-05	-0.809	9.79E-06	2.26E-04
5 days	-0.846	3.11E-06	2.18E-05	-0.841	3.02E-05	6.99E-04
9 days	-0.770	8.35E-06	5.98E-05	-0.862	3.93E-05	9.09E-04
12 days	-0.794	1.98E-06	1.42E-05	-0.806	1.57E-05	3.65E-04
16 days	-0.762	6.38E-06	4.57E-05	-0.762	2.76E-06	6.39E-05
19 days	-0.763	2.22E-06	1.59E-05	-0.821	1.44E-06	3.34E-05
22 days	-0.737	2.02E-05	1.45E-04	-0.836	2.25E-05	5.22E-04
25 days	-0.892	9.69E-06	6.94E-05	-0.865	7.13E-05	1.65E-03
30 days	-0.816	5.81E-06	4.16E-05	-0.889	1.81E-05	4.20E-04

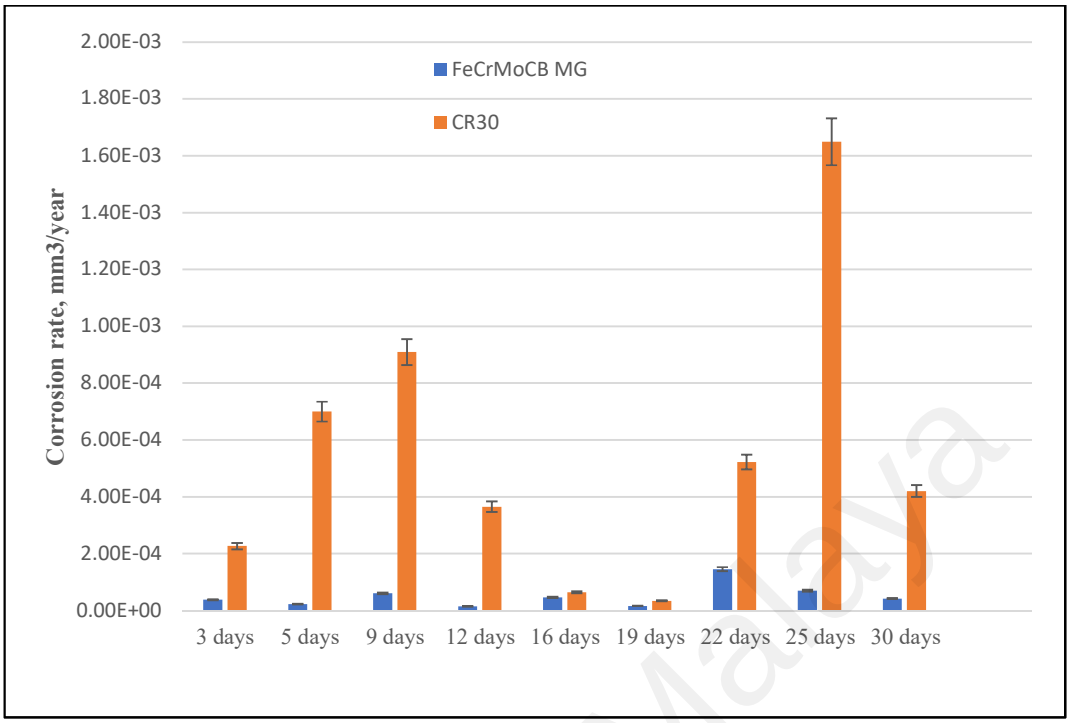

Figure 4.33: Comparison between the corrosion rate values of FeCrMoCB MG and Cronidur30 during 30 days immersion test

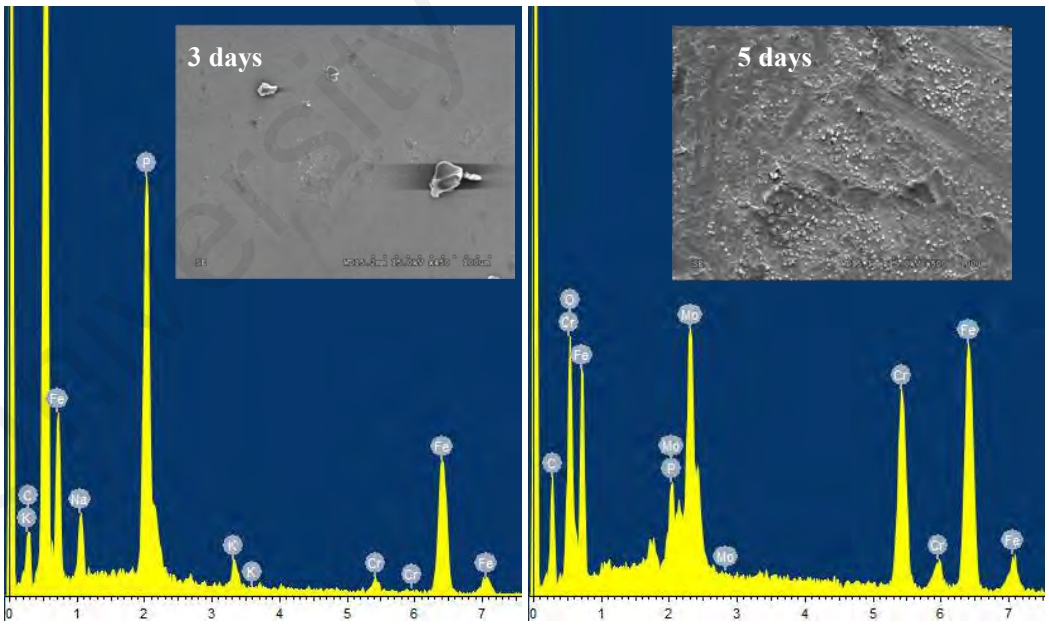

Figure 4.34: SEM images and EDS spectra of FeCrMoCB MG after the immersion-corrosion test

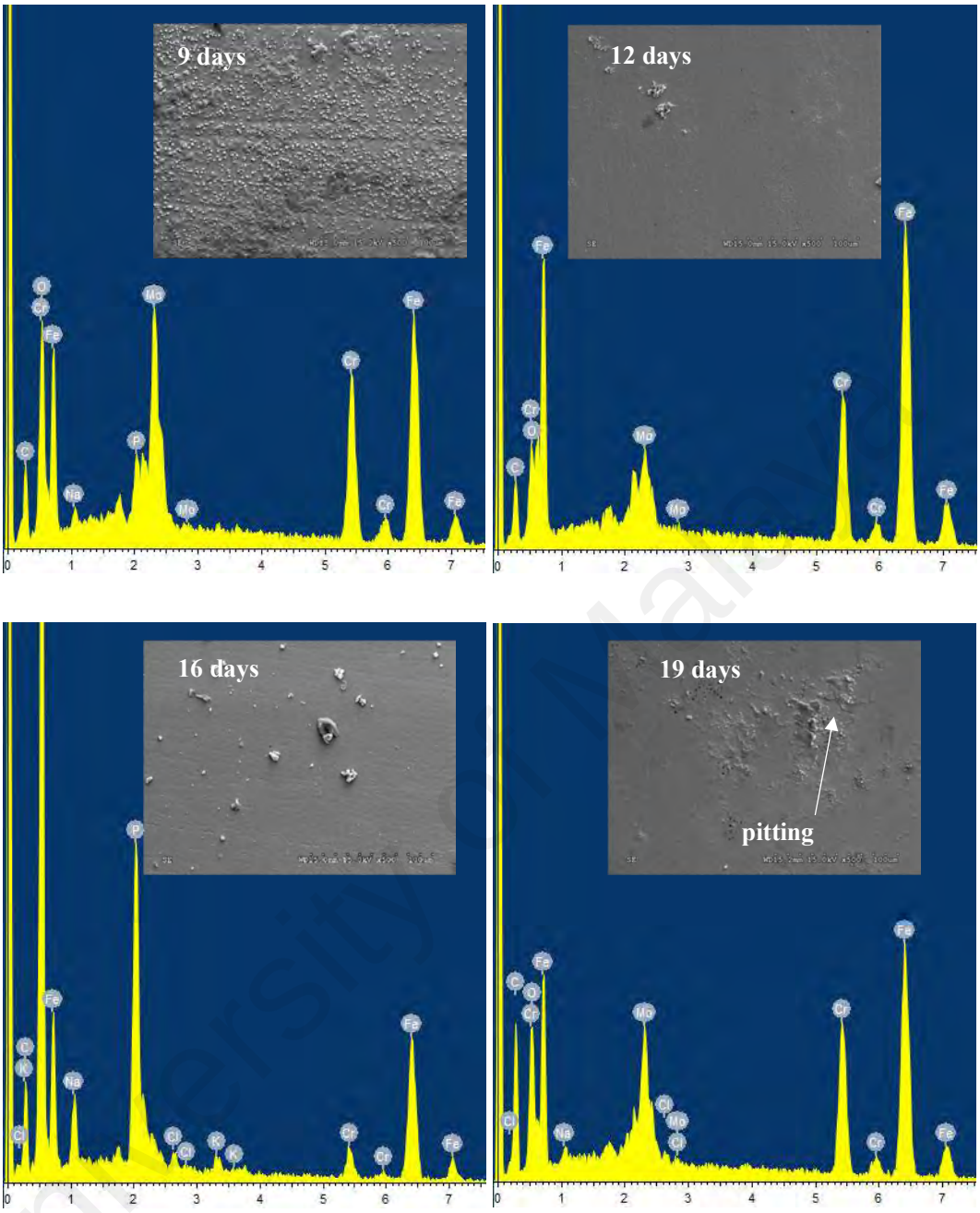

Cont. Figure 4.34

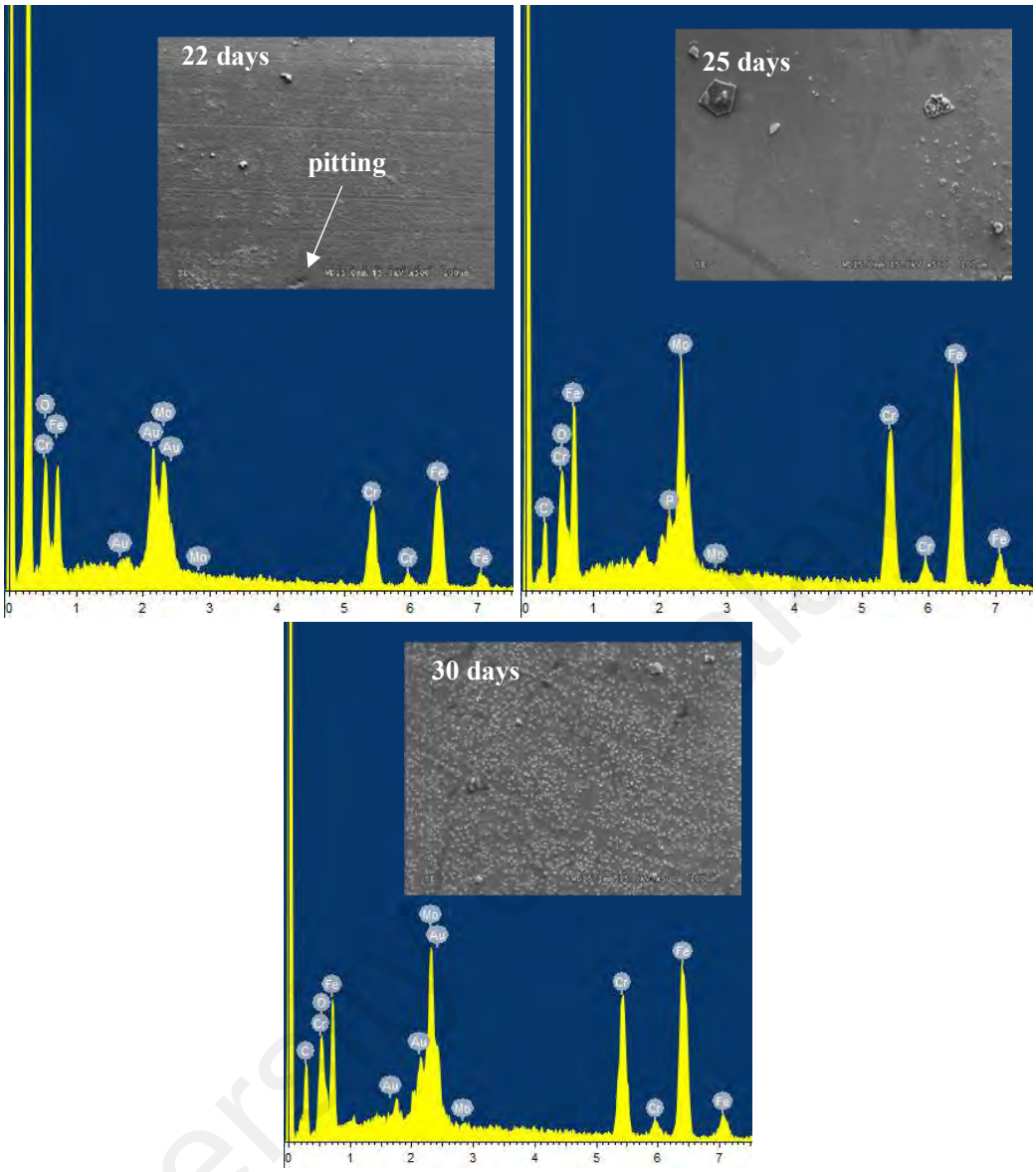

Cont. Figure 4.34

On the other side, Cronidur30 showed pitting corrosion from day 3, Figure 4.35. In day 16, chromium oxide passive layer became stronger and the corrosion rate was dropped dramatically. However, further immersion caused breaking the passive layer and the pitting corrosion was increased as shown in day 30, Figure 4.35.

The immersion test revealed the stability of the corrosion resistance of the FeCrMoCB MG during 30 days of immersion in PBS. This is referred to the ability of the MG to form and reform a stable and strong passive besides the deposition of Na and P particle forming

a protective layer. The pitting corrosion is started after 22 days of immersion, however, the corrosion rate and pitting corrosion still superior to the uncoated substrate.

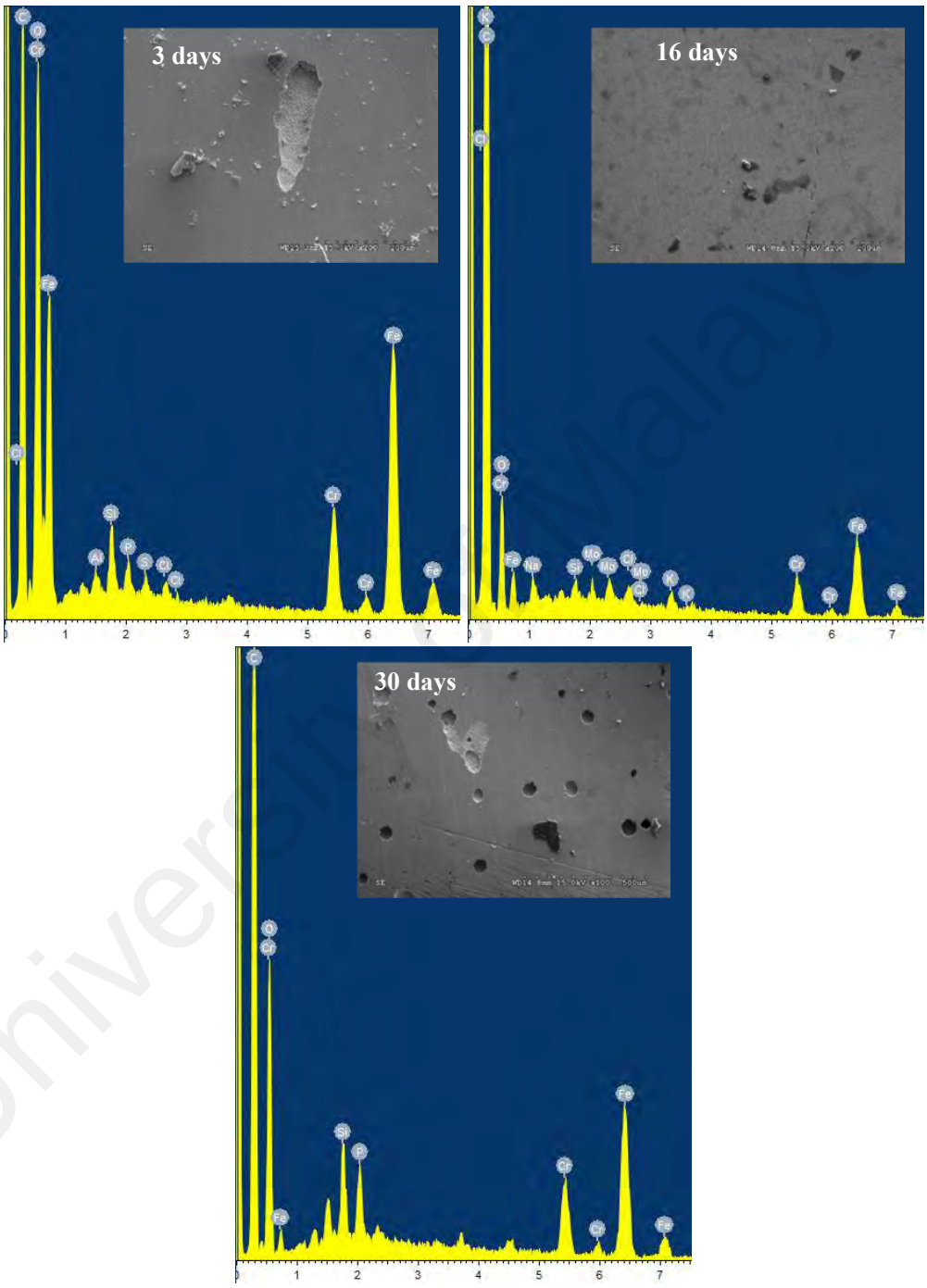

Figure 4.35: SEM imaging and EDS spectra of Cronidur30 after the immersion-corrosion test

4.5.2. Wettability test

The average contact angle of coated samples and uncoated substrate are listed in Table 4.13. The results showed that the FeCrMoCB MG exhibited better wettability than the uncoated substrate which indicates to have better cell adhesion (Ma et al., 2012; Sola, Bellucci, & Cannillo, 2016). This result predicts better cell adhesion and bioactivity of the FeCrMoCB MG.

Table 4.13: Contact angle for the coated samples and uncoated substrate

Sample	Uncoated	FeCrMoCB MG
Average contact angle	95.24	87.87

4.5.3. In-vitro bioactivity test

Figure 4.36 shows the SEM images and the corresponding EDS spectra of the apatite layer formed on the surface of the FeCrMoCB CL. It can be observed that the apatite layer starts to nucleate on the first day and rapidly grows to cover the complete surface in 21 days. The EDS analysis showed that at 1 and 3 days of soaking, P and Ca are present but the Ca/P ratio was below 1. However, after 7 days, Ca/P ratio increased to 1.25 and after 21 days became 1.61 approaching the stoichiometric ratio of apatite. After 21 days, a new layer of apatite started to form on the top of the existed apatite layer.

This could be described as a promising intermediate bioactive materials where Fe-based MG exhibit bioactivity by forming Fe-OH groups which help the apatite formation and growth (Qin et al., 2016). Moreover, the B can enhance the bioactivity as it is known to be beneficial for healthy and growing bones (Balasubramanian, Büttner, Miguez Pacheco, & Boccaccini, 2018; Hakki et al., 2013). An interesting question that can be raised here is why does a change in the phase of Fe from crystalline to amorphous result in dramatically improved bioactivity? Since amorphous Fe does not exhibit any long-range

atomic order and acts as a frozen liquid, the surface energy is higher and completely isotropic as compared to the energetically stable phases observed when Fe is chemically bound in an ordered crystalline lattice. This elevated free energy of amorphous Fe promotes formation of Fe-OH bonds that serve as nucleation sites for Ca^{+2} and PO_4^{-2} ions to grow into apatite. Also, the good wettability properties of FeCrMoCB MG would enhance the formation and growth of apatite layer. These results reveal the good bioactivity of the proposed FeCrMoCB CL and highlight its outstanding potential for bone-implant applications.

Table 4.14: absorbance values at 570 nm of the MTT assay for tested samples

Day 1				Day 3				Day 7			
A	**CR30**	**Control**	**Blank**	**A**	**CR30**	**Control**	**Blank**	**A**	**CR30**	**Control**	**Blank**
0.106	0.079	0.107	0.06	0.611	0.259	0.422	0.059	1.413	1.595	2.254	0.064
0.116	0.078	0.11	0.06	0.364	0.345	0.386	0.062	0.727	1.557	2.204	0.063
0.106	0.081	0.106	0.059	0.436	0.347	0.4	0.06	1.673	1.655	2.251	0.062
1.063	0.096	0.102	0.059	0.358	0.311	0.411	0.062	0.122	1.745	2.32	0.061
0.119	0.08	0.103	0.059	0.311	0.349	0.409	0.056	1.659	1.882	2.149	0.061

4.5.4. In-vitro cytocompatibility

The MTT assay results of 7 days cell-culture are listed in Table 4.14. The highlighted values are eliminated from the average data as it exhibited large error. A is referred to FeCrMoCB MG coating sample, CR30 is the uncoated substrate, control is the negative sample and blank is the no-sample no-cell sample.

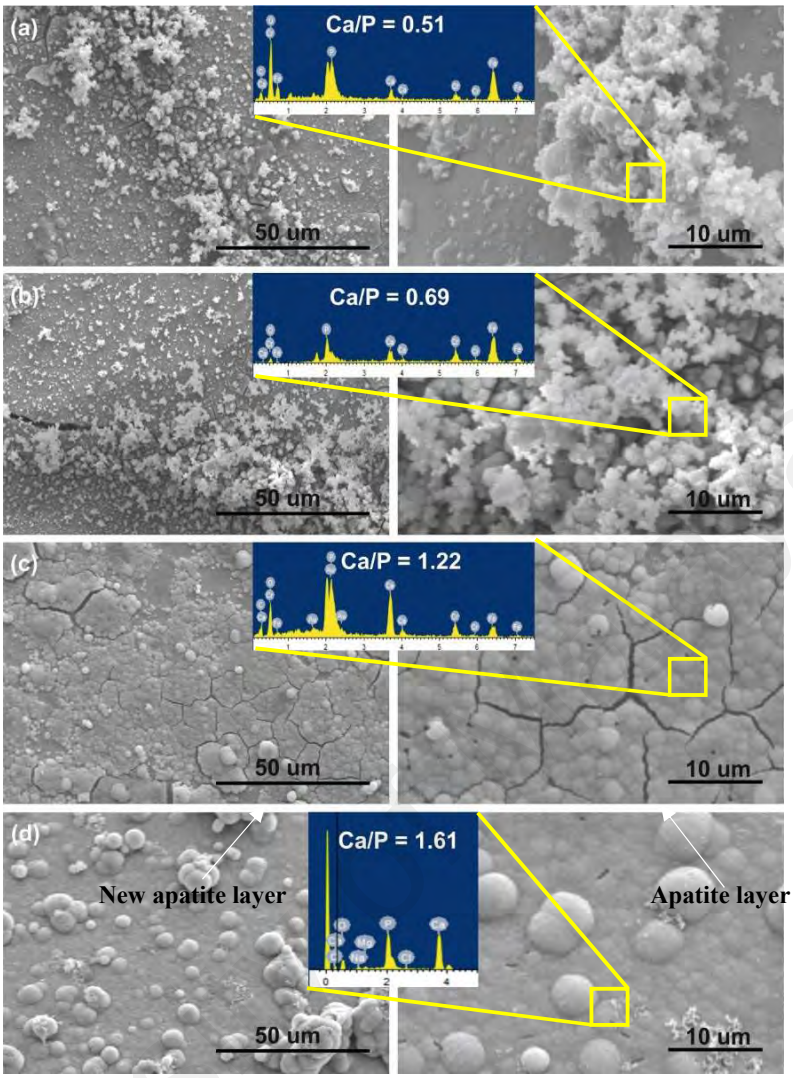

Figure 4.36: SEM imaging and EDS spectra of apatite layer on FeCrMoCB CL after (a) 1 day, (b) 3 days, (c) 7 days, and (d) 21 days soaking in SBF

The average data and the calculated cell-viability % are presented in Table 4.15. According to ISO 10993-1, both the FeCrMoCB MG and Cronidur30 does not appear to have cytotoxic effect. However, the cell-viability of FeCrMoCB MG was decreasing to the 7th day. From the literature, Mo is affecting the growth of cells. This can explain the reduction of cell-viability in the 7th day. However, the existence of Cr in the matrix would affect the cytotoxicity of the CL (Ibrahim, Sarhan, Yusuf, & Hamdi, 2017). So, further biocompatibility examinations are needed to ensure the cytocompatibility of FeCrMoCB MG.

Table 4.15: average of the absorbance values and the corresponding cell-viability %

	Day 1			Day 3			Day 7		
Sample	**Mean**	**SD**	**Viability%**	**Mean**	**SD**	**Viability%**	**Mean**	**SD**	**Viability%**
A	0.1117	0.425	113.31	0.4160	0.117	103.00	1.5816	0.676	69.99
SS	0.0828	0.007	50.64	0.3222	0.038	75.88	1.6868	0.130	74.75
Control	0.1056	0.003		0.4056	0.013		2.2356	0.063	
Blank	0.0594	0.001		0.0598	0.002		0.0622	0.001	

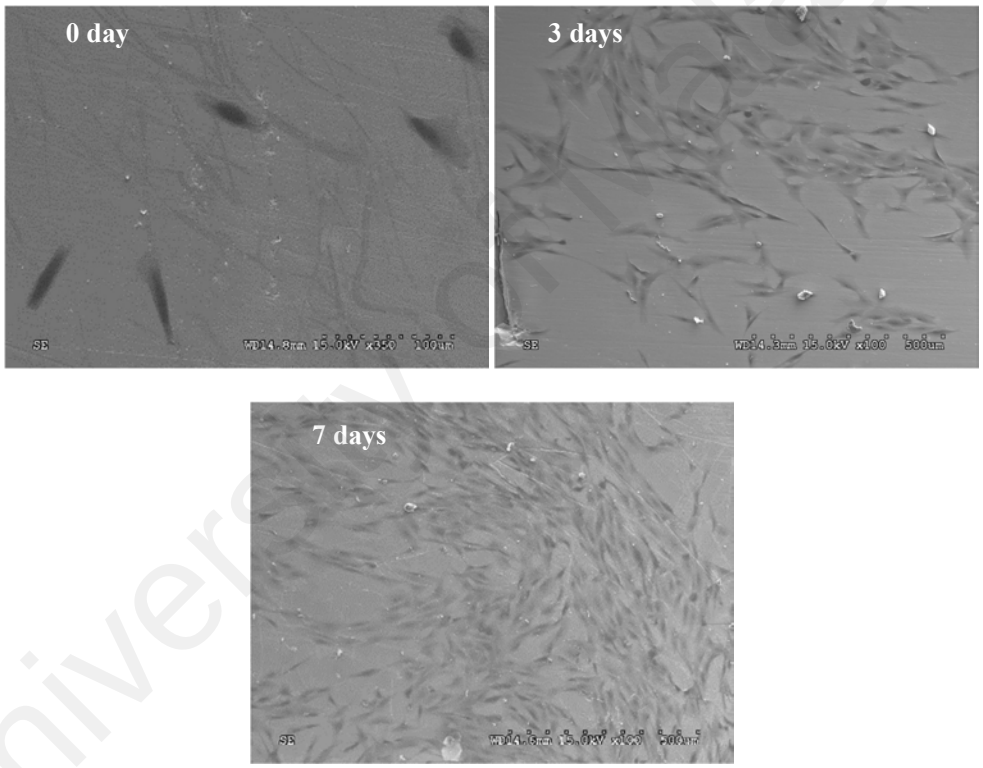

Figure 4.37: Cell morphology on FeCrMoCB MG sample

These results are supported by the cell morphology obtained using the SEM as shown in Figure 4.37 and 4.38. The cells were more flattened on FeCrMoCB MG sample compared to the cells on Cronidur30 sample because FeCrMoCB MG exhibited higher wettability – lower contact angle – facilitating the adhesion of the cells on the surface.

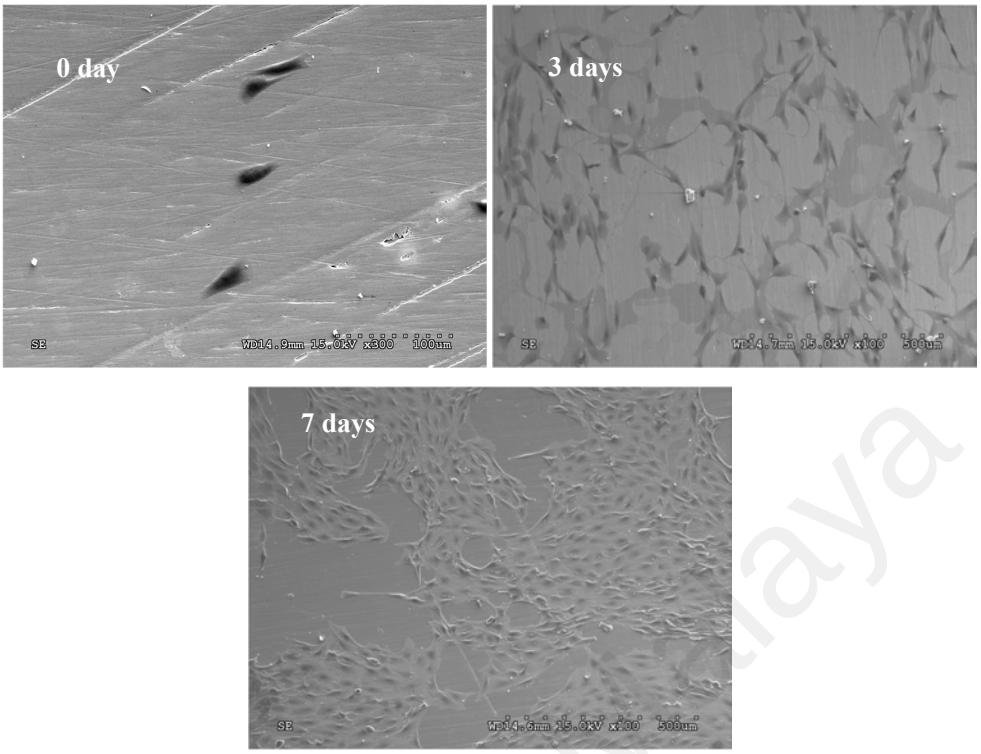

Figure 4.38: Cell morphology on Cronidur30

Table 4.16: absorbance values at 570 nm and cell-viability of the corroded samples

Sample	A	CR30	Control	Blank
Absorbance	1.673	1.681	2.194	0.062
	N/A	1.606	2.058	0.06
Cell-viability %	78.05	76.63		

As stated in the previous chapter, in-vitro cell-culture test was performed on the corroded samples to ensure the biocompatibility of the corrosion compounds formed on the surface of coating layer and substrate. The absorbance values at 570 nm of the MTT assay after 7 days of cell culture as well as the cell-viability % are listed in Table 4.16. These results show that FeCrMoCB MG has acceptable biocompatibility and have a promising potential for biomedical implant applications.

4.6. Conclusion

In this chapter, the results of the experimental work have been demonstrated and discussed. As discussed, the process has been optimized to obtain defect-free samples with the optimized properties. The FeCrMoCB MG has proved enhanced tribological properties and corrosion resistance. Also, FeCrMoCB MG showed to have acceptable biocompatibility as Cronidur30. Moreover, the FeCrMoCB MG has shown in-vitro bioactivity in SBF. The in-vitro cell-culture test showed an acceptable cytocompatibility properties of the FeCrMoCB MG. These results revealed a promising potential of FeCrMoCB MG in the biomedical bone-implant applications. However, further investigations of the in-vivo biocompatibility and bioactivity properties are needed to ensure the validity of the proposed MG system.

CHAPTER 5: CONCLUSION

5.1. Introduction

This research proposed a durable and cost-effective biomedical bone-implant via laser cladding of Fe-based MG coating layer on nickel-free high nitrogen stainless-steel. During this research, a comprehensive literature review has been introduced covering the characteristics of the common metallic biomaterials and the newly developed MGs alloys. Also, the literature included the different coating techniques developed to enhance the biocompatibility and bioactivity properties. It was found that the current metallic biomaterials failed to prove long-term durability (more than 25 years life-span) in a way to minimize the revision surgeries needed.

Thus, Fe-based MG (FeCrMoCB) with superior properties was proposed as a coating on a nickel-free stainless steel to minimize the harmful effect of nickel-ions. The laser cladding technique was selected for its true metallurgical bonding between the coating layer and substrate which in consequence improve the adhesion strength and minimize the separation and delamination of the coating layer. Moreover, laser cladding is cost effective and provide the cooling rate required to produce the amorphous phase of the MG alloy. Another important feature is the controllable process allowing to variate the amorphous content within the coating layer to improve the different properties.

5.2. Conclusion

The FeCrMoCB MG coating layer was optimized through three stages; preliminary experiment, optimization of the substrate surface roughness, and optimization of the laser power, scanning speed, laser beam size and the overlap percentage. The coating layer was optimized based on the morphological properties, mechanical properties, wear and corrosion resistance.

The proposed FeCrMoCB MG laser cladded layer on nickel-free SS substrate was successfully developed without any defects. Moreover, the investigations showed that preparing the substrate with sand polishing paper 240-gritt gave the best cladding layer from the geometry point of view.

It has been shown that the proposed FeCrMoCB MG coating layer has enhanced tribology and corrosion properties in simulated body fluid and has comparable properties to the conventionally used Ti and Co-alloy. The results showed a stable corrosion resistance during the 30 days immersion test which is referred to the stable and regenerated passive layer.

In addition, the FeCrMoCB MG showed a promising in-vitro bioactivity in SBF. The examinations showed nucleation of apatite layer from the first day, and the apatite started growing progressively with immersion time. The Ca/P ratio reached the stoichiometric ratio (1.61) after 21 days of immersion. Finally, the FeCrMoCB MG proved acceptable cytocompatibility bringing promising in-vitro biocompatibility behavior for bone-implants.

Overall, the proposed laser cladded FeCrMoCB MG proved enhanced biocompatibility properties bringing a promising potential in the application of biomedical bone-implants, especially the join-replacement devices.

5.2. Future work and recommendation

Based on the findings of this study, it is recommended to apply more and deeper investigations on the biocompatibility of the laser cladded FeCrMoCB MG to ensure the cytotoxicity of the Cr included in the MG alloy. Moreover, the bioactivity behavior of FeCrMoCB MG needs further study to understand the reasons and the mechanism of growing the apatite-like layer.

Also, in-vivo biocompatibility and bioactivity are required to prove the validity of the Fe-based MG in bone-implants applications.

REFERENCES

Alavi, S. H., & Harimkar, S. P. (2015). Melt expulsion during ultrasonic vibration-assisted laser surface processing of austenitic stainless steel. *Ultrasonics*, *59*, 21–30.

An, Y., Hou, G., Chen, J., Zhao, X., Liu, G., & Zhou, H. (2014). Microstructure and tribological properties of iron-based metallic glass coatings prepared by atmospheric plasma spraying. *Vacuum*, *107*, 132–140.

Arias-González, F., del Val, J., Comesaña, R., Penide, J., Lusquiños, F., Quintero, F., Riveiro, A., Boutinguiza, M., & Pou, J. (2016). Fiber laser cladding of nickel-based alloy on cast iron. *Applied Surface Science*, *374*, 197–205.

Asri, R. I. M., Harun, W. S. W., Samykano, M., Lah, N. A. C., Ghani, S. A. C., Tarlochan, F., & Raza, M. R. (2017). Corrosion and surface modification on biocompatible metals: A review. *Materials Science and Engineering: C*, *77*, 1261–1274.

Audebert, F., Colaço, R., Vilar, R., & Sirkin, H. (2003). Production of glassy metallic layers by laser surface treatment. *Scripta Materialia*, *48*(3), 281–286.

Bai, L., Cui, C., Wang, Q., Bu, S., & Qi, Y. (2008). Ti–Zr–Fe–Si system amorphous alloys with excellent biocompatibility. *Journal of Non-Crystalline Solids*, *354*(33), 3935–3938.

Balasubramanian, P., Büttner, T., Miguez Pacheco, V., & Boccaccini, A. R. (2018). Boron-containing bioactive glasses in bone and soft tissue engineering. *Journal of the European Ceramic Society*, *38*(3), 855–869.

Balla, V. K., & Bandyopadhyay, A. (2010). Laser processing of Fe-based bulk amorphous alloy. *Surface and Coatings Technology*, *205*(7), 2661–2667.

Baradaran, S., Basirun, W. J., Zalnezhad, E., Hamdi, M., Sarhan, A. A. D., & Alias, Y. (2013). Fabrication and deformation behaviour of multilayer Al2O3/Ti/TiO2 nanotube arrays. *Journal of the Mechanical Behavior of Biomedical Materials*, *20*, 272–282.

Barekat, M., Shoja Razavi, R., & Ghasemi, A. (2016). Nd:YAG laser cladding of Co–Cr–Mo alloy on γ-TiAl substrate. *Optics & Laser Technology*, *80*, 145–152.

Bell, J. C., & Richards, M. N. (1987). Some effects of hardness and microstructure on the lubricated wear of steels. *Tribology Series*, *12*, 343–353.

Burguera, J. L., & Burguera, M. (2007). Molybdenum in human whole blood of adult residents of the Merida State (Venezuela). *Journal of Trace Elements in Medicine and Biology*, *21*(3), 178–183.

Buzzi, S., Jin, K., Uggowitzer, P. J., Tosatti, S., Gerber, I., & Löffler, J. F. (2006). Cytotoxicity of Zr-based bulk metallic glasses. *Intermetallics*, *14*(7), 729–734.

Campbell, A. A. (2003). Bioceramics for implant coatings. *Materials Today*, *6*(11), 26–30.

Chen, Q., & Thouas, G. A. (2015). Metallic implant biomaterials. *Materials Science and Engineering R: Reports*, *87*, 1–57.

Chien, C. S., Liu, C. W., & Kuo, T. Y. (2016). Effects of laser power level on microstructural properties and phase composition of laser-clad fluorapatite/zirconia composite coatings on Ti6Al4V substrates. *Materials*, *9*(5).

Chien, C. S., Liu, C. W., Kuo, T. Y., Wu, C. C., & Hong, T. F. (2016). Bioactivity of fluorapatite/alumina composite coatings deposited on Ti6Al4V substrates by laser cladding. *Applied Physics A*, *122*(4), 303.

Choudhury, P., & Agrawal, D. C. (2011). Sol–gel derived hydroxyapatite coatings on titanium substrates. *Surface and Coatings Technology*, *206*(2), 360–365.

Comesaña, R., Quintero, F., Lusquiños, F., Pascual, M. J., Boutinguiza, M., Durán, A., & Pou, J. (2010). Laser cladding of bioactive glass coatings. *Acta Biomaterialia*, *6*(3), 953–61.

Crossgrove, J., & Zheng, W. (2004). Manganese toxicity upon overexposure. *NMR in Biomedicine*, *17*(8), 544–53.

Dewidar, M. M., Khalil, K. A., & Lim, J. K. (2007). Processing and mechanical properties of porous 316L stainless steel for biomedical applications. *Transactions of Nonferrous Metals Society of China*, *17*(3), 468–473.

Espallargas, N., Aune, R. E., Torres, C., Papageorgiou, N., & Muñoz, A. I. (2013). Bulk metallic glasses (BMG) for biomedical applications—A tribocorrosion investigation of Zr55Cu30Ni5Al10 in simulated body fluid. *Wear*, *301*(1), 271–279.

Evans, E. J., & Thomas, I. T. (1986). The in vitro toxicity of cobalt-chrome-molybdenum alloy and its constituent metals. *Biomaterials*, *7*(1), 25–9.

Ezazi, M. A., Yusof, F., Sarhan, A. A. D., Hamdi, M., Shukor, A., & Fadzil, M. (2015). Employment of fiber laser technology to weld austenitic stainless steel 304 l with aluminum alloy 5083 using pre-placed activating flux. *Jmade*, *87*, 105–123.

FAN, X., CHEN, J., ZOU, J., WAN, Q., ZHOU, Z., & RUAN, J. (2009). Bone-like apatite formation on HA/316L stainless steel composite surface in simulated body fluid. *Transactions of Nonferrous Metals Society of China*, *19*(2), 347–352.

Fathi, M.H., Salehi, M., Saatchi, A., Mortazavi, V., & Moosavi, S.B. (2003). In vitro corrosion behavior of bioceramic, metallic, and bioceramic–metallic coated stainless steel dental implants. *Dental Materials*, *19*(3), 188–198.

Filiaggi, M.J., Pilliar, R.M., & Coombs, N.A. (1993). Post-plasma-spraying heat treatment of the HA coating/Ti-6Al-4V implant system. *Journal of Biomedical Materials Research*, *27*(2), 191–198.

Frazier, W. E. (2014). Metal Additive Manufacturing: A Review. *Journal of Materials Engineering and Performance*, *23*(6), 1917–1928.

Fujita, K., Zhang, W., Shen, B., Amiya, K., Ma, C. L., & Nishiyama, N. (2012). Fatigue properties in high strength bulk metallic glasses. *Intermetallics*, *30*, 12–18.

Galván, J. C., Larrea, M. T., Braceras, I., Multigner, M., & González-Carrasco, J. L. (2016). In vitro corrosion behaviour of surgical 316LVM stainless steel modified by Si+ ion implantation – An electrochemical impedance spectroscopy study. *Journal of Alloys and Compounds*, *676*, 414–427.

Gao, Y.L., Shen, J., Sun, J.F., Wang, G., Xing, D.W., Xian, H.Z., & Zhou, B.D. (2003). Crystallization behavior of ZrAlNiCu bulk metallic glass with wide supercooled liquid region. *Materials Letters*, *57*(13), 1894–1898.

Gludovatz, B., Demetriou, M. D., Floyd, M., Hohenwarter, A., Johnson, W. L., & Ritchie, R. O. (2013). Enhanced fatigue endurance of metallic glasses through a staircase-like fracture mechanism. *Proceedings of the National Academy of Sciences of the United States of America*, *110*(46), 18419–24.

Goharian, A., & Abdullah, M. R. (2017). Bioinert metals (stainless steel, titanium, cobalt chromium). In *Trauma Plating Systems* (pp. 115–142).

Goodman, S. B., Yao, Z., Keeney, M., & Yang, F. (2013). The future of biologic coatings for orthopaedic implants. *Biomaterials*, *34*(13), 3174–83.

Gross, K. A., Chai, C. S., Kannangara, G. S. K., Ben-Nissan, B., & Hanley, L. (1998). Thin hydroxyapatite coatings via sol–gel synthesis. *Journal of Materials Science: Materials in Medicine*, *9*(12), 839–843.

Gu, X. J., Poon, S. J., & Shiflet, G. J. (2007). Mechanical properties of iron-based bulk metallic glasses. *Journal of Materials Research*, *22*(02), 344–351.

Guo, S., & Su, C. (2017). Micro/nano ductile-phases reinforced Fe-based bulk metallic glass matrix composite with large plasticity. *Materials Science and Engineering A*, *707*, 44–50.

Hakki, S. S., Dundar, N., Kayis, S. A., Hakki, E. E., Hamurcu, M., Kerimoglu, U., Baspinar, N., Basoglu, A., & Nielsen, F. H. (2013). Boron enhances strength and alters mineral composition of bone in rabbits fed a high energy diet. *Journal of Trace Elements in Medicine and Biology*, *27*(2), 148–153.

He, G., Guo, B., Wang, H., Liang, C., Ye, L., Lin, Y., & Cai, X. (2014). Surface characterization and osteoblast response to a functionally graded hydroxyapatite/ fluoro-hydroxyapatite/titanium oxide coating on titanium surface by sol-gel method. *Cell Proliferation*, *47*(3), 258–266.

Hermawan, H., Ramdan, D., & Djuansjah, J. R. P. (2011). Metals for biomedical applications. In R. Fazel (Ed.), *Biomedical Engineering: from Theory to Applications* (pp. 411–430).

Herzog, D., Seyda, V., Wycisk, E., & Emmelmann, C. (2016). Additive manufacturing of metals. *Acta Materialia*, *117*(September), 371–392.

Hofmann, D. C. (2013). Bulk Metallic Glasses and Their Composites: A Brief History of Diverging Fields. *Journal of Materials*, 1–8.

Horton, J. A., & Parsell, D. E. (2002). Biomedical Potential of a Zirconium-Based Bulk Metallic Glass. *MRS Proceedings*, *754*, CC 1.5.

Hua, N., Zheng, Z., Fang, H., Ye, X., Lin, C., Li, G., Wang, W., Chen, W., Zhang, T. (2015). Dry and lubricated tribological behavior of a Ni- and Cu-free Zr-based bulk metallic glass. *Journal of Non-Crystalline Solids*, *426*, 63–71.

Huang, C. H., Lai, J. J., Wei, T. Y., Chen, Y. H., Wang, X., Kuan, S. Y., & Huang, J. C. (2015). Improvement of bio-corrosion resistance for Ti42Zr40Si15Ta3 metallic glasses in simulated body fluid by annealing within supercooled liquid region. *Materials Science and Engineering: C*, *52*, 144–150.

Huang, L., Pu, C., Fisher, R. K., Mountain, D. J. H., Gao, Y., Liaw, P. K., Zhang, W., & He, W. (2015). A Zr-based bulk metallic glass for future stent applications: Materials properties, finite element modeling, and in vitro human vascular cell response. *Acta Biomaterialia*, *25*, 356–368.

Huang, L., Qiao, D., Green, B. A., Liaw, P. K., Wang, J., Pang, S., & Zhang, T. (2009). Bio-corrosion study on zirconium-based bulk-metallic glasses. *Intermetallics*, *17*(4), 195–199.

Nantel, G., & Tontisirin, K. (2001). *Human Vitamin and Mineral Requirements Report of a joint FAO/WHO expert consultation Bangkok, Thailand*.

Hussain, M. A., Maqbool, A., Khalid, F. A., Bakhsh, N., Hussain, A., Rahman, J. U., Park, J. K., Park, T. G., Hyun, L. J., & Kim, M. H. (2014). Mechanical properties of CNT reinforced hybrid functionally graded materials for bioimplants. *Transactions of Nonferrous Metals Society of China*, *24*, s90–s98.

Ibrahim, M. Z., Sarhan, A. A. D., Kuo, T. Y., Yusuf, F., Hamdi, M., & Chien, C. S. (2018). Investigate the effects of the substrate surface roughness on the geometry, phase transformation, and hardness of laser-cladded Fe-based metallic glass coating. *The International Journal of Advanced Manufacturing Technology*.

Ibrahim, M. Z., Sarhan, A. A. D., Yusuf, F., & Hamdi, M. (2017). Biomedical materials and techniques to improve the tribological, mechanical and biomedical properties of orthopedic implants – A review article. *Journal of Alloys and Compounds*, *714*, 636–667.

Jeong, Y.-H., Moon, B.-H., Choe, H.-C., & Brantley, W. A. (2013). Surface characteristics of hydroxyapatite-coated layer prepared on nanotubular Ti–35Ta–xHf alloys by EB-PVD. *Thin Solid Films*, *549*, 147–153.

Kartik, B., Veerababu, R., Sundararamanc, M., & Satyanarayana, D. V. V. (2015). Effect of high temperature ageing on microstructure and mechanical properties of a nickel-free high nitrogen austenitic stainless steel. *Materials Science and Engineering: A*, *642*, 288–296.

Kasuga, T. (2010). Coatings for metallic biomaterials. *Metals for Biomedical Devices* (pp. 260–282).

Kokubo, T. (1998). Apatite formation on surfaces of ceramics, metals and polymers in body environment. *Acta Materialia*, *46*(7), 2519–2527.

Kokubo, T., & Takadama, H. (2006). How useful is SBF in predicting in vivo bone bioactivity? *Biomaterials*, *27*(15), 2907–2915.

Kubala-Kukuś, A., Banaś, D., Braziewicz, J., Majewska, U., Pajek, M., Wudarczyk-Moćko, J., Antczak, G., Borkowska, B., Góźdź, S., & Smok-Kalwat, J. (2014). Analysis of copper concentration in human serum by application of total reflection X-ray fluorescence method. *Biological Trace Element Research*, *158*(1), 22–8.

Kulpetchdara, K., Limpichaipanit, A., Rujijanagul, G., Randorn, C., & Chokethawai, K. (2016). Influence of the nano hydroxyapatite powder on thermally sprayed HA coatings onto stainless steel. *Surface and Coatings Technology*, *Volume 306*, 181–186.

Kwon, O. J., Kim, Y. C., Kim, K. B., Lee, Y. K., & Fleury, E. (2006). Formation of amorphous phase in the binary Cu−Zr alloy system. *Metals and Materials International*, *12*(3), 207–212.

Lee, K., Nam, D.-H., Lee, S., & Kim, N. J. (2006). Hardness and wear resistance of Zr-based bulk metallic glass/Ti surface composites fabricated by high-energy electron beam irradiation. *Surface and Coatings Technology*, *201*(3), 1620–1628.

Li, D., Chen, X., Hui, X., Wang, J., Jin, P., & Li, H. (2017). Effect of amorphicity of HVOF sprayed Fe-based coatings on their corrosion performances and contacting osteoblast behavior. *Surface and Coatings Technology*, *310*, 207–213.

Li, H. F., & Zheng, Y. F. (2016). Recent advances in bulk metallic glasses for biomedical applications. *Acta Biomaterialia*, *36*, 1–20.

Li, S., Wei, Q., Li, Q., Jiang, B., Chen, Y., & Sun, Y. (2015). Development of Fe-based bulk metallic glasses as potential biomaterials. *Materials Science and Engineering: C*, *52*, 235–241.

Li, X. P., Roberts, M., Liu, Y. J., Kang, C. W., Huang, H., & Sercombe, T. B. (2015). Effect of substrate temperature on the interface bond between support and substrate during selective laser melting of Al-Ni-Y-Co-La metallic glass. *Materials and Design, 65,* 1-6.

Li, X. P., Roberts, M. P., O'Keeffe, S., & Sercombe, T. B. (2016). Selective laser melting of Zr-based bulk metallic glasses: Processing, microstructure and mechanical properties. *Materials & Design*, *112*, 217–226.

Li, Z., Zhang, C., & Liu, L. (2015). Wear behavior and corrosion properties of Fe-based thin film metallic glasses. *Journal of Alloys and Compounds*, *650*, 127–135.

Liang, D., Wei, X., Chang, C., Li, J., Wang, X., & Shen, J. (2018). Effect of W addition

on the glass forming ability and mechanical properties of Fe-based metallic glass. *Journal of Alloys and Compounds*, *731*, 1146–1150.

Liang, X., Chen, J., Mora, M. T., Fernandez Urdaneta, J., & Zeng, Q. (2017). Effect of precipitation on the hardness of ternary metallic glass. *Advances in Materials Physics and Chemistry*, *7*, 255–262.

Liao, Z., Hua, N., Chen, W., Huang, Y., & Zhang, T. (2017). Correlations between the wear resistance and properties of bulk metallic glasses. *Intermetallics, 93,* 290-298.

Liu, D.-M., Yang, Q., & Troczynski, T. (2002). Sol–gel hydroxyapatite coatings on stainless steel substrates. *Biomaterials*, *23*, 691–698.

Liu, H., Hao, J., Han, Z., Yu, G., He, X., & Yang, H. (2016). Microstructural evolution and bonding characteristic in multi-layer laser cladding of NiCoCr alloy on compacted graphite cast iron. *Journal of Materials Processing Technology*, *232*, 153–164.

Liu, H., Qin, X., Huang, S., Hu, Z., & Ni, M. (2018). Geometry modeling of single track cladding deposited by high power diode laser with rectangular beam spot. *Optics and Lasers in Engineering*, *100*, 38–46.

Liu, Z., Chan, K. C., Liu, L., & Guo, S. F. (2012). Bioactive calcium titanate coatings on a Zr-based bulk metallic glass by laser cladding. *Materials Letters*, *82*, 67–70.

Löffler, J. F. (2003). Bulk metallic glasses. *Intermetallics*, *11*(6), 529–540.

Lu, Y., Huang, G., Wang, Y., Li, H., Qin, Z., & Lu, X. (2018). Crack-free Fe-based amorphous coating synthesized by laser cladding. *Materials Letters*, *210*, 46–50.

Chen, Q. J., Hu, L. L., Zhou, X. L., Hua, X. Z., & Yang, Y. J. (2011). Effect of Corrosive Medium on the Corrosion Resistance of FeCrMoCB Amorphous Alloy Coating. *Advanced Materials Research*, *291–294*, 65–71.

Mahbooba, Z., Thorsson, L., Unosson, M., Skoglund, P., West, H., Horn, T., … Harrysson, O. (2018). Additive manufacturing of an iron-based bulk metallic glass larger than the critical casting thickness. *Applied Materials Today*, *11*, 264–269.

Luo, K. Y., Jing, X., Sheng, J., Sun, G. F., Yan, Z., & Lu, J. Z. (2016). Characterization and analyses on micro-hardness, residual stress and microstructure in laser cladding coating of 316L stainless steel subjected to massive LSP treatment. *Journal of Alloys and Compounds*, *673*, 158–169.

Ma, M. Z., Liu, R. P., Xiao, Y., Lou, D. C., Liu, L., Wang, Q., & Wang, W. K. (2004). Wear resistance of Zr-based bulk metallic glass applied in bearing rollers. *Materials Science and Engineering: A*, *386*(1), 326–330.

Ma, T., Wan, P., Cui, Y., Zhang, G., Li, J., Liu, J., … Lu, L. (2012). Cytocompatibility of high nitrogen nickel-free stainless steel for orthopedic implants. *Journal of Materials Science & Technology*, *28*(7), 647–653.

Mansur, M. R., Wang, J., & Berndt, C. C. (2013). Microstructure, composition and

hardness of laser-assisted hydroxyapatite and Ti-6Al-4V composite coatings. *Surface and Coatings Technology*, *232*, 482–488.

Medical Implants Market Global Forecast To 2023 | MRFR. (2018).

Menghua, L., Tieying, Y., Yazhou, W., Feifei, D., Xingzheng, Z., Hans, G., & Guixue, W. (2014). Study of biocompatibility of medical grade high nitrogen nickel-free austenitic stainless steel in vitro. *Materials Science and Engineering: C*, *43*, 641–648.

Metallic Implant Materials. (2007). *Biomaterials* (pp. 99–137). New York, NY: Springer New York.

Mittal, M., Nath, S. K., & Prakash, S. (2011). Characterization of plasma sprayed hydroxyapatite coatings on AISI 316L SS and titanium substrate and their corrosion behavior in simulated body fluid. *Journal of Minerals & Materials Characterization & Engineering*, *10*(11), 1041–1049.

Mohseni, E., Zalnezhad, E., & Bushroa, A. R. (2014). Comparative investigation on the adhesion of hydroxyapatite coating on Ti-6Al-4V implant: A review paper. *International Journal of Adhesion and Adhesives*, *48*.

Mohseni, E., Zalnezhad, E., Bushroa, A. R., Abdel Magid Hamouda, Goh, B. T., & Yoon, G. H. (2015). Ti/TiN/HA coating on Ti–6Al–4V for biomedical applications. *Ceramics International*, *41*(10), 14447–14457.

Moritz, N., Vedel, E., Ylänen, H., Jokinen, M., Hupa, M., & Yli-Urpo, A. (2004). Characterisation of bioactive glass coatings on titanium substrates produced using a CO 2 laser. *Journal of Materials Science: Materials in Medicine*, *15*(7), 787–794.

Muley, S. V., Vidvans, A. N., Chaudhari, G. P., & Udainiya, S. (2016). An assessment of ultra fine grained 316L stainless steel for implant applications. *Acta Biomaterialia*, *30*, 408–419.

Nenadl, O., Ocelík, V., Palavra, A., & Hosson, J. T. M. De. (2014). The Prediction of Coating Geometry from Main Processing Parameters in Laser Cladding. *Physics Procedia*, *56*, 220–227.

Niinomi, M. (2002). Recent metallic materials for biomedical applications. *Metallurgical and Materials Transactions A*, *33*(3), 477–486.

Niinomi, M. (2008). Biologically and mechanically biocompatible titanium alloys. *MATERIALS TRANSACTIONS*, *49*(10), 2170–2178.

Odahara, T., Matsumoto, H., & Chiba, A. (2008). Mechanical properties of biomedical Co-33Cr-5Mo-0.3N alloy at elevated temperatures. *Materials Transactions*, *49*(9), 1963–1969.

Okazaki, Y., & Gotoh, E. (2005). Comparison of metal release from various metallic biomaterials in vitro. *Biomaterials*, *26*(1), 11–21.

Olding, T., Sayer, M., & Barrow, D. (2001). Ceramic sol–gel composite coatings for

electrical insulation. *Thin Solid Films*, *398*, 581–586.

Omar, S. A., Ballarre, J., & Ceré, S. M. (2016). Protection and functionalization of AISI 316L stainless steel for orthopedic implants: hybrid coating and sol gel glasses by spray to promote bioactivity. *Electrochimica Acta*, *203*, 309–315.

Orthopedic Implants Market Size | Industry Report, 2024. (2016). San Francisco.

Pei, X., Wang, J., Wan, Q., Kang, L., Xiao, M., & Bao, H. (2011). Functionally graded carbon nanotubes/hydroxyapatite composite coating by laser cladding. *Surface and Coatings Technology*, *205*(19), 4380–4387.

Pinkerton, A. J. (2016). [INVITED] Lasers in additive manufacturing. *Optics & Laser Technology*, *78*, 25–32.

Plecko, M., Sievert, C., Andermatt, D., Frigg, R., Kronen, P., Klein, K., Stübinger, S., Nuss, K., Bürki, A., Ferguson, S., Stoeckle, U., von Rechenberg, B., Albrektsson, T., Berglundh, T., Lindhe, J., & Richards, R. (2012). Osseointegration and biocompatibility of different metal implants - a comparative experimental investigation in sheep. *BMC Musculoskeletal Disorders*, *13*(1), 32.

Pourhashem, S., & Afshar, A. (2014). Double layer bioglass-silica coatings on 316L stainless steel by sol-gel method. *Ceramics International*, *40*(1 PART A), 993–1000.

Pramanik, S., Agarwal, A. K., & Rai, K. N. (2005). Chronology of total hip joint replacement and materials development. *Trends Biomater . Artif . Organs*, *19*(1), 15–26.

Qiao, D. C., Wang, G. Y., Liaw, P. K., Ponnambalam, V., Poon, S. J., Shiflet, G. J., & Buchanan, R. A. (2007). Fatigue behavior of an Fe48Cr15Mo14Er2C15B6 amorphous steel. *Journal of Materials Research*, *22*(02), 544–550.

Qin, C., Hu, Q., Li, Y., Wang, Z., Zhao, W., Louzguine-Luzgin, D. V., & Inoue, A. (2016). Novel bioactive Fe-based metallic glasses with excellent apatite-forming ability. *Materials Science and Engineering: C*, *69*, 513–521.

Quazi, M. M., Fazal, M. A., Haseeb, A. S. M. A., Yusof, F., Masjuki, H. H., & Arslan, A. (2016). Effect of rare earth elements and their oxides on tribo-mechanical performance of laser claddings: A review. *Journal of Rare Earths*, *34*(6), 549–564.

Rahaman, M. L., Zhang, L. C., & Ruan, H. H. (2013). Understanding the friction and wear mechanisms of bulk metallic glass under contact sliding. *Wear*, *304*(1–2), 43–48.

Rahmati, B., Sarhan, A. A. D., Zalnezhad, E., Kamiab, Z., Dabbagh, A., Choudhury, D., & Abas, W. A. B. W. (2015). Development of tantalum oxide (Ta-O) thin film coating on biomedical Ti-6Al-4V alloy to enhance mechanical properties and biocompatibility. *Ceramics International*, *42*(1), 466–480.

Rahmati, B., Zalnezhad, E., Sarhan, A. A. D., Kamiab, Z., Nasiri Tabrizi, B., & Abas, W.

A. B. W. (2015). Enhancing the adhesion strength of tantalum oxide ceramic thin film coating on biomedical Ti-6Al-4V alloy by thermal surface treatment. *Ceramics International*, *41*(10), 13055–13063.

Ramasamy, P., Szabo, A., Borzel, S., Eckert, J., Stoica, M., & Bárdos, A. (2016). High pressure die casting of Fe- based metallic glass. *Nature Publishing Group*.

Rautray, T. R., Narayanan, R., & Kim, K.-H. (2011). Ion implantation of titanium based biomaterials. *Progress in Materials Science*, *56*(8), 1137–1177.

Sanli, I., Arts, J. J. C., & Geurts, J. (2016). Clinical and Radiologic Outcomes of a Fully Hydroxyapatite-Coated Femoral Revision Stem: Excessive Stress Shielding Incidence and its Consequences. *The Journal of Arthroplasty*, *31*(1), 209–214.

Schroers, J., Kumar, G., Hodges, T. M., Chan, S., & Kyriakides, T. R. (2009). Bulk metallic glasses for biomedical applications. *JOM*, *61*(9), 21–29.

Segu, D. Z., Choi, J. H., Yi, S., & Kim, S. S. (2012). Dry sliding tribological properties of Fe-based bulk metallic glass. *Tribology Letters*, *47*(1), 131–138.

Shamray, V. F., Sirotinkin, V. P., Smirnov, I. V., Kalita, V. I., Fedotov, A. Y., Barinov, S. M., & Komlev, V. S. (2017). Structure of the hydroxyapatite plasma-sprayed coatings deposited on pre-heated titanium substrates. *Ceramics International*.

Sharma, U., Concagh, D., Core, L., Kuang, Y., You, C., Pham, Q., & Palasis, M. (2017). The development of bioresorbable composite polymeric implants with high mechanical strength. *Nature Materials*, *17*(1), 96–103.

Shu, F., Tian, Z., Zhao, H., He, W., Sui, S., & Liu, B. (2016). Synthesis of amorphous coating by laser cladding multi-layer Co-based self-fluxed alloy powder. *Materials Letters*, *176*, 306–309.

Sola, A., Bellucci, D., & Cannillo, V. (2016). Functionally graded materials for orthopedic applications – an update on design and manufacturing. *Biotechnology Advances*, *34*(5), 504–531.

Stoch, A., Jastrze¸bski, W., Długoń, E., Lejda, W., Trybalska, B., Stoch, G. J., & Adamczyk, A. (2005). Sol–gel derived hydroxyapatite coatings on titanium and its alloy Ti6Al4V. *Journal of Molecular Structure*, *744*, 633–640.

Sun, Y., Huang, Y., Fan, H., Liu, F., Shen, J., Sun, J., & Chen, J. J. J. (2014). Comparison of mechanical behaviors of several bulk metallic glasses for biomedical application. *Journal of Non-Crystalline Solids*, *406*, 144–150.

Sun, Y., Huang, Y., Fan, H., Wang, Y., Ning, Z., Liu, F., & Chen, J. J. J. (2015). In vitro and in vivo biocompatibility of an Ag-bearing Zr-based bulk metallic glass for potential medical use. *Journal of Non-Crystalline Solids*, *419*, 82–91.

Talha, M., Behera, C. K., & Sinha, O. P. (2013). A review on nickel-free nitrogen containing austenitic stainless steels for biomedical applications. *Materials Science*

and Engineering: C, *33*(7), 3563–3575.

Tatkare, D. (2016). *Medical Implants Market - Growth, Global Share, Industry Overview, Analysis, Trends Opportunities and Forecast 2014 - 2020*.

Thevenot, P., Hu, W., & Tang, L. (2008). Surface chemistry influences implant biocompatibility. *Current Topics in Medicinal Chemistry*, *8*(4), 270–80.

Tlotleng, M., Akinlabi, E., Shukla, M., & Pityana, S. (2014). Microstructures, hardness and bioactivity of hydroxyapatite coatings deposited by direct laser melting process. *Materials Science and Engineering: C*, *43*, 189–198.

Trexler, M. M., & Thadhani, N. N. (2010). Mechanical properties of bulk metallic glasses. *Progress in Materials Science*, *55*(8), 759–839.

Wai Yip, M., Barnes, S., & Aly Diaa Mohmmed Sarhan, A. (2015). Deposition of a Silicon Carbide Reinforced Metal Matrix Composite (P25) Layer Using CO_2 Laser. *Journal of Manufacturing Science and Engineering*, *137*(3), 031010.

Wang, G. Y., Liaw, P. K., Peter, W. H., Yang, B., Yokoyama, Y., Benson, M. L., Green, B.A., Kirkham, M.J., White, S.A., Saleh, T.A., McDaniels, R.L., Steward, R.V., Buchanan, R.A., Liu, C.T., & Brooks, C. R. (2004). Fatigue behavior of bulk-metallic glasses. *Intermetallics*, *12*(7), 885–892.

Wang, G. Y., Liaw, P. K., Yokoyama, Y., Inoue, A., & Liu, C. T. (2008). Fatigue behavior of Zr-based bulk-metallic glasses. *Materials Science and Engineering: A*, *494*(1), 314–323.

Wang, Y. B., Li, H. F., Zheng, Y. F., & Li, M. (2012). Corrosion performances in simulated body fluids and cytotoxicity evaluation of Fe-based bulk metallic glasses. *Materials Science and Engineering: C*, *32*(3), 599–606.

Wang, Y., Liu, X., Fan, T., Tan, Z., Zhou, Z., & He, D. (2017). In vitro evaluation of hydroxyapatite coatings with (002) crystallographic texture deposited by micro-plasma spraying. *Materials Science and Engineering: C*, *75*, 596–601.

Wang, Y., Shi, L., Duan, D., Li, S., & Xu, J. (2014). Tribological properties of Zr61Ti2Cu25Al12 bulk metallic glass under simulated physiological conditions. *Materials Science and Engineering: C*, *37*, 292–304.

Weber, T., de Wit, L., Saris, F. W., Königer, A., Rauschenbach, B., Wolf, G. K., & Krauss, S. (1995). Hardness and corrosion resistance of single-phase nitride and carbide on iron. *Materials Science and Engineering: A*, *199*(2), 205–210.

Wei, Q., Li, S., Han, C., Li, W., Cheng, L., Hao, L., & Shi, Y. (2015). Selective laser melting of stainless-steel/nano-hydroxyapatite composites for medical applications: Microstructure, element distribution, crack and mechanical properties. *Journal of Materials Processing Technology*, *222*, 444–453.

Williams, D. (2003). Revisiting the definition of biocompatibility. *Medical Device*

Technology, *14*(8), 10–3.

Wu, X. L., & Hong, Y. S. (2001). Novel Fe70Zr10Ni6Al4Si6B4 thick metallic glass coating produced by laser cladding. *Materials Science and Technology*, *17*(8), 1025–1028.

Wu, Z.-J., He, L.-P., & Chen, Z.-Z. (2006). Fabrication and characterization of hydroxyapatite/Al 2 O 3 biocomposite coating on titanium. *Transactions of Nonferrous Metals Society of China*, *16*, 259–266.

Xu, M., Li, J., Jiang, J., & Li, B. (2015). Influence of Powders and Process Parameters on Bonding Shear Strength and Micro Hardness in Laser Cladding Remanufacturing. *Procedia CIRP*, *29*, 804–809.

Yamamoto, A., Honma, R., & Sumita, M. (1998). Cytotoxicity evaluation of 43 metal salts using murine fibroblasts and osteoblastic cells. *Journal of Biomedical Materials Research*, *39*(2), 331–340.

Yazdipour, A., & Heidarzadeh, A. (2016). Effect of friction stir welding on microstructure and mechanical properties of dissimilar Al 5083-H321 and 316L stainless steel alloy joints. *Journal of Alloys and Compounds*, *680*, 595–603.

Ye, X., Bae, H., Shin, Y. C., & Stanciu, L. A. (2015). In Situ Synthesis and Characterization of Zr-Based Amorphous Composite by Laser Direct Deposition. *Metallurgical and Materials Transactions A*, *46*(9), 4316–4325.

Yue, T. M., Su, Y. P., & Yang, H. O. (2007). Laser cladding of Zr65Al7.5Ni10Cu17.5 amorphous alloy on magnesium. *Materials Letters*, *61*(1), 209–212.

Zalnezhad, E., Baradaran, S., Bushroa, A. R., & Sarhan, A. A. D. (2014). Mechanical property enhancement of Ti-6Al-4V by Multilayer thin solid film Ti/TiO2 nanotubular array coating for biomedical application. *Metallurgical and Materials Transactions A: Physical Metallurgy and Materials Science*, *45*(2), 785–797.

Zeng, C., Tian, W., Liao, W. H., & Hua, L. (2016). Microstructure and porosity evaluation in laser-cladding deposited Ni-based coatings. *Surface and Coatings Technology*, *294*, 122–130.

Zhang, P., & Liu, Z. (2016). Physical-mechanical and electrochemical corrosion behaviors of additively manufactured Cr-Ni-based stainless steel formed by laser cladding. *Materials & Design*, *100*, 254–262.

Zhang, Y., Lin, X., Wang, L., Wei, L., Liu, F., & Huang, W. (2015). Microstructural analysis of Zr55Cu30Al10Ni5 bulk metallic glasses by laser surface remelting and laser solid forming. *Intermetallics*, *66*, 22–30.

Zhao, X., Wang, G., Zheng, H., Lu, Z., Cheng, X., & Zreiqat, H.(2014). Refining nanotopographical features on bone implant surfaces by altering surface chemical compositions. *RSC Adv.*, *4*(97), 54226–54234.

Zhou, H., Zhang, C., Wang, W., Yasir, M., & Liu, L. (2015). Microstructure and Mechanical Properties of Fe-based Amorphous Composite Coatings Reinforced by Stainless Steel Powders. *Journal of Materials Science & Technology*, *31*(1), 43–47.

Zhu, Y. Y., Li, Z. G., Li, R. F., Li, M., Daze, X. L., Feng, K., & Wu, Y. X. (2013). Microstructure and property of Fe–Co–B–Si–C–Nb amorphous composite coating fabricated by laser cladding process. *Applied Surface Science*, *280*, 50–54.

LIST OF PUBLICATIONS

Published papers in peer-reviewed journals

- **Ibrahim, Mahmoud Z**. Sarhan, Ahmed A.D. Yusuf, Farazila, Hamdi M., Biomedical materials and techniques to improve the tribological, mechanical and biomedical properties of orthopedic implants – A review article (2017), *Journal of Alloys and Compounds*, *714*, 636-667. ***(ISI-Q1)***

- **Ibrahim, Mahmou Z.**, Sarhan, A. A. D., Kuo, T. Y., Yusuf, F., Hamdi, M., & Chien, C. S., Investigate the effects of the substrate surface roughness on the geometry, phase transformation, and hardness of laser-cladded Fe-based metallic glass coating (2018). *The International Journal of Advanced Manufacturing Technology, 98,* 1977-1987. ***(ISI-Q1).***

- **Ibrahim, Mahmoud Z.**, Sarhan, A.D., Kuo T.Y., Hamdi M., Yusof F., Chien, C.S., Chang, C.P., Lee, T.M., Advancement of the artificial amorphous-crystalline structure of laser cladded FeCrMoCB on nickel-free stainless-steel for bone-implants (2019), *Materials Chemistry and Physics*, *227*, 358-367. ***(ISI-Q2).***

- **Ibrahim, Mahmoud Z.**, Sarhan, A.D., Kuo, T.Y., Yusof, F., Hamdi, M., Characterization and hardness enhancement of amorphous Fe-based metallic glass laser cladded on nickel-free stainless steel for biomedical implant application (2019). *Materials Chemistry and Physics, 235,* 121745. ***(ISI-Q2).***

Book chapter

- Ibrahim, Mahmoud Z., Sarhan, A. D., Shaikh, M. O., Kuo, T. Y., Yusuf, F., Hamdi, M, Investigate the effects of the laser cladding parameters on the microstructure, phases formation, mechanical and corrosion properties of metallic glasses coatings for biomedical implant application (2019), *Additive Manufacturing of Emerging Materials, Springer Nature*, 299-323.

Papers accepted in conferences

- Ahmed A.D. Sarhan, **Mahmoud Z. Ibrahim**, T.Y. Kuo, Farazila Yusuf, M. Hamdi, C.S. Chien, T.F. Hong, Influence of Laser Power and Scanning Speed on the Hardness and Microstructure of Fe-Based Metallic Glass Coating on Nickel-Free Stainless-Steel Substrate, **2017 International Symposium on Novel and Sustainable Technology, Tainan, Taiwan.**